

**Experimental Analysis and Computational Modeling of  
Annealing in AA6xxx Alloys**

by

Panthea Sepehrband

A thesis

presented to the university of Waterloo

in fulfillment of the

thesis requirement for the degree of

Doctor of Philosophy

in

Mechanical Engineering

Waterloo, Ontario, Canada, 2010

©Panthea Sepehrband 2010

## **AUTHOR'S DECLARATION**

I hereby declare that I am the sole author of this thesis. This is a true copy of the thesis, including any required final revisions, as accepted by my examiners.

I understand that my thesis may be made electronically available to the public.

## ABSTRACT

Microstructural evolution in a naturally-aged and cold-rolled AA6451 aluminum alloy during a non-isothermal annealing process, which leads to significant grain refinement, is investigated through: (a) conducting a comprehensive experimental analysis and (b) developing a computational modeling technique. The underlying mechanisms of annealing have been investigated through analysing interactive phenomena between precipitation and concurrent recovery and recrystallization. It is shown that the interactions between solute elements, clusters, and fine precipitates with dislocations restrict dynamic and static recovery during deformation and subsequent annealing. Inhibition of recovery favours recrystallization that initiates at 300°C and progresses through a nucleation and growth mechanism. Despite localized inhomogeneities, nucleation mainly occurs in non-recovered high energy sites which are uniformly distributed within the entire structure. Growth of the recrystallized nuclei is restricted by pinning precipitates that undergo a concurrent coarsening process. The fine, uniform distribution of recrystallized nuclei and their limited growth result in the formation of a fine-grained microstructure, after completion of recrystallization. The acquired knowledge has been used to develop a computational modeling technique for simulating microstructural evolution of the alloy. Microstructural states are simulated by integrating analytical approaches in a Monte Carlo algorithm. The effects of deformation-induced and pre-existing inhomogeneities, as well as precipitate coarsening and grain boundary pinning on the competitive recovery-recrystallization process are included in the simulation algorithm. The developed technique is implemented to predict the microstructural evolution during isothermal and non-isothermal annealing of AA6xxx sheets. A good quantitative agreement is found between the model predictions and the results from the experimental investigations.

## ACKNOWLEDGEMENT

I am ever grateful to God whose care, protection and love accompanied me through all my life.

The successful completion of this thesis was made possible through the invaluable contribution of a number of people. First and foremost, I would like to express my sincerest gratitude to my academic supervisor, Dr. Shahrzad Esmaili, who has supported me from the preliminary to the concluding level with her knowledge, guidance and encouragement.

Many thanks and appreciations go to the members of my dissertation committee: Prof. Gary Purdy, Prof. Selva Selvakumar, Prof. Michael Worswick and Prof. Carolyn Hansson for their valuable comments and feedbacks.

I extend my gratitude to Novelis Global Technology Center (NGTC) for the excellence collaborations throughout this work. The financial support from NGTC, NSERC, IAMI, CAMM and OGS are respectfully acknowledged. Dr. Haiou Jin and Dr. Xiang Wang are profusely thanked for their insight and assistance with TEM and EBSD observations. I would like to also genuinely thank Dr. David Lloyd for his comments and the enlightening discussions.

I have learned a lot from pleasant discussions with my fellow graduate students to whom I am truly grateful. I would like to specifically thank Nasim Bakhshi Zadeh, Dan Cluff, Roger Carrick, Brian Langelier and Joyce Lam for their help and friendship, as well as co-op students, Andrew Finkle, Gandhali Joshi and Masroor Hassan who helped me with experimental analysis. I owe my special thanks to my dear friends, Dr. Shahab Ardalan, Negar Rasti, and Juli whose accompany and supports made working at the University of Waterloo a great experience for me.

The last but the most, I would like to thank my family. I am greatly thankful to my aunt, Shahla, for always being there for me. I would like to extend my deepest appreciation to my dear brother, Radin, and his lovely little family, Morvarid and Baran, for their encouragement and for believing in what I was doing. There is no word to describe my immense gratitude to my parents; I can only and humbly be grateful forever. None of this would have been possible without their unconditional love, support, and patience. This thesis, therefore, is dedicated to Simin and Ali, my beloved parents.

# **DEDICATION**

*To my Mom and Dad.*

# TABLE OF CONTENTS

Author's Declaration.....	ii
Abstract .....	iii
Acknowledgement.....	iv
Dedication .....	v
Table of contents .....	vi
List of Tables.....	x
List of figures .....	xi
Nomenclature .....	xvii
Chapter 1. Introduction.....	1
Chapter 2. Literature review .....	4
2.1. Precipitation in Al-Mg-Si-(Cu) alloys .....	4
2.1.1. General precipitation behaviour of AA6xxx aluminum alloys .....	4
2.1.2. Precipitate contribution to yield strength.....	9
2.1.3. Effect of cold work on precipitation .....	10
2.2. Annealing of the deformed material .....	11
2.2.1. The deformed state.....	11
2.2.1.1 Stored energy of deformation.....	12
2.2.1.2 Dislocation distribution after deformation .....	13
2.2.2. Recovery after deformation .....	17
2.2.2.1 Reduction of stored energy during recovery .....	18
2.2.2.2 Recovery of two phase alloys.....	20
2.2.3. Recrystallization .....	22

2.2.3.1 Microstructural evolution during recrystallization.....	22
2.2.3.2 Recrystallization of two phase alloys:.....	24
2.2.3.3 Recrystallization modeling: analytical approach .....	26
2.2.3.4 Recrystallization modeling: computer modeling and simulation.....	27
2.2.4. Annealing of AA6xxx aluminum alloy.....	29
2.3. Grain refinement in AA6xxx .....	32
Chapter 3. Scope and Objective .....	36
Chapter 4. Experimental Methodology .....	37
4.1. Material.....	37
4.2. Thermomechanical processing .....	38
4.3. Experimental methodology.....	41
4.3.1. Differential scanning calorimetry (DSC).....	41
4.3.2. Microhardness measurement .....	41
4.3.3. Transmission electron microscopy (TEM) .....	42
4.3.4. Scanning electron microscopy (SEM) .....	43
4.3.5. Electron backscatter diffraction (EBSD) .....	44
Chapter 5. Experimental results and discussion .....	46
5.1. Results .....	46
5.1.1. Characterization of precipitation behaviour through DSC .....	46
5.2. Characterization of precipitate hardening and annealing softening .....	48
5.2.1. Microstructural characterization through TEM .....	50
5.2.2. Microstructural characterization through SEM.....	66
5.2.3. Microstructural characterization through EBSD.....	70

5.3. Discussion.....	78
5.3.1. Precipitate evolution during non-isothermal annealing .....	78
5.3.2. Dislocation arrangement in the as-deformed state.....	83
5.3.3. Interactions of precipitates and dislocations during annealing .....	84
5.3.4. Microstructural evolution during recrystallization .....	88
5.3.5. Concluding remarks .....	102
Chapter 6. Computational modelling and simulation.....	104
6.1. Computer assisted quantitative analysis of EBSD results .....	104
6.2. Simulating isothermal annealing .....	120
6.2.1. Introduction.....	121
6.2.2. Objective .....	122
6.2.3. Analytical formulation.....	122
6.2.4. Simulation algorithm for isothermal annealing conditions.....	126
6.2.4.1 Generation of deformed structure.....	126
6.2.4.2 Simulating microstructural evolution.....	128
6.2.5. Calibration and implementation of simulation .....	131
6.3. Simulating non-isothermal annealing.....	138
6.3.1. Analytical formulation and assumptions.....	138
6.3.2. Simulation algorithm for non-isothermal annealing .....	140
6.3.2.1 Generation of deformed structure.....	141
6.3.2.2 Simulation microstructural evolution.....	143
6.3.3. Calibration and implementation of the simulation.....	146
6.3.4. Simulation results and discussion .....	153

6.4. Range of applicability and limitation of the model .....	160
Chapter 7. Summary, conclusions and future work.....	162
7.1. Summary and conclusions .....	162
7.2. Future work.....	165
References .....	167
Appendix (A1): Micrographs .....	176
Appendix (A2): Misorientation calculation .....	177

## LIST OF TABLES

Table 4-1 Chemical composition of AA6451 alloy (wt%) .....	38
Table 4-2. Sample identification .....	40
Table 4-3. Identification of the additional TEM samples .....	43
Table 6-1. Analytical equations .....	123
Table 6-2. Calibration parameters for model implementation .....	133
Table 6-3 Material and simulation parameters (non-isothermal simulation).....	152

## LIST OF FIGURES

Figure 2-1. The DSC traces for the as-quenched and different aging conditions of an AA6111 aluminum alloy [19].	5
Figure 2-2 TEM micrographs of an AA6111 aluminum alloy at (a) peak aged condition (7h/180°C) showing presence of $\beta''$ and $Q''$ , (b) overaged (7 days/250°C) showing presence of $Q'$ and precursor of $\beta$ (c) severely overaged (21 days/ 300°C) showing presence of $\beta$ and $Q$ phases; after Wang et. al. [19].	8
Figure 2-3. Schematic view of the a) cutting mechanism, b) Orowan mechanism [34].	10
Figure 2-4. Variation of drag stress with the dislocation velocity [30].	15
Figure 2-5. TEM micrographs showing dislocation substructure in a) pure aluminum after 80% ( $\epsilon= 1.6$ ) cold rolling reduction in thickness [86], b) Al-2.5Mg after 95% ( $\epsilon=3$ ) cold rolling reduction in thickness [87].	17
Figure 2-6. Schematic representation of a mapped microstructure for Monte Carlo simulation [3].	28
Figure 2-7. Schematic representation of typical thermomechanical processing steps in commercial production of AA6xxx aluminum alloy sheets [4].	30
Figure 4-1. Schematic diagram of the processing route for production of cold-rolled sheet from hot-rolled plate: a) hot-rolled 5mm thick plate, b) solutionizing and natural aging of the hot-rolled plate, and c) thickness reduction from 5mm to 1mm through multiple cold rolling passes.	37
Figure 4-2. Schematic presentation of the non-isothermal annealing routes.	39
Figure 5-1. The DSC thermograms for the as-quenched (AQ) and naturally-aged (NA) samples.	47

Figure 5-2. The DSC thermograms for the as-quenched and cold-rolled (AQ-CR), and naturally-aged and cold-rolled (NA-CR), and cold-rolled pure aluminum (Al-CR) samples. ....	48
Figure 5-3. Microhardness evolution of naturally-aged (NA), naturally-aged and cold-rolled (NA-CR), as-quenched and cold-rolled (AQ-CR), and cold-rolled pure aluminum (Al-CR) samples. ....	49
Figure 5-4. Bright field TEM micrograph showing dislocation distribution in the as-deformed (NA-CR) sample (TEM operated by X. Wang). ....	52
Figure 5-5. Bright field TEM micrograph showing dislocation distribution in the NA-CR-180 sample (TEM operated by X. Wang). ....	53
Figure 5-6. TEM micrographs of NA-CR-180-20m a) bright field image and b) dark field image taken at $[001]_{Al}$ zone axis from an identical area of the sample (TEM operated by X. Wang). ....	54
Figure 5-7. Bright field TEM micrograph showing dislocation distribution in the NA-CR-235 sample (TEM operated by X. Wang). ....	55
Figure 5-8. TEM bright field micrograph showing presence of subgrains in the NA-CR-235 sample at different magnification and tilting conditions. For clear observation, the same area of the microstructure is marked by (A) in the micrographs (TEM operated by X. Wang). ....	56
Figure 5-9. TEM micrograph of the NA-CR-235-20m sample showing subgrains formed adjacent to a dispersoid particle with accompanying EDX spectrum (TEM operated by X. Wang). ....	57

Figure 5-10. a) TEM micrographs of NA-CR-235-20m taken at  $[001]_{Al}$  zone axis showing precipitates with rectangular cross-sectional areas (marked B) and circular cross-sectional areas (marked C) (TEM operated by D. Steele)..... 58

Figure 5-11. TEM micrographs of NA-CR-235-20m a) bright field image and b) dark field image (TEM operated by X. Wang)..... 59

Figure 5-12. TEM micrograph of the NA-CR-235-20m sample showing subgrains pinned by precipitates (TEM operated by X. Wang). .... 60

Figure 5-13. Bright field TEM micrograph showing dislocation distribution in the NA-CR-300 sample (TEM operated by X. Wang). .... 62

Figure 5-14. TEM micrographs of the NA-CR-300 sample showing a) subgrains, marked by arrows, b) a recrystallized nucleus, marked by arrow, c) the same area presented in part a) after tilting, and d) the same area presented in part b) after tilting . The same regions of the micrographs (before and after tilting) are marked identically (TEM operated by X. Wang)..... 63

Figure 5-15. TEM bright field micrographs of the NA-CR-300 sample showing recrystallized grains on a pre-existing grain boundary (TEM operated by X. Wang)..... 64

Figure 5-16. TEM bright field micrograph of the NA-CR-300 sample showing a recrystallized grain formed within the deformed structure (TEM operated by X. Wang). .... 64

Figure 5-17. TEM bright field micrographs from different areas showing recrystallized (R) and non-recrystallized (NR) regions in the NA-CR-340-20m sample (TEM operated by D. Steele)..... 65

Figure 5-18. TEM bright field micrographs showing recrystallized structure in the NA-CR-380-20m sample (TEM operated by X. Wang)..... 66

Figure 5-19. Backscattered SEM micrograph showing distribution of dispersoids and constituents in the NA-CR-235 sample.....	68
Figure 5-20. Backscattered SEM image showing recrystallized bands formed in the NA-CR-320 sample.....	68
Figure 5-21. a) Backscattered and b) secondary SEM images of an identical area of the NA-CR-380-20m sample. ....	69
Figure 5-22. Backscatter SEM image of the NA-CR-380-20m sample. Arrows point to grain boundary pinning by precipitates. ....	70
Figure 5-23. EBSD orientation maps of a) NA-CR-180, b) NA-CR-235, c) NA-CR-300, d) NA-CR-320, e)NA-CR-340, and f) NA-CR-380-20m samples (EBSD test performed by H. Jin).....	74
Figure 5-24. EBSD grain boundary maps of a) NA-CR-235, b) NA-CR-300, c) NA-CR-320, d) NA-CR-340 samples ; black $\geq 15^\circ$ , blue = $2^\circ - 15^\circ$ (EBSD test performed by H. Jin). ....	76
Figure 5-25. Grain size distribution calculated from EBSD results on a)NA-CR-340, and b)NA-CR-380-20m samples. ....	77
Figure 5-26. The DSC thermograms for the as-quenched (AQ), as-quenched and cold-rolled (AQ-CR), naturally-aged (NA), and naturally-aged and cold-rolled (NA-CR) samples..	80
Figure 5-27. DSC thermograms and hardness evolution of naturally-aged and cold-rolled (NA-CR), and naturally-aged (NA) samples. ....	83
Figure 5-28. Point to point misorientation distribution along a) dashed line a b) dashed line b and c) dashed line c on the EBSD boundary map of the NA-CR-235 sample.....	90
Figure 5-29. Point to point misorientation distribution along a) dashed line a b) dashed line b and c) dashed line c on the EBSD boundary map of the NA-CR-300 sample.....	91

Figure 5-30. Grain boundary character distribution for the EBSD maps of a) NA-CR-235, b) NA-CR-300, c) NA-CR-320, d) NA-CR-340 and e) NA-CR-380. The dashed line shows the division between high angle and low angle boundaries ( $15^\circ$ ). ..... 95

Figure 5-31. Evolution of high angle grain boundary fraction (HAGB%) as a function of the end annealing temperature of the non-isothermal annealing process..... 95

Figure 5-32. EDX analysis on precipitates in a) a recrystallized area and b) a non-recrystallized area of the NA-CR-340-20 [139]. ..... 101

Figure 6-1. Indexing quality maps generated by Matlab coding based on the measured IQ value for each point of the EBDS maps of a) NA-CR-235, b)NA-CR-300, c)NA-CR-320, d)NA-CR-340 and e)NA-CR-380-20m samples..... 109

Figure 6-2. The schematic distribution of indexing quality for ideal recrystallized and deformed samples..... 111

Figure 6-3. Distribution of indexing quality values for NA-CR-235 and NA-CR-380-20m.. 111

Figure 6-4. Distribution of grain average misorientation values for NA-CR-235 and NA-CR-380-20m. .... 113

Figure 6-5. Grain size distribution in NA-CR-380-20m; comparison of Channel 5 analysis results and computed results..... 115

Figure 6-6. Recrystallized grains maps of a)NA-CR-235, b) NA-CR-300, c) NA-CR-320, d) NA-CR-340, and e) NA-CR-380-20m; non-recrystallized areas are shown in black shade. .... 118

Figure 6-7. Quantified EBSD results showing the evolution of average grain diameter as a function of the end temperature of the non-isothermal annealing process. .... 119

Figure 6-8. Quantified EBSD results showing the evolution of recrystallized fraction as a function of the end temperature of the non-isothermal annealing process. ....	119
Figure 6-9. Stored energy distribution across a deformed grain; the hatched rectangles show areas having the highest 10% of stored energy. ....	128
Figure 6-10. MC simulation of microstructural evolution during annealing at 325°C for a) 35 h, b) 165 h, and c) 600h. ....	132
Figure 6-11. a) Recrystallized area fraction calculated from Improved-MC simulation, Simple-MC simulation and experimental results b) JMAK analysis of Improved-MC simulation, Simple-MC simulation, and experimental results. Experimental results are from Ref. [6]. ....	136
Figure 6-12. Flow chart describing the sequence of steps in simulation for isothermal condition. ....	137
Figure 6-13. Schematic presentation of rule of addition for simulating non-isothermal annealing. ....	141
Figure 6-14. Stored energy distribution across deformed structure. ....	143
Figure 6-15. Non-isothermal simulation results after annealing to a) 180°C, b) 235°C, c) 300°C, d) 320°C, e) 340°C and f) 356°C. ....	154
Figure 6-16. Recrystallized area fraction calculated from Non-isothermal simulation and experimental results. ....	157
Figure 6-17. Average diameter of recrystallized grains calculated from Non-isothermal simulation and experimental results. ....	159
Figure 6-18. Grain size distribution calculated from non-isothermal simulation and experimental results for the fully recrystallized conditions. ....	159

# NOMENCLATURE

$A$	Constant in LSW coarsening equation
$b$	Magnitude of the Burgers vector
$B$	Temperature dependent constant in JMAK equation
$C_0$	Number of atoms per unit volume in the system
$C_{0s}$	Average solute concentration
$C_I$	Concentration of heterogeneous nucleation sites per unit volume in the system
$d_l$	Diameter of the large particles
$D_s$	Solute diffusion coefficient
$E$	Young's modulus
$E_{total}$	Total energy of the system in Monte Carlo simulation
$f_i$	Volume fraction of large particles
$f_{gb}$	Grain boundaries area fraction
$f_{non-recx}$	Non-recrystallized area fraction
$f_{ppt}$	Volume fraction of precipitates
$f_{recx}$	Recrystallized area fraction,
$F_m$	Maximum force that can be sustained by the precipitate against dislocation movement
$G$	Shear modulus
$\dot{G}$	Rate of recrystallized grain growth
$GAM$	Grain Average Misorientation
$GAM_{cr}$	Critical value of Grain Average Misorientation

$\Delta G_{hom}^*$	Activation energy for homogeneous nucleation
$\Delta G_{het}^*$	Activation energy for heterogeneous nucleation
$H$	Deformation stored energy
$H_0$	Stored energy at the start of annealing
$H_{0g}$	Stored energy inside the grains at the start of annealing
$H_{0gb}$	Stored energy associated to grain boundary
$H_{0l}$	Stored energy around large particles at the start of annealing
$H_{dis}$	Energy per unit length of dislocation line
$H_i$	Energy of lattice site $i$ in a mapped microstructure for Monte Carlo simulation
$H_{0g}^{max}$	Maximum value of stored energy inside a grain
$H_{0g}^{min}$	Minimum value of stored energy inside a grain
$IQ$	Indexing quality
$IQ_{cr}$	Critical value of indexing quality
$k$	Boltzman's constant
$k_c$	Constant in LSW coarsening equation
$K_1$	Constant
$l_a$	Activation distance of dislocation
$l_s$	Solute separation
$L$	One lattice site dimension
$L_p$	Average precipitate spacing
$M$	Taylor factor
$M_b$	Grain boundary mobility
$M_{b0}$	Grain boundary mobility constant

$n$	Constant
$n_{dis}$	Number of dislocation nodes
$N$	Total number of lattice sites
$\dot{N}_{het}$	Heterogenous nucleation rates
$\dot{N}_{hom}$	Homogeneous nucleation rates
$N_n$	Nearest neighbours of a selected lattice site
$N_{ppt}$	Number density of precipitates
$N_{rex}$	Number of recrystallized nuclei
$P_{max}$	Maximum pressure on a lattice site of the microstructure
$P_R$	Driving pressure for recrystallization
$Q_A$	Apparent activation energy of coarsening
$Q_M$	Activation energy for boundary migration
$r_0$	Average radius of the precipitates at the start of heat treatment
$r_{ppt}$	Average radius of precipitates during heat treatment
$r_{peak}$	Average precipitate diameter at the peak of aging
$R$	Universal gas constant
$S_i$	Arbitrary orientation of lattice site in a mapped microstructure for Monte Carlo simulation
$t$	Time
$t_0$	Starting time of annealing
$t_1$	Reference annealing time
$t_{cycle}$	Time duration of each Monte Carlo cycle
$t_i$	Summation of $t_{cycle}$ of previous Monte Carlo cycles during which the selected

	site has experienced unsuccessful reorientation attempts
$t_{peak}$	Time to peak-age condition
$T$	Temperature
$T_0$	Temperature of the previous Monte Carlo cycle
$U_r$	Activation energy for recovery
$v$	Velocity of the moving boundary
$v_c$	Critical velocity of dislocations in presence of solute drag
$v_d$	Velocity of dislocations in presence of solute drag
$v_{max}$	Velocity of the fastest moving boundary
$V_r$	Activation volume of recovery
$X_0^i$	Summation of $X_{cycle}^i$ from previous unsuccessful transformation attempts
$X_{cycle}^i$	Distance that grain boundary can move in one Monte Carlo cycle during non-isothermal annealing
$X_{local}$	Distance that a selected recrystallized site can move in one Monte Carlo cycle during isothermal annealing
$X_v$	Transformed volume fraction in JMAK equation
$Z$	Zener pinning effect of precipitates against grain boundary movement
$\alpha$	Constant in Taylor equation
$\alpha_s$	Solute-boundary binding energy constant
$\beta$	Solute drag parameter which depends on elastic constants of the solute and matrix
$\varepsilon$	True strain
$\gamma$	Energy of the high angle grain boundary

$\gamma_\theta$	Energy of the low angle grain boundary
$\Gamma$	Dislocation line tension
$\delta$	Kronecker delta
$\Delta t$	Time interval assigned to each Monte Carlo cycle
$Z$	The unpinned fraction of dislocation network which recover
$\rho$	Dislocation density
$\rho_g$	Dislocation density in the grains
$\rho_l$	Additional dislocations density accumulated around large particles
$\rho_t$	Total dislocation density
$\sigma$	Yield strength
$\sigma_d$	Solute drag stress
$\sigma_{dis}$	Contribution of dislocations to yield strength
$\sigma_{diso}$	Contribution of dislocations to yield strength at the start of annealing
$\sigma_{dm}$	Maximum solute drag stress
$\sigma_i$	Intrinsic strength of aluminum
$\sigma_{ss}$	Contribution from the solid solution strengthening to yield strength
$\sigma_{ppt}$	Contribution from precipitate hardening to yield strength
$\tau_c$	Critical stress required for the dislocation to break free of shearable precipitate
$\tau_{or}$	Critical stress required for the dislocation to break free of non-shearable precipitate
$v_D$	Debby frequency
$\omega$	Heating rate of the non-isothermal annealing process

# Chapter 1. INTRODUCTION

Al-Mg-Si(-Cu), i.e. A6xxx, are the alloys of choice in the automotive industry for lightweight outer panel applications. The use of these alloys is expected to rise in coming years due to the ever-increasing need for significant weight reduction in automotive manufacturing. The widespread application of these alloys, however, will require further research and development activities in various areas related to the processing, process optimization and properties of the alloys. One such area involves developing novel thermomechanical processing routes to achieve sheets with the desired microstructural properties.

Recently, a new thermomechanical processing method (TMPM) has been developed for the grain refinement of AA6xxx aluminum alloys [1]. The main advantage of the new method over the previously developed processes for achieving fine grained structure is its continuous nature and good compatibility with existing industrial production lines. This method consists of a solution treatment, and conventional cold rolling stage that is followed by a non-isothermal annealing process. Upon the successful grain refinement of an AA6xxx aluminum alloy through the TMPM, the primary objectives of this work are assigned as characterizing and modeling microstructural evolution during the non-isothermal annealing stage of the TMPM.

The microstructural evolution during non-isothermal annealing is dictated by the interactions between precipitation, recovery and recrystallization mechanisms. While the microstructure of the deformed material evolves through a competition between recovery and recrystallization for reduction of stored energy of the system, the extent of each of these phenomena is extensively affected by precipitation [2-4]. Precipitation, in turn, is strongly

affected by dislocations and grain boundaries that act as heterogeneous nucleation sites and easy diffusion paths for solutes. The present work aims to identify the underlying mechanism of microstructural evolution during the non-isothermal annealing process and in turn grain refinement through comprehensive investigation of these phenomena and their mutual interactions.

Traditional methods for designing appropriate TMP involve massive trial and error experimental work which results in extensive inefficiency and costly production. To address this issue, physically-based process models are required so that processes, microstructures and properties can be efficiently optimized. Although important attempts in developing models for the prediction of microstructural transformations in precipitation hardenable alloys have recently been made (e.g. [5, 6]), the complexity of the transformations in these alloys cannot be fully addressed through pure analytical approaches.

To overcome this limitation, during the last two decades, much effort has been put into the development of computer simulation methods to describe annealing behaviour (e.g. [7-12]). The main advantage of the computational modeling over pure analytical methods is the ability to include multiple variables as well as the microstructural inhomogeneities. Among different computer simulation techniques, Monte Carlo (MC) is one of the most commonly used techniques for the simulation of annealing phenomena (e.g [7-12]). This method was first employed by Anderson et al. [7] for simulating grain growth. Srolovitz and co-workers [8, 9] modified the initial method and simulated recrystallization. The Monte Carlo technique has since been used by many researchers to simulate different aspects of annealing phenomena (e.g. [10-12]).

This research aims at developing a computational model based on a combination of analytical approaches and a Monte Carlo technique for simulating microstructural evolution during non-isothermal annealing. The goal is to develop a computational model that is backed up with solid physical principles through the analytical approaches and includes the complexity of the system through the Monte Carlo algorithm. The present work is the first approach for computational modeling of microstructural evolution in precipitation hardenable AA6xxx aluminum alloys. The combination of the computational modeling technique and the results of the comprehensive experimental analysis are anticipated to have a significant impact on the development and design of new thermomechanical processing routes for the production of AA6xxx aluminum sheets with tailored properties.

## Chapter 2. LITERATURE REVIEW

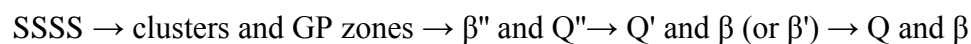
### 2.1. Precipitation in Al-Mg-Si-(Cu) alloys

Precipitation hardenable Al-Mg-Si-(Cu), i.e. AA6xxx aluminum alloys, are widely used as medium strength structural alloys due to their light weight combined with good mechanical and surface properties [13, 14]. The composition of many commercial 6xxx alloys includes Cu as another alloying element (in addition to Mg and Si), which increases the rate of precipitation [15, 16]. In this section, initially, the general precipitation behaviour of AA6xxx aluminum alloys will be presented, then, precipitation hardening and the effect of cold work prior to aging treatment on precipitation behaviour of the alloys will be described.

#### 2.1.1. General precipitation behaviour of AA6xxx aluminum alloys

The age-hardening response of Al-Mg-Si-(Cu) alloys is remarkable, and therefore, control of precipitation during heat treatment is crucial for attaining optimal alloy microstructure. The precipitation behaviour of AA6xxx aluminum alloys has been extensively studied in the past (e.g. [13, 14, 16-19]). In this review only those studies which are specifically related to this research will be reviewed.

Based on a recent study on AA6111 [19], the precipitation sequence of the alloy is suggested as:



SSSS and GP zones represent supersaturated solid solution and Guinier–Preston zones (small highly coherent precipitates), respectively [20, 21]. Metastable  $\beta''$  and  $\beta'$  are the precursors of the square-shaped stable phase  $\beta$  with the chemical composition of  $\text{Mg}_2\text{Si}$  [22]. Similarly,  $Q''$  and  $Q'$  are the metastable phases and precursors of the lath shaped stable phase  $Q$ , composed

of Al, Cu, Mg and Si [13, 19, 25-28]. The precipitation sequence of the alloy has been determined through a combination of DSC and TEM analysis. The DSC traces of AA6111 alloy at different aging conditions are presented in Figure 2-1. The TEM micrographs in Figure 2-2, show precipitates which form at various stages of aging in AA6111 aluminum alloy.

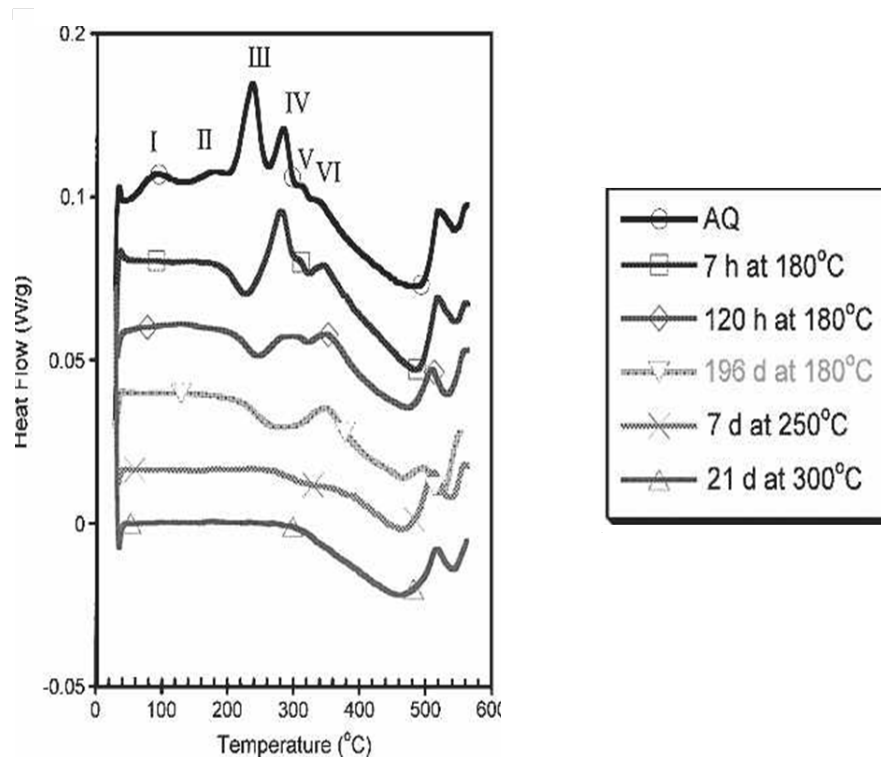


**Figure 2-1. The DSC traces for the as-quenched and different aging conditions of an AA6111 aluminum alloy [19].**

In general, nucleation of precipitates in the matrix can occur either homogeneously within the grains or heterogeneously on various microstructural defects such as dislocations, existing second phase particles and grain boundaries [29, 30]. The nucleation mechanism depends on the level of the driving force available for the process, which in turn, depends on

the degree of supersaturation. The relative magnitude of heterogeneous and homogeneous nucleation rates,  $\dot{N}_{het}$  and  $\dot{N}_{hom}$ , respectively, can be given in a simple relation as [29]:

$$\frac{\dot{N}_{het}}{\dot{N}_{hom}} = \frac{C_1}{C_0} \exp\left(\frac{\Delta G_{hom}^* - \Delta G_{het}^*}{kT}\right) \quad (2-1)$$

where  $\Delta G_{hom}^*$  and  $\Delta G_{het}^*$  are the activation energies for homogeneous and heterogeneous nucleation, respectively;  $C_0$  and  $C_1$  the number of atoms and the concentration of heterogeneous nucleation sites per unit volume in the system, respectively;  $k$  is the boltzman's constant and  $T$  is the temperature of reaction. As  $\Delta G_{het}^*$  is always smaller than  $\Delta G_{hom}^*$ , the exponential factor in the Equation (2-1) is larger than unity and, as a result, favours heterogeneous nucleation. However, the factor  $(C_1/C_0)$  is always less than unity and promotes homogeneous nucleation. Therefore, the dominant nucleation process depends on the aging temperature and is dictated by the balance between these two terms of the Equation (2-1).

After formation of a stable nucleus, the addition of any further atoms results in a decrease of free energy and the nucleus will grow. Esmaeili and Lloyd [31] have introduced a simple modeling relationship to predict the average size of precipitates,  $r_{ppt}$ , during artificial aging of a pre-aged material, assuming that the precipitates that form during the pre-aging treatment act as nuclei for the “growth-controlled” precipitation process during artificial aging. The relationship for spherical precipitates can be given by:

$$r_{ppt} = \left(\frac{f_r}{f_r^o}\right)^{1/3} r_o \quad (2-2)$$

where  $r_o$  is the average radius of the precipitates at the start of artificial aging,  $f_r$  and  $f_r^o$  are the relative volume fraction of precipitates during and at the start of artificial aging, respectively. It should be mentioned here that Equation (2-2) is only valid up to the peak strength. Aging beyond the peak strength results in coarsening of larger particles and the dissolution of smaller

ones, which leads to the decrease in free energy of the system [29]. To estimate  $r_{ppt}$  beyond the peak (during overaging), Esmacili et. al. [31] have adapted Lifshiz-Slyozov-Wagner (LSW) [32] theory for precipitate coarsening and used the following equation:

$$r_{ppt}^3 - r_{peak}^3 = k_c(t - t_{peak}) \quad (2-3)$$

In the above equation,  $r_{peak}$  is the average precipitate diameter at the peak of aging and  $t$  and  $t_{peak}$  are the time beyond the peak-aged condition and the time to reach peak of aging, respectively. The rate constant  $k_c$  can be calculated as:

$$k_c = \frac{A}{T} \exp\left(\frac{-Q_A}{RT}\right) \quad (2-4)$$

where  $A$  is a constant factor,  $Q_A$  is an apparent activation energy and  $R$  is the universal gas constant.

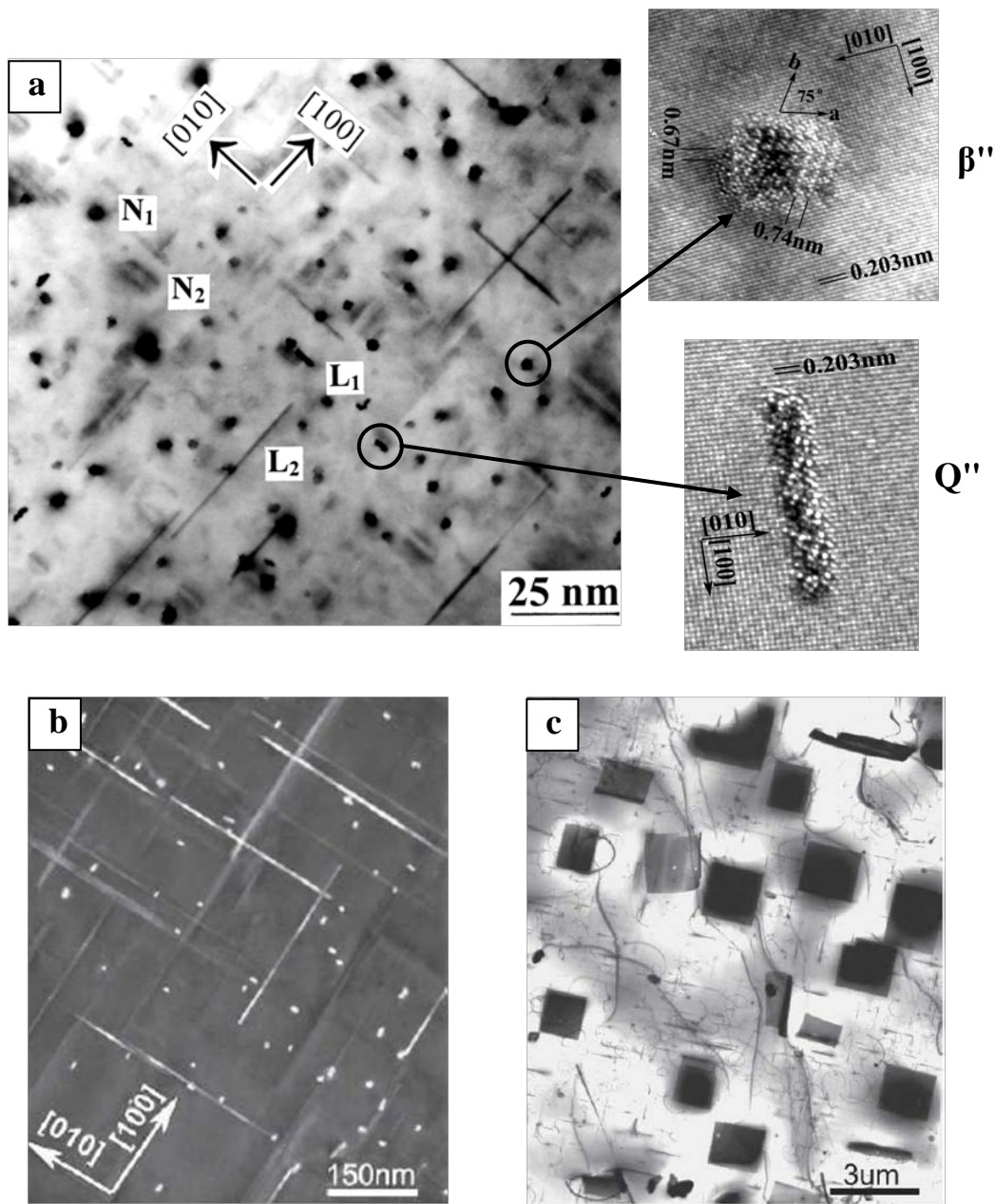


Figure 2-2 TEM micrographs of an AA6111 aluminum alloy at (a) peak aged condition (7h/180°C) showing presence of  $\beta''$  and  $Q''$ , (b) overaged (7 days/250°C) showing presence of  $Q'$  and precursor of  $\beta$  (c) severely overaged (21 days/ 300°C) showing presence of  $\beta$  and  $Q$  phases; after Wang et. al. [19].

### 2.1.2. Precipitate contribution to yield strength

By precipitation of clusters and GP zones at the very early stages of precipitation, the hardness and strength of AA6xxx alloys increase [13, 17-19, 32]. The maximum precipitation hardening in Al-Mg-Si-(Cu) alloys is obtained in the presence of  $\beta''$  [13, 17] or both  $\beta''$  and  $Q''$  in copper-bearing alloys such as AA6111 [18, 19]. Further aging of the alloy results in the formation of more stable phases, precipitate coarsening, and decreases in precipitate hardening effect [13, 18, 19, 31].

The precipitation hardening theories have been reviewed in detail in the past decades [33-35]. The usual approach to treat the hardening phenomenon associated with precipitation is to consider the particles as an array of point obstacles interacting with dislocations. Once a gliding dislocation line encounters the array of precipitates, it bows out. By increasing the applied stress the bowing angle becomes smaller until it reaches a critical value at which the obstacle is overcome and the dislocation can move forward. When the critical breaking angle is large, precipitates are considered as weak shearable obstacles and will be cut by the moving dislocation line, as schematically shown in Figure 2-3(a). For the case of strong non-shearable precipitates Figure 2-3(b), strengthening is controlled by the Orowan mechanism where the critical breaking angle becomes zero, the two positive and negative segments of the dislocation line annihilate one another and a loop is formed around the precipitate. In a recent study on Al-Mg-Si-Cu alloy, it has been shown that precipitates which form at early stages of aging, i.e.  $\beta''$  and  $Q''$  are shearable and the more stable phases which form during later stages of aging are non-shearable [36].



Figure 2-3. Schematic view of the a) cutting mechanism, b) Orowan mechanism [34].

### 2.1.3. Effect of cold work on precipitation

Introduction of deformation prior to the heat treatment process can significantly influence precipitation behaviour (e.g. [2, 36-46]). Dislocations formed during deformation prior to aging provide heterogeneous nucleation sites for precipitation [2, 39, 40] and act as short circuit paths for solute diffusion [41-43]. Precipitation in a deformed structure is a competitive/additive process between bulk homogeneous precipitation and precipitation on dislocations. Studies on precipitation behaviour of deformed AA6xxx aluminum alloys have shown that other than cluster formation at room temperature, nucleation and growth of the intermediate phases are highly accelerated by cold deformation [4, 45-53]. Dislocations which are introduced before natural aging are believed to serve as sinks for quenched-in vacancies [49, 50, 52-55] that are essential for clustering activities [56]. Birol [49] and Shen et. al. [54] have reported that deformation may prevent clustering at room temperature and retard precipitation kinetics in the as-quenched condition [49, 54]. On the other hand, dislocations assist nucleation of  $\beta''$  precipitates and result in the achievement of the peak of aging in pre-deformed AA6xxx faster than in un-deformed conditions [40, 45, 50, 52, 57, 58].

## **2.2. Annealing of the deformed material**

During deformation, the free energy of a metallic material increases by the formation of dislocations and interfaces. A material at such a high level of free energy is thermodynamically unstable and the defects should disappear [3, 29, 30]. However, the transformation is very slow at low temperatures and the unstable defects are retained after deformation. Heating the deformed material to high enough temperatures, i.e. annealing, annihilates or rearranges the defects and, as a result, lowers the free energy of the material. During annealing, microstructure, mechanical and physical properties of the deformed material are restored to their original values [3]. Traditionally annealing has been categorized into recovery, recrystallization and grain growth. In this section, the first two stages of annealing, i.e. recovery and recrystallization, the deformed state, and annealing behaviour of AA6xxx alloys will be reviewed.

### **2.2.1. The deformed state**

The main driving force for microstructural changes during recovery and recrystallization originates from the decrease in the density of dislocations formed during deformation. Therefore, it is very important to understand the nature of dislocation accumulation during deformation which defines the stored energy of the system and the driving force for both recovery and recrystallization. In this section, first the dislocation distribution in single phase metals is reviewed and then the effect of second phase particles on dislocation accumulation will be discussed.

### 2.2.1.1 Stored energy of deformation

The essential difference between the deformed and the annealed states lies in the dislocation content and their arrangement [3, 59]. The increase in dislocation density during deformation arises from the trapping of existing dislocations at obstacles as well as the generation of new dislocations. Dislocation accumulation results in an increase in the yield strength of the alloy. The contribution of dislocation to yield strength,  $\sigma_{dis}$ , is related to the dislocation density,  $\rho$ , through the Taylor equation [60]:

$$\sigma_{dis} = \alpha M G b \rho^{0.5} \quad (2-5)$$

where  $\alpha$  is a constant,  $M$  is the Taylor factor,  $b$  is the magnitude of the Burgers vector and  $G$  is the shear modulus. For a dislocation density  $\rho$ , the stored energy is defined as [3]:

$$H = \rho H_{dis} \quad (2-6)$$

where  $H_{dis}$  is the energy per unit length of dislocation line formulated as [3]:

$$H_{dis} = 0.5 G b^2 \quad (2-7)$$

substituting Equation (2-7) in Equation (2-6), the stored energy is given by:

$$H = 0.5 \rho G b^2 \quad (2-8)$$

For the case of precipitation hardenable alloys, in addition to dislocations, precipitates contribute to yield strength as well. Cheng et. al. [61] proposed that a general form of the flow stress addition law may be taken to include the solid-solution-strengthening component, precipitation and dislocation hardening contributions in yield strength:

$$\sigma = \sigma_i + \sigma_{ss} + (\sigma_{ppt}^n + \sigma_{dis}^n)^{1/n} \quad (2-9)$$

where  $\sigma_i$  is the intrinsic strength of aluminum,  $\sigma_{ss}$ ,  $\sigma_{ppt}$  and  $\sigma_{dis}$  are the contribution from the solid solution, precipitates and dislocations to yield strength and  $n$  is a constant which can vary between 1 and 2. In the presence of a high density of weak obstacles and low density of strong

obstacles,  $n=1$ . This condition corresponds to the early stages of precipitation when there is a high density of weak precipitates. On the other hand, for the later stages of aging most of the precipitates are strong and  $n$  is equal to 2. At intermediate cases, the appropriate value of  $n$  falls between 1 and 2.

Most industrial alloys, such as AA6xxx aluminum alloys, contain particles in addition to precipitates. If particles are present during deformation, they may affect the density and distribution of dislocations in the microstructure and, in turn, its subsequent annealing behaviour [2-4, 62, 63]. The extent of the effect of particles depends on their average size and volume fraction. In deforming matrix that contains large non-deformable particles, as was shown by Ashby [62, 63], there will be a strain incompatibility between the two phases. This incompatibility can be accommodated by the generation of dislocations at the particle-matrix interface. The density of additional dislocations, i.e.  $\rho_l$ , may be estimated from the volume fraction,  $f_l$ , and diameter of the particles,  $d_l$ , through Equation (2-10) [62, 63]:

$$\rho_l = \frac{6\varepsilon f_l}{bd_l} \quad (2-10)$$

where  $\varepsilon$  is the true strain of deformation.

### **2.2.1.2 Dislocation distribution after deformation**

The annealing behaviour of a deformed material not only depends on the overall dislocation density, but more importantly on its distribution. The distribution of dislocation in the as-deformed condition is determined by the process of dislocation generation during deformation, and dislocation rearrangement through dynamic recovery. In metals with high stacking fault energy, such as pure aluminum, dislocations may reach a low energy configuration by forming cells and subgrains [64-67]. Dislocation cells and subgrains are products of dynamic recovery and will therefore be generally affected by any parameters

which alter dislocation movement and generation. Addition of alloying elements can affect dislocation distribution in a deformed structure [3, 68]. This effect may be due to the presence of solute in a solid solution condition or precipitation of the second phase in precipitate hardenable alloys.

The effect of solutes on reducing the size of dislocation cells in deformed material has first been reported by Gay and his co-workers [69, 70]. Solute atoms may act as point obstacles to moving dislocations for slow-diffusing solutes [71-74]. However, when the solute diffusion is significant, the elastic interactions between the solutes and dislocations lead to solute segregation around the dislocations, formation of so called Cottrell atmospheres [75] and depletion of solute elsewhere. Under external forces, a dislocation surrounded by an atmosphere starts to move and leave the atmosphere behind. As a result, a force is exerted by solutes pulling the dislocation back to its original position at the center of the atmosphere. The magnitude of this retarding force is a function of dislocation velocity [30, 75, 76]. At both very high and very low velocities, the drag-stress is very small. At extremely high dislocation velocities, the dislocation passes by the solute atoms at such a fast rate that there is insufficient time for the atoms to rearrange themselves. Under these conditions, the solute atoms can be considered as a set of fixed obstacles through which the dislocation moves. The drag stress reaches a maximum value,  $\bar{\sigma}_{dm}$ , at a critical velocity  $v_c$  [30, 75, 76], as schematically shown in Figure 2-4. The values of  $\bar{\sigma}_{dm}$  and  $v_c$ , can be approximated through Equation (2-11) and (2-12):

$$\sigma_{dm} = 17C_{os}N\frac{\beta}{b} \quad (2-11)$$

$$v_c \cong \frac{4D_s kT}{\beta} \quad (2-12)$$

where  $N$  is the number of atoms per unit volume,  $C_{0s}$  is the average solute concentration, and  $D_s$  is the solute diffusion coefficient;  $\beta$  is a parameter that depends on elastic constants of the solute and matrix, the volume change caused by the solute atom, and the strength of dislocation [75, 76]. The stress, i.e.  $\sigma_d$ , to move the dislocation at slower speed, i.e.  $v_D$ , can be roughly estimated as [75]:

$$\sigma_d = \left(\frac{v_D}{v_c}\right)\sigma_{dm} \quad (2-13)$$

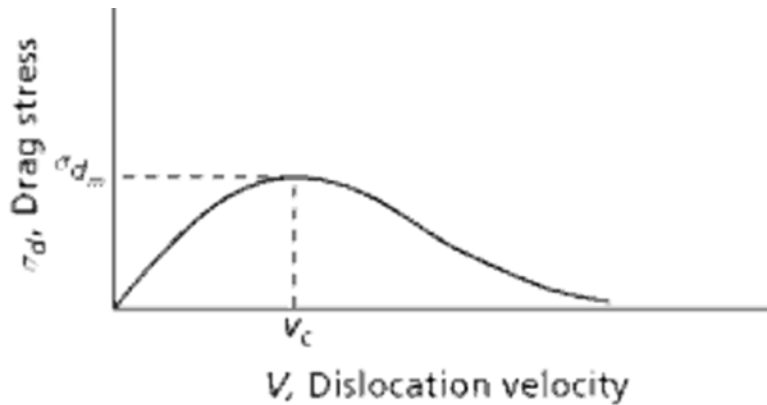


**Figure 2-4. Variation of drag stress with the dislocation velocity [30].**

Various alloying elements have different influences on the rate of dynamic recovery. The effects of magnesium [77-82] and copper [82-85] on reducing the rate of dynamic recovery in aluminum alloys has been frequently reported in literature. Even relatively low level alloying of aluminum with magnesium or copper has been shown to result in remarkable changes in the rate of dynamic recovery compared to pure aluminum [82]. Such an effect has often been attributed to the influence of the alloying elements on the reduction of stacking fault energy and the restriction of dislocation cross-slip during recovery and, in turn, dislocation cell formation (e.g. [78, 86]). However, the main effect on inhibiting cell structure

formation during recovery, has been shown to be due to the drag of solute atmospheres [68, 82]. Dislocation substructure in pure aluminum and Al-2.5Mg alloy after 80% and 95% reduction in thickness through cold rolling are presented in Figure 2-5. It is seen that while, defined cells/subgrains form in the as-cold rolled pure aluminum [86], in the Al-2.5Mg alloy [87], dislocation are arranged in dense wavy tangles.

The presence of second phase particles (in the form of precipitates or dispersoids/constituents) during deformation may also influence dislocation rearrangement by impeding dislocation movement [2, 75, 84, 87, 88, 92]. Dislocations can only pass particles if the local stress overcomes their retarding effect. Therefore, dislocations will be free to move in the regions between particles and will be hindered at particles. Recovery processes that take place on a scale smaller than the interparticle spacing will be unaffected, but recovery processes involving rearrangement of dislocations on a scale larger than the interparticle spacing will be retarded [3, 75]. In a precipitate hardenable alloy, the effect of precipitates on dynamic recovery becomes more complicated owing to the fact that precipitation of second phase particles results in a decrease of supersaturation and, as a result, reductions in the solute drag effect. The overall effect of precipitates is complicated as precipitates influence dislocation storage through four different ways: (a) by influencing the mean free path of dislocations [84, 88], (b) by acting as obstacles against dislocation movement [75], (c) by introducing additional dislocation storage mechanisms [89] and (d) by influencing the rate of dynamic recovery through depletion of solutes in the matrix [90]. After deforming an AA6xxx aluminum alloy, which had been heat treated to the peak aged condition prior to deformation, to a very high level of strain (up to 4.2), shearing of precipitates by dislocations has been observed [46, 91]. Precipitate shearing has been seen to result in dissolution of precipitates

during deformation and the structure and properties of the material are seen to be identical with those of the supersaturated solid solution [46, 91]. Precipitate shearing has been also reported for underaged Al-Mg-Si alloy after 70% cold rolling, but no evidence for extensive amount of dissolution is provided [2]. At lower level of deformation, effect of precipitates is mainly dictated by their size and shape. Wang et. al. [92] showed formation of two different dislocation arrangements after 40% cold rolling of overaged, and severely overaged AA6xxx alloys. The result of this research showed that the material containing fine lath-shaped particles stored dislocations with a very uniform distribution, but the material containing large plate-shaped precipitates produced a dislocation cell structure.

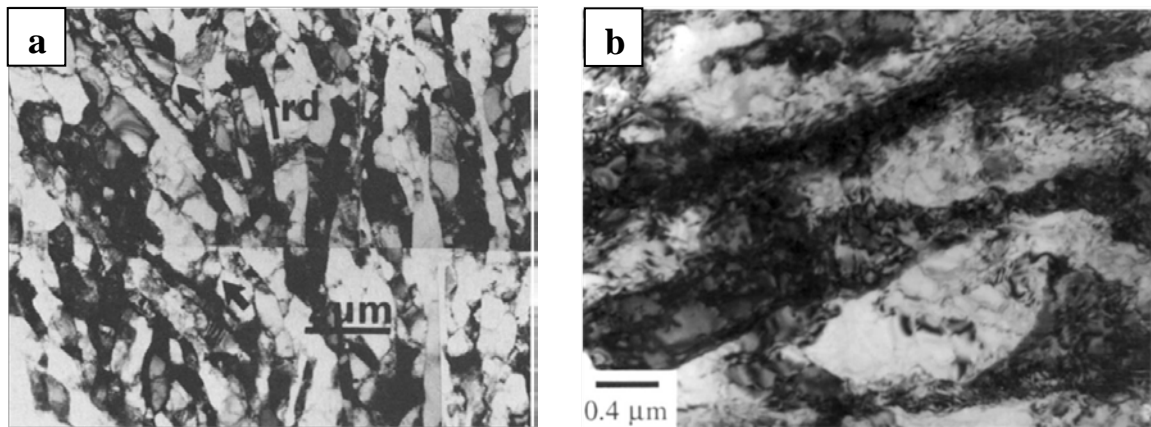


**Figure 2-5. TEM micrographs showing dislocation substructure in a) pure aluminum after 80% ( $\epsilon=1.6$ ) cold rolling reduction in thickness [86], b) Al-2.5Mg after 95% ( $\epsilon=3$ ) cold rolling reduction in thickness [87].**

### **2.2.2. Recovery after deformation**

Recovery refers to all thermally activated processes of dislocation rearrangement in the deformed microstructure that do not involve the sweeping of the deformed structure by migrating high-angle grain boundaries [3]. In this section, first reduction of stored energy

during recovery is summarized and then the effect of second phase particles on the progress of recovery will be discussed.

### **2.2.2.1 Reduction of stored energy during recovery**

Recovery is the first stage of annealing, which involves a gradual decrease in the stored energy of the system through dislocation movement [3, 30, 88]. Decrease of stored energy is achieved as a result of annihilation and rearrangement of dislocations into a lower energy configuration through a combination of glide, climb and cross-slip. In principle, depending on the material, the nature of deformation and the annealing temperature, one of these dislocation movement phenomena can be the dominant mechanism that controls the rate of recovery [88]. These controlling mechanisms are briefly described as follows [88, 93]:

- **Glide control:** Softening process is controlled by the glide of heavily jogged screw dislocations.
- **Climb control:** For this situation, the glide of dislocations into climb position is so rapid that the slower climb process will determine the rate of dislocation movement.
- **Cross-slip (Annihilation controlled):** Dislocations transport to a configuration where the annihilation reaction becomes the rate controlling mechanism.

Progress of recovery through any of the above mechanisms results in the softening of the deformed material. The softening process during recovery may be modeled based on the total dislocation density as a single internal state variable [86, 94, 95]. In such a modeling approach, recovery is assumed to be a thermally activated process, and internal stress relaxation assumed to occur due to dislocation rearrangement and annihilation. The evolution of yield strength during recovery is, then, formulated as [86, 94, 95]:

$$\sigma = \sigma_0 - \frac{kT}{V_r} \ln \left( 1 + \frac{t}{t_1} \right) \quad (2-14)$$

where  $\sigma$  is the yield strength at  $t$  time of annealing,  $\sigma_0$  is the yield strength at the start of recovery,  $V_r$  is the activation volume of recovery, and  $t_1$  is a reference time given by [86]:

$$t_1 = \frac{kT}{K_1 V_r} \exp((U_r - V_r \sigma_0)/kT) \quad (2-15)$$

where  $K_1$  is a constant and  $U_r$  is the activation energy for recovery. The value of the activation energy depends on the operating diffusional mechanisms and varies from the activation energy of pipe-diffusion to the activation energy of self (or solute) bulk diffusion [88]. Activation volume is the volume physically swept by a dislocation from an equilibrium state to an activated state after deformation. In the case of a thermally-activated process, the activation volume term,  $V_r$ , is equal to  $b^2 l_a$ , where  $l_a$  is activation distance, the magnitude of which depends on the rate controlling mechanism during recovery. In case of glide controlled recovery,  $l_a$  is equal to the distance between jogs; for climb controlled,  $l_a$  is equal to the magnitude of Burgers vector; and for cross slip (annihilation controlled)  $l_a$  is of the order of  $b$  [88].

In addition to the above reported recovery model, Nes [88] also proposed a recovery model where microstructural evolution is represented by two parameters: i) dislocation density within cells/subgrains and ii) size of the cell/subgrain. The fundamental difference between the two models arises from the fact that in the latter model, the softening effect is attributed to the role of subgrain evolution during recovery, while in the formerly discussed model, recovery occurs by the re-arrangement and annihilation of randomly distributed forest dislocations.

### 2.2.2.2 Recovery of two phase alloys

Alloying elements and impurities in the form of solute or second phase particles affect the process of recovery. Second phase particles may be in the form of i) precipitates whose volume fraction and size evolves during annealing [18, 19, 96], or ii) dispersoids and constituent particles which remain unchanged during transformation [4, 97-99]. The matrix of AA6xxx aluminum alloys includes both types of the particles [2, 96]. Precipitation and recovery interact in three different ways [3]: i) recovery reduces heterogeneous nucleation sites for precipitation by reducing dislocation density, ii) precipitates pin dislocations and retard progress of recovery, and iii) precipitation results in the reduction of solute content and affects the progress of recovery. As the effect of dislocations on precipitate nucleation has been discussed in Section 2.1.3, only the last two effects are discussed in this section.

The extent of the retarding effect of precipitate against dislocation movement depends on the type of dislocation-precipitate interaction. For shearable precipitates, the critical stress required for the dislocation to break free of the precipitate,  $\tau_c$ , is formulated as [100]:

$$\tau_c = \frac{Gb}{L_p} \left( \frac{F_m}{2\Gamma} \right)^{3/2} \quad (2-16)$$

where,  $L_p$  is the average precipitate spacing,  $\Gamma$  is the dislocation line tension, and  $F_m$  is the maximum force that can be sustained by the precipitate. It should be noted that for shearable precipitates,  $F_m$  is not constant and in fact is proportional to the precipitate radius. For non-shearable precipitates, on the other hand, where precipitates interact with dislocation through Orowan mechanism,  $F_m=2\Gamma$  and Equation (2-16) is reduced to [100]:

$$\tau_{Or} = \frac{Gb}{L_p} \quad (2-17)$$

where  $\tau_{Or}$  is the critical stress required for the dislocation to break free of non-shearable precipitate. In a recent work, Zurob et. al. [5], the effect of precipitation on recovery is modelled by assuming that a certain fraction of the dislocation network is pinned by precipitates and is not available for recovery. The unpinned fraction of dislocation network which recover, i.e.  $\zeta$ , is given by:

$$\zeta = 1 - \frac{n_{ppt}}{n_{dis}} \quad (2-18)$$

where  $n_{ppt}$  is the number of precipitates and  $n_{dis}$  is the number of dislocation nodes which can be approximated by  $\approx 0.5\rho^{1.5}$ .

The effect of solute elements on the softening kinetics through recovery, may be included in recovery modeling and equations by considering their effects on activation volume and activation energy for recovery [88,93]. When solute drag is the rate controlling mechanism, the activation distance, i.e.  $l_a$ , will be determined by solute separation, i.e.  $l_a = l_s$  where  $l_s$  according to Furu et. al. [101] can be approximated to be inversely proportional to the solute concentration:  $l_s = Const./C_s$ . In the presence of solute atoms, depending on the solute element, activation energy for recovery varies between the self-diffusion activation energy for the solvent atoms and the activation energy for diffusion of the solute atoms in the matrix [102].

In AA6xxx aluminum alloy, the average diameter and number density of constituents and dispersoids is remarkably smaller than precipitates. Therefore their effect on retardation of recovery compared to precipitates is negligible. The main effect of these particles arises from their effect on dislocation distribution and its subsequent effect on nucleation of recrystallization which are discussed in Section 2.2.1.1 and 2.2.3.2, respectively.

### **2.2.3. Recrystallization**

Recrystallization is the formation of new dislocation free grains within the deformed material by the development and migration of high angle grain boundaries [3, 29, 30]. In the following two sections, first microstructural evolution during recrystallization and then the effect of second phase particles on recrystallization will be reviewed.

#### **2.2.3.1 Microstructural evolution during recrystallization**

Recrystallization of plastically deformed metals and alloys is of interest for two main reasons. The first is the softening and ductility restoration during recrystallization [3, 30, 103]; the second is the control of the grain structure of the product [96, 104-107]. Recrystallization may occur discontinuously within the deformed structure through nucleation and growth [3, 103]. Alternatively, new grain formation may occur uniformly throughout the deformed microstructure with no distinguishable nucleation and growth stages [108, 109]. This latter type of recrystallization is called continuous recrystallization [3, 103, 108, 109-111]. As described by Humphreys and Hatherly [3], “the discontinuous recrystallization and continuous recrystallization terms are considered as pure phenomenological, describing the spatial and temporal heterogeneity of microstructural evolution during annealing, but not the micro-mechanisms”. In this research, the term “recrystallization” refers to “discontinuous recrystallization” unless otherwise noted.

Recrystallization nucleation is the formation of low internal energy crystallites that are fully/partially separated by high angle grain boundaries from the matrix [3, 103, 112]. An important feature of recrystallization nuclei is that they are not, unlike nuclei of phase transformations, formed by the thermal fluctuation of atoms [3, 103, 112]. In the classical nucleation theory developed for phase transformation, nuclei form through atom by atom

construction [29, 30], whereas the nuclei from which recrystallization initiate are the pre-existing small volumes in the microstructure [3, 103, 112, 113]. Nucleation of recrystallization is technically the result of the growth of small regions (subgrains or cells) that are already present in the structure. Only subgrains/cells with mobile grain boundaries can grow and transfer to recrystallization nuclei. The boundaries of subgrains/cells which have a high misorientation angle to the adjacent recovered or deformed structure have enough mobility to move and grow. Therefore, nuclei form most often in regions where a high angle grain boundary is either already present or is more easily formed [3, 103, 112, 113].

Once the nucleus is formed, it grows into the surrounding structure. By the growth of the new grain, the migrating boundary sweeps out the dislocations and the dislocation-free region expands into the previously deformed or recovered structure [3, 103, 112, 113]. The growth stage is relatively straightforward, and, at a microscopic level, it is a process of grain boundary migration. The boundaries move in response to a driving pressure ( $P$ ) which arises from stored dislocations or from the energy of the boundaries in the material. Velocity of the moving boundary ( $v$ ), depends on the boundary mobility and the driving pressure on the boundary as given by [3]:

$$v = M_b P \tag{2-19}$$

where  $M_b$ , the boundary mobility, is usually assumed to vary with temperature according to:

$$M_b = M_{b0} \exp\left(-\frac{Q_M}{RT}\right) \tag{2-20}$$

where  $M_{b0}$  is a material property constant [3, 114], and  $Q_M$  is the activation energy for boundary migration.

### 2.2.3.2 Recrystallization of two phase alloys:

In two-phase alloys, recrystallization behaviour is influenced by the presence of second phase particles as well as solute elements [2, 4, 96, 102, 104]. The effect of second phase particles is dictated by their size [3, 4, 96, 102, 104]. While large particles enhance recrystallization, small particles, may impede progress of recrystallization [2, 4, 96, 102, 104]. Following Section 2.2.2.2, the effect of small particles is described by considering the precipitate effect. Recrystallization and precipitation interacts in four distinct ways [3]: i) recrystallization decreases dislocation density, and as a result, the potential sites for precipitation; ii) Precipitates retard progress of recovery and as a result affects the amount and distribution of stored energy of the system which is the driving force for recrystallization; iii) precipitates pin grain boundaries and hinder recrystallization; iv) precipitation changes the amount of the solutes and, consequently, mobility of grain boundaries. In this section, pinning of grain boundaries by precipitates, as well as the effect of solute atoms on grain boundary mobility will be discussed, as the other two effects have been described in Section 2.1.3 and 2.2.2.2.

When a boundary intersects a precipitate, the precipitate effectively removes a region of boundary equal to the intersection area and thus the energy of the system is lowered. This reduction in energy drives the grain boundary attraction to the precipitates and, in turn, pinning of the boundary by precipitate [3, 30, 115]. Precipitate pinning of the grain boundaries provides a force against boundary movement; this effect is known as Zener drag [115]. For a volume fraction  $f_{ppt}$  of randomly distributed spherical precipitates of radius  $r_{ppt}$ , the pinning pressure exerted by the precipitates on unit area of the boundary,  $P_Z$ , is given by:

$$P_Z = \frac{3f_{ppt}\gamma}{2r_{ppt}} \quad (2-21)$$

where  $\gamma$  is the energy of the boundary. This relationship was first proposed by Zener in 1948 and was later confirmed by computer simulation [76].

Large particles can promote recrystallization by introducing additional nucleation sites [3, 96, 103, 104, 112]. Particle stimulated nucleation (PSN) takes place in the so-called deformation zones that form through dislocation accumulation around large particles during deformation as explained in Section 2.2.1.2. The PSN activity after cold deformation is influenced by the amount of cold work and the particle size where a decreasing amount of deformation requires an increased particle size for PSN to be effective.

Many commercial alloys contain both large and small particles. The presence of small particles reduces the efficiency of large particles for acting as PSN sites. In such a situation, the driving pressure of recrystallization,  $P_R$ , is offset by the Zener pinning pressure,  $P_Z$ , and the critical particle size for acting as a PSN site is given by [4]:

$$d_l = \frac{2\gamma}{P_R - P_Z} \quad (2-22)$$

The above relationship shows that due to precipitate pinning, a larger particle is required for PSN compared to conditions where small particles are not present.

In metallic alloys, grain boundary migration is affected by the presence of solute atoms [114, 116]. The interaction with solutes is due to the free or excess volume at grain boundaries which is associated with less dense atomic packing than in a perfect crystal [3]. Interaction of solute and grain boundaries results in the formation of a solute atmosphere around the grain boundary which reduces grain boundary mobility [3, 114, 116]. According to the theory of

Cahn [116], for a moving grain boundary with solute drag, the grain boundary mobility is given by:

$$M_b = \left( \frac{1}{M_b} + \alpha_s C_{os} \right)^{-1} \quad (2-23)$$

In this equation,  $C_{os}$  is the bulk solute concentration and the constant  $\alpha_s$  is a function of solute-boundary binding energy, and solute diffusion.

### 2.2.3.3 Recrystallization modeling: analytical approach

The most widely used analytical approach to describe the evolution of the volume fraction of recrystallized grains,  $X_v$ , with respect to time is based on the so-called JMAK methodology, which was developed by Johnson and Mehl [117] Avrami [118-120] and Kolmogorov [1221]. The JMAK model assumes random nucleation of new grains, growth of grains as spheres and a constant growth rate of all grains. The simple JMAK equation is written as:

$$X_v = 1 - \exp(-Bt^n) \quad (2-24)$$

where  $B$  is a temperature dependent constant and  $n$  is a numerical temperature independent exponent. Although JMAK analysis is easy to understand and apply, the assumptions made in the JMAK model are highly simplified compared with what is observed in recrystallization experiments [3, 122]. The simple JMAK equation has been modified to include the variation of growth rate with time as given by equation [123]:

$$X_v = 1 - \exp \left[ -\frac{4}{3} \pi N_{rex} \left( \int_0^t G dt \right)^3 \right] \quad (2-25)$$

where,  $N_{rex}$  is the number of recrystallized nuclei and  $\dot{G}$  is the growth rate. The modified JMAK equation has been employed in developing a recrystallization model that includes

concurrent effects of recovery and precipitation on the variation of growth rate during recrystallization [5]. However, random nucleation and spherical growth of the grains have been kept as the main assumptions of the model [5]. The same technique has been subsequently employed to predict recrystallization behaviour of AA6111 aluminum alloy [6].

#### **2.2.3.4 Recrystallization modeling: computer modeling and simulation**

Computational modeling and simulation techniques of annealing have been remarkably improved in the last two decades with the ultimate goal of providing quantitative tools for analysis and prediction of annealing behaviour (e.g. [7-12, 124, 125]). Application of computer simulation to recrystallization and grain growth was strongly stimulated by the work which has been done by Anderson et. al. [7] which showed that the Monte Carlo technique may be used for simulation of grain growth. The model was later modified by Srolovitz et. al [8, 9] for simulation of recrystallization.

Monte Carlo methods (or Monte Carlo experiments) are a class of computational algorithms that rely on repeated random sampling to compute the final results. In Monte Carlo techniques which have been developed for simulating annealing phenomena, a continuum microstructure is mapped into a lattice [7-9]. Each lattice site is assigned a number,  $S_i$  as shown in Figure 2-6. Lattice sites which are adjacent to sites having different grain orientations are regarded as being separated by a grain boundary, while a site surrounded by sites with the same orientation is inside the grain. Microstructural properties inside each lattice site are assumed to be homogeneous, while microstructural inhomogeneities may be assigned to the microstructure through considering different properties in different lattice sites. Each lattice site contributes an assigned level of energy, i.e.  $H_i$  to the system; in recrystallization modelling, the level of energy is the energy stored during deformation in the

form of dislocation at site  $i$ . In addition to deformation stored energy, each unlike pair of nearest neighbours contributes a unit of grain boundary free energy,  $\gamma$ . Therefore the total energy of the system,  $E$ , is calculated through the following Hamiltonian equation [7-9]:

$$E = \sum_{i=1}^N H_i + \frac{1}{2} \sum_{i=1}^N \sum_{j=1}^{N_n} \gamma(1 - \delta_{i,j}) \quad (2-26)$$

Where the sum on  $i$  is over all lattice sites of the system, i.e.  $N$ , sum of  $J$  is over the nearest neighbour of site  $i$  and  $\delta$  is the Kronecker delta:

$$\delta_{i,j} = \begin{cases} 1, & \text{if } i = j \\ 0, & \text{if } i \neq j \end{cases} \quad (2-27)$$

The evolution of structure is simulated by selecting a site in a random manner and examining the possibility of reorientation of its nearest neighbour to the selected site. Reorientation is accepted if the assigned criterion of the simulation is satisfied [7-9].

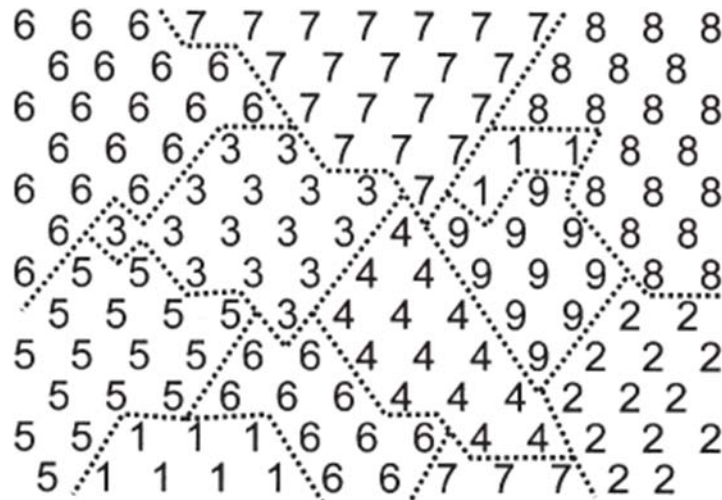
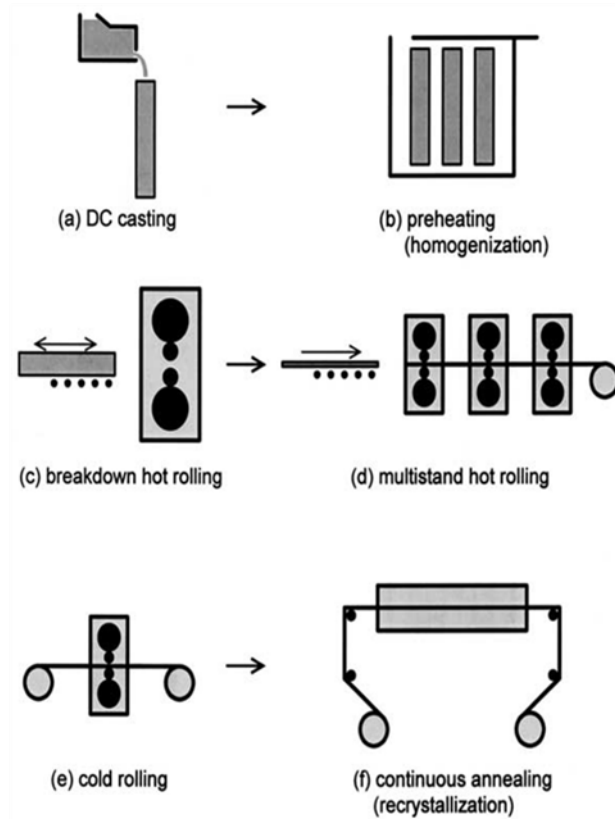


Figure 2-6. Schematic representation of a mapped microstructure for Monte Carlo simulation [3].

There have been many attempts in developing new Monte Carlo algorithms for including various microstructural properties which affect the progress of annealing (e.g. [10, 12, 124, 125]). The effect of stored energy distribution on microstructural evolution has been included in the technique by considering hypothetical stored energy gradients [12, 124, 125] as well as use of EBSD results as the input of the model for pure alloys [11]. In addition the effect of particles [12, 125] and concurrent recovery [10, 12, 125] on progress of recrystallization has been simulated. Although important progress has been made in providing Monte Carlo simulation techniques for various annealing conditions, to the best of the author's knowledge, there is no available simulation technique which considers interactions of precipitation, recovery and recrystallization in simulating microstructural evolution during annealing.

#### **2.2.4. Annealing of AA6xxx aluminum alloy**

In the commercial production of AA6xxx sheets, the alloy undergoes a specific thermomechanical processing as schematically demonstrated in Figure 2-7. During this process, initially the billet obtained through direct chill casting is hot rolled where its thickness is reduced from about 600mm to 3-6mm in a multi-stand mill. Subsequently, the thickness of the hot rolled plate is reduced to the final gauge of around 0.8-1.2mm through cold rolling. The last stage includes annealing of the cold-rolled sheet [4, 99]. Final properties of the sheet strongly depend on all of the process steps.



**Figure 2-7. Schematic representation of typical thermomechanical processing steps in commercial production of AA6xxx aluminum alloy sheets [4].**

Commercial AA6xxx aluminum alloys have complex microstructures consisting of different types of second phase particles. The second phase particles can be classified in three major groups:

- Large Fe rich constituents that form during solidification [4, 97-99];
- Al(Fe,Mn)Si dispersoids that form during homogenization and hot rolling [4, 97-99];
- Precipitates, which form during aging heat treatment, [2, 18, 19, 97].

Dispersoids and constituents are always present during cold deformation, while precipitates may or may not be, depending on the TMP route. Therefore, the deformation zones forming around constituents and dispersoids during cold working may influence

annealing behaviour of the alloy through the PSN effect. The extent of such an effect depends on the particle and precipitate size and distribution as well as the level of deformation. Initiation of recrystallization at large constituents and dispersoids has been widely reported (e.g. [2, 92, 97, 99]). It has been shown that at moderate levels of deformation (40% and 60% reduction in thickness), the volume fraction of recrystallized grains in AA6013 alloy strongly depends on the size and distribution of constituents. However, such dependency is lost after a high level of cold rolling reduction, i.e. 80% [98]. The effectiveness of the constituents for acting as preferred nucleation sites in AA6xxx alloys has also been reported to be strongly affected by the presence of precipitates [2]. Lillywhite et. al. [2], showed that in the presence of fine precipitates, recrystallization nucleation through PSN is restricted to those coarse particles that are surrounded by precipitate free zones.

While annealing behaviour of AA6xxx alloys in the presence of precipitates has been extensively studied (e.g. [96, 104, 106, 107, 111]), relatively few studies [2, 6, 87, 124] have been performed on studying the systems where the precipitates can nucleate, coarsen, dissolve and transform during annealing. Lillywhite et al. [2] have studied the influence of prior precipitation states on recrystallization behaviour of an Al-Mg-Si alloy. In their work, different heat treatments have been applied prior to rolling, to produce samples with various precipitate conditions. The results show a dramatic effect of the starting condition on recrystallization behaviour of the alloy. It is shown that depending on the starting condition (before rolling), the rate of recrystallization can be controlled by (a) PSN for highly overaged condition, (b) local coarsening of  $\beta$  for the overaged condition, and (c) solute drag effect and phase transformation of  $\beta'$  to  $\beta$  for the as-quenched condition [2].

The same approach as Lillywhite et al. [2] has been taken by Wang et al. [92] and Go and colleagues [6, 126] to study the interaction of precipitation and recrystallization in AA6111 aluminum alloy. In these works, the recovery and recrystallization behaviour of samples with four different starting conditions (naturally-aged, peak aged, overaged and severely overaged) prior to deformation (40% reduction) have been studied. It has been suggested that in all conditions the onset of recrystallization is mostly controlled by precipitate coarsening, and the overaged condition has been reported as having the longest recrystallization time. Recrystallization in the overaged sample has been retarded due to the strong pinning effect of the small fractured  $Q$  phase precipitates. It is implied that although the fractured precipitates coarsen by further annealing, due to their high number density, they pin grain boundaries and retard recrystallization. No fracture of the square-shaped  $\beta$  phase precipitates, which have been formed through severe overaging, has been reported. Although these plate-shaped precipitates have been present during deformation, no PSN on them is reported either [6, 92, 126]. The incapability of square-shaped precipitates in serving as PSN sites is in agreement with Troeger et al's [104] results.

### **2.3. Grain refinement in AA6xxx**

Application of AA6xxx aluminum alloys in automotive skin panels results in significant weight reduction and is considered as one of the most practical solutions to the growing demand for production of lightweight fuel-efficient vehicles [99]. Currently such an application is restricted to high-end car models or simple-shaped panels due to the high cost of aluminum and the limited formability of the AA6xxx. Formability issues may be overcome by applying a combination of warm forming techniques and grain refinement of AA6xxx aluminum sheets [127, 128]. Grain refinement of AA6xxx aluminum sheets has been the

subject of many researches (e.g. [46, 91, 104, 129]). One of the most common methods for grain refinement in aluminum alloys is thermomechanical processing (TMP). Thermomechanical processes are described as any combination of thermal and deformation processing. Both the type and order of each processing stage, i.e. heat treatment and deformation, influence the final result. Considering the deformation techniques, TMP routes can be divided into two main categories: (a) methods based on severe plastic deformation (SPD) through novel deformation techniques such as ECAP (e.g. [46, 91, 130]) and (b) the methods based on conventional deformation techniques such as rolling (e.g. [104, 106, 107]). However, due to limitation, SPD techniques have only produced relatively small quantities of materials. Considering that conventional deformation methods are more cost efficient compared to SPD, there is a strong interest in developing TMP routes for production of fine grained AA6xxx aluminum sheets through conventional deformation techniques followed by proper heat treatments.

Conventional rolling methods have been used for the production of fine-grained structures (i.e. average grain diameter 10-20  $\mu\text{m}$ ) in heat treatable aluminum alloys. The approaches for grain refinement of precipitation hardenable aluminum alloys through TMP, using rolling as the deformation method, have been first patented by Waldman [107] and Paton and Hamilton [106]. As a brief summary, the procedure in their work includes solution heat treatment, overaging, cold rolling, and subsequent annealing. Large rolling reduction in the presence of overaged precipitates results in PSN during recrystallization and, as a result, grain refinement of the alloy. Although Waldman [107] and Paton [106] successfully conducted grain refinement on AA7xxx aluminum alloys through conventional rolling, the attempts for grain refinement of AA6xxx aluminum alloys through the same procedure were not successful

[129]. The problem arises as the overaged precipitates of AA6xxx alloy cannot act as preferred nucleation sites for recrystallization due to their plate-shaped morphology [6, 104], and as a result a fine-grained structure could not be produced.

Considering this problem, another TMP has been developed by Troeger et al. [104]. In the latter method, a rolling process is added after solutionizing and prior to aging. Through this method, first the material is given a solution heat treatment followed by a water quench. Then the material is cold-rolled and, subsequently, overaged. In the next step, the overaged material is subjected to another cold rolling stage followed by annealing. During annealing, a fine-grained structure with an average grain diameter of 10 $\mu$ m is formed through recrystallization of new grains mainly on PSN sites. PSN sites are provided by spheroidized overaged precipitates. Adding another deformation stage prior to overaging results in the formation of spherical overaged precipitates, instead of the regular plate-shaped one. Although, the process was successful in grain refinement of AA6xxx alloys, it has not been adapted for the production of automotive sheets.

More recently, a new thermomechanical processing method (designated as TMPM, hereafter) has been developed for grain refinement of AA6xxx aluminum sheets [1, 131]. In contrast to previously developed method [104] for grain refinement of AA6xxx, which are designed based on PSN effects of overaged precipitates, TMPM has been designed considering the interaction of concurrent precipitation (i.e. precipitate nucleation, growth and coarsening) and annealing phenomena. Eliminating the overaging and extra deformation stage makes this technique more cost effective and practical from industrial point of view. In summary TMPM includes three steps: a solutionizing step, followed by a cold rolling stage and a non-isothermal annealing process starting from low temperatures. These stages are compatible with existing

commercial production lines due to the continuous nature of the process. TPM has been implemented on AA6451 and a fine-grained sheet with significantly enhanced ductility at warm forming temperatures and a very weak texture [1, 131] has been achieved.

## Chapter 3. SCOPE AND OBJECTIVE

The present work aims to fulfill the following two main objectives:

- providing a comprehensive knowledge on the underlying mechanisms of microstructural evolution in an AA6451 aluminum alloy during the implementation of a recently-developed non-isothermal annealing process,
- developing a physically based computational modeling technique for the simulation of microstructural evolution during non-isothermal annealing of precipitation hardenable AA6xxx alloys.

These objectives are achieved through:

- characterization of the cold-rolled state which governs the subsequent annealing phenomena,
- investigating interactions between precipitation, recovery and recrystallization processes that dictate microstructural evolution during non-isothermal annealing;
- developing a new physically based computational modeling technique through a combination of the acquired knowledge and existing physical theories;
- implementing the developed model for simulation of microstructural evolution during isothermal and non-isothermal annealing;
- validating the simulation results with experimental results.

The computational modeling technique will be the first approach for simulating microstructural evolution in precipitate hardenable AA6xxx aluminum alloys. The combined experimental and modeling work makes a significant contribution to better understanding the annealing behaviour of AA6xxx aluminum alloys. The results have the potential to be used in the design and optimization of thermomechanical routes, to develop tailored microstructural properties in precipitate hardenable aluminum alloys.

## Chapter 4. EXPERIMENTAL METHODOLOGY

This chapter includes information on the material as well as the heat treatment procedure and describes the experimental techniques which have been performed in this investigation to characterize non-isothermal annealing behaviour of the alloy.

### 4.1. Material

The aluminum alloy AA6451 used in this study was provided by Novelis Global Technology Center (NGTC) in the form of hot rolled plate of ~5mm thickness and a solutionized, naturally aged, and cold-rolled sheet of ~1mm thickness. The 1mm thick sheet was produced in accordance with the Thermomechanical processing method (TMPM) proposed by Esmaeili et. al [1, 131] for grain refinement of AA6xxx aluminum alloys. The sequence of producing the 1mm sheet from the 5mm hot-rolled plate is schematically demonstrated in Figure 4-1. The chemical composition of the alloy is given in Table 4-2.

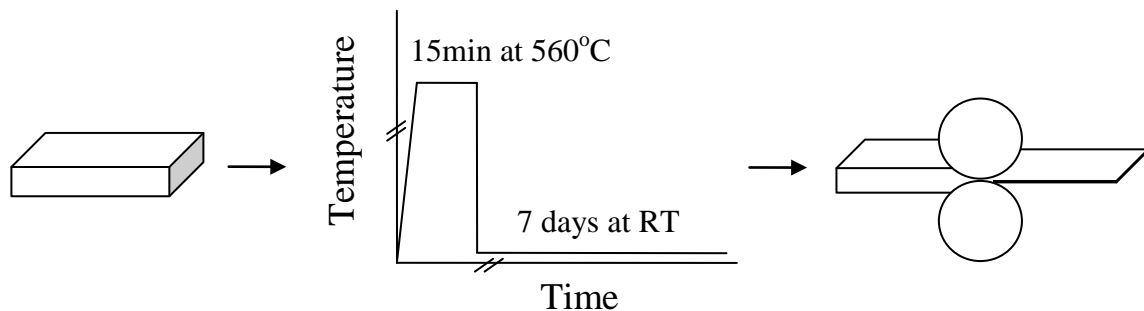


**Figure 4-1. Schematic diagram of the processing route for production of cold-rolled sheet from hot-rolled plate: a) hot-rolled 5mm thick plate, b) solutionizing and natural aging of the hot-rolled plate, and c) thickness reduction from 5mm to 1mm through multiple cold rolling passes.**

**Table 4-1 Chemical composition of AA6451 alloy (wt%)**

Alloy	Mg	Si	Cu	Fe	Mn	Cr	Ti
AA6451	0.64	0.77	0.31	0.26	0.23	0.001	0.024

## 4.2. Thermomechanical processing

The 5mm AA6451 plate was solutionized for 15min at 560°C and, subsequently was water quenched to produce as-quenched, i.e. AQ, plates. As-quenched cold-rolled sheets, i.e. AQ-CR, were produced by reducing the thickness of the AQ plate to ~1mm. Cold rolling was performed immediately after quenching to avoid natural aging prior to deformation. In addition to the AQ-CR sheet, samples at naturally aged condition, i.e. NA, were produced by storing the AQ 5mm thick plate at room temperature for one week.

The cold-rolled sheets were thermally processed for producing microstructural states associated with the early, intermediate and final stages of the TPM [1, 131]. Thermal processing included non-isothermal annealing of the cold-rolled sheet from 50°C to various annealing temperatures up to 380°C at a heating rate of 0.4°C/min in an air atmosphere furnace. The samples which were annealed to 380°C were held at 380°C for 20min and then furnace cooled. Annealed samples were given a simple three-term, i.e. X-X-X, identification code. The first two terms indicate the deformation and its prior heat treatment history, and the third term indicates the temperature that the sample was annealed to. The annealing treatment route for preparing samples for further characterization is schematically illustrated in Figure 4-2. The sample identification is summarized in Table 4-2.

In addition to AA6451, ultra pure aluminum (99.999%) was used in this study. The ultra pure aluminum was received in the form of a cast billet with a thickness of 3cm. The

billet was, initially, hot rolled to 5mm thickness and, subsequently, cold rolled to 1mm thickness to produce a cold-rolled ultra-pure aluminum sheet, i.e. Al-CR.

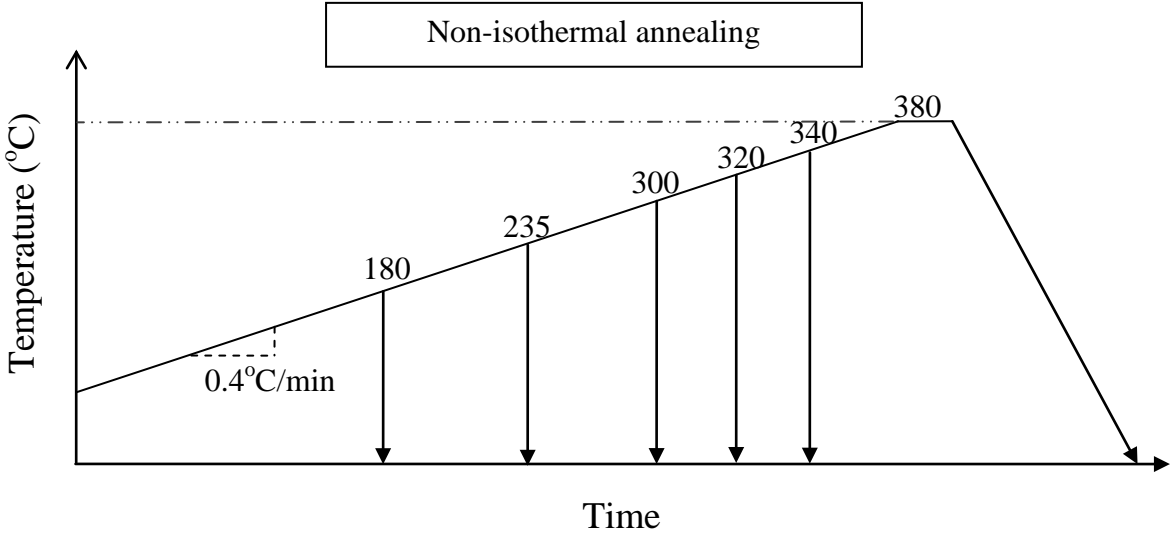


Figure 4-2. Schematic presentation of the non-isothermal annealing routes.

**Table 4-2. Sample identification**

Designation	Material	Process Route	Test
Al-CR	pure Al	Hot-rolled + Cold Rolling (80% reduction in thickness)	DSC
AQ	AA6451	15 min at 560°C + water quenched	DSC
NA	AA6451	15 min at 560°C + water quenching + 1 week at room temperature	DSC
AQ-CR	AA6451	AQ + Cold Rolling (80% reduction in thickness)	DSC
NA-CR	AA6451	NA + Cold Rolling (80% reduction in thickness)	DSC, TEM
NA-CR-180	AA6451	NA-CR + heating from 50°C to 180°C (0.4°C/min) + water quenching	TEM, EBSD
NA-CR-235	AA6451	NA-CR + heating from 50°C to 235°C (0.4°C/min) + water quenching	TEM, EBSD, SEM
NA-CR-300	AA6451	NA-CR + heating from 50°C to 300°C (0.4°C/min) + water quenching	TEM, EBSD, SEM
NA-CR-320	AA6451	NA-CR + heating from 50°C to 320°C (0.4°C/min) + water quenching	EBSD, SEM
NA-CR-340	AA6451	NA-CR + heating from 50°C to 340°C (0.4°C/min) + water quenching	TEM, EBSD
NA-CR-380-20m	AA6451	NA-CR + heating from 50°C to 380°C (0.4°C/min) + 20 min at 380°C + furnace cooling	TEM, EBSD, SEM

### **4.3. Experimental methodology**

In the following sections, the characterization procedures which were employed in this research are introduced. The experimental procedures are categorized according to the testing techniques which were used.

#### **4.3.1. Differential scanning calorimetry (DSC)**

DSC tests were carried out in a SETARAM C80 calorimeter in an air atmosphere and using the same heating rate as the non-isothermal annealing, i.e.  $0.4^{\circ}\text{C}/\text{min}$  (up to  $300^{\circ}\text{C}$ ). For each test, multiple sample pieces,  $10\text{ mm} \times 5\text{ mm} \times 1\text{ mm}$  in size (total mass  $\sim 850\text{ mg}$ ), were placed in the test vessel while the reference vessel was kept empty. The baseline trace was acquired by running a similar test on a pure Al sample (same mass as the alloy sample). The corrected final DSC trace was obtained by subtracting the baseline trace from the trace acquired for the alloy sample. The exothermic reactions were plotted upward and endothermic reactions downward on the DSC thermograms. DSC tests were repeated at least three times to confirm repeatability of the results.

#### **4.3.2. Microhardness measurement**

Samples for microhardness measurements were heated to various annealing temperatures in the range of  $50^{\circ}\text{C}$  to  $380^{\circ}\text{C}$ , with the same heating rate as the DSC test (i.e.  $0.4^{\circ}\text{C}/\text{min}$ ) and with  $10^{\circ}\text{C}$ - $25^{\circ}\text{C}$  intervals. The heat treated samples, then, were cold mounted in an acrylic resin and polished to  $1\mu\text{m}$  finish. Microhardness measurements were conducted using a Leco micro-hardness tester and applying a  $200\text{g}$  load for 20 seconds. Each reported hardness value is the average of seven readings. The variation between reported average values

and the multiple measurements for each condition have found to lie between  $\pm 4\%$  of the average value.

### **4.3.3. Transmission electron microscopy (TEM)**

TEM analyses were performed on samples with selected heat treatment conditions as listed in Table 4-2. Additional investigations were performed on samples which were held for 20 minutes at the end annealing temperature. These samples were designated by a “20m” suffix at the end of the identifying code. Table 4-3 summarizes heat treatment conditions of the additional TEM samples. TEM analysis on the samples with a 20 minute hold time was performed to study mechanisms of the interactions between precipitate and dislocations/grain boundaries. The effect of the 20min holding time on the nature of these mechanisms is expected to be negligible.

The TEM foils of the heat treated samples were prepared by the conventional method through mechanical polishing up to a thickness of 80-100 $\mu\text{m}$ , punching samples from the sheet and twin jet polishing. Jet polishing was performed in 30% nitric acid in 70% methanol solution, with the polishing condition of 15 volts in the temperature range of  $-30^{\circ}\text{C}$  to  $-40^{\circ}\text{C}$ . The thin foils were examined either in a Philips electron microscope operated at 120 KV at NGTC or in a Philips CM-12 electron microscope operated at 120 KV at McMaster University. To analyse the interaction of precipitates and dislocations, a combination of dark field and bright field imaging was used. Dark field imaging helps in identifying fine precipitates, while the bright field technique reveals dislocations with a better contrast. Dark field analysis was performed on the  $[001]_{\text{Al}}$  zone axis. TEM observations were conducted with the assistance of Mr. Don Steele at NGTC and Dr. Xiang Wang at McMaster University.

**Table 4-3. Identification of the additional TEM samples**

Designation	Process Route
NA-CR-180-20m	NA-CR + heating from 50 °C to 180 °C (0.4 °C/min) + 20 min at 180 °C + water quenching
NA-CR-235-20m	NA-CR + heating from 50 °C to 235 °C (0.4 °C/min) + 20 min at 235 °C + water quenching
NA-CR-340-20m	NA-CR + heating from 50 °C to 340 °C (0.4 °C/min) + 20 min at 340 °C + water quenching

#### 4.3.4. Scanning electron microscopy (SEM)

The distribution of large/coarsened precipitate and grain structure was studied by scanning electron microscopy through a combination of secondary and backscattered imaging techniques. Secondary electrons offer a high resolution and are suitable for studying precipitates. On the other hand, they do not reveal grains. Appropriate electrons for this purpose are the backscattered ones, as they are able to show orientation contrast. In order to obtain the best quality backscattered electron images, the voltage was set between 5-6 kV, the working distance was kept as low as 6mm, a large aperture (either 60 or 120 $\mu$ m) was used, the contrast was increased to maximum, and the brightness adjusted to its lowest level. SEM micrographs were taken using a LEO 1530 FEGSEM microscope.

Surface preparation of the samples for backscattered SEM analysis is critical, as the orientation contrast is weak and often difficult to detect. Therefore, the influence of surface imperfections must be minimal. To prepare ideal samples for SEM analysis, after mechanical grinding, samples were polished with diamond paste up to 0.25 $\mu$ m. To remove the thin deformation layer which forms at the surface of the sample during mechanical grinding and polishing, the mechanically polished samples were electropolished. Electropolishing was

performed in a solution of 30% Nitric acid and 70% Methanol kept below  $-30^{\circ}\text{C}$ . The samples were electropolished for 45 seconds at a voltage of 9V.

#### **4.3.5. Electron backscatter diffraction (EBSD)**

EBSD tests were performed at NGTC by Dr. H. Jin, using a Philips XL30S field emission gun (FEG) scanning electron microscope (SEM), equipped with a Nordlys II detector, and operated at 25kV. To maximize backscattered electrons, samples were tilted by  $70^{\circ}$  and working distance was kept at 14mm. For EBSD analysis, the heat treated samples were mechanically ground and polished, and then electropolished in a solution comprising 2% butylcellosolve, 8%  $\text{HClO}_4$ , 30% alcohol and 60% water with current density of  $1.5 \text{ A/cm}^2$  for 30 seconds at  $-10^{\circ}\text{C}$ .

EBSD mapping of the grain structure was carried out at step sizes of  $0.25 \mu\text{m}$ ,  $1 \mu\text{m}$  and  $2 \mu\text{m}$ . Each test was run on a region about  $1.5\text{mm} \times 1\text{mm}$  of the samples in the rolling plane (RD-TD plane). EBSD analysis was based on the acquisition of kikuchi diffraction patterns from bulk sample in the scanning electron microscope. The HKL channel 5 software was used to control the data acquisition, solve the diffraction pattern and store the data. Stored data were further analyzed by the software to provide orientation maps, grain boundary maps, average grain size, as well as the quantitative representation of indexing quality. For grain structure reconstruction by HKL Channel 5 software,  $7.5^{\circ}$  was considered as the threshold angle. It should be mentioned that an optimum value for the threshold angle to identify the boundary structure of an EBSD map may lie in the range of  $5\text{-}20^{\circ}$  [131]. It has been found that  $7.5^{\circ}$  serves as an optimum misorientation angle for the analysis of the data obtained from the EBSD tests of commercially-processed AA6xxx alloys, and provides results

in agreement with the results from optical and scanning electron microscopy techniques [133].

In the EBSD maps, different orientation appears with different colors.

## Chapter 5. EXPERIMENTAL RESULTS AND DISCUSSION

### 5.1. Results

In this section, the experimental results are presented by following the sequence of the experimental procedure described in Chapter 4.

#### 5.1.1. Characterization of precipitation behaviour through DSC

Differential scanning calorimetry (DSC) technique has been employed to study the precipitation state after natural aging, as well as the precipitate evolution during non-isothermal annealing. The results of DSC analysis on naturally-aged and as-quenched samples in the deformed and non-deformed conditions are presented in this section.

In order to study the precipitation sequence in AA6451 and to reveal precipitation events that occur during natural aging, DSC runs have been conducted on the as-quenched and naturally-aged material, i.e. AQ and NA, respectively. The corresponding DSC thermograms are shown in Figure 5-1. The distinct heat effects of the thermograms are marked by letters. Following the information given in the literature on similar alloys [18, 19], the exothermic peaks A and B may be linked to the formation of clusters and GP zones. Similarly, peaks C and C' with a shoulder marked as C<sub>a</sub> and C<sub>a</sub>' and peaks D and D' may be considered as representing the precipitation of  $\beta''$ , Q'',  $\beta'$  and Q' phases [18, 19]. No attempt is made to pinpoint the exact association of each peak with named precipitates and the degree of overlap between precipitation events. It should be mentioned that the shoulder peak C<sub>a</sub> has usually been observed when DSC tests are run at low heating rates [51, 133, 135, 136]. Comparison of the thermograms for the naturally-aged material with that of the as-quenched sample shows a remarkable reduction in the cluster peak (i.e. A compared to A').

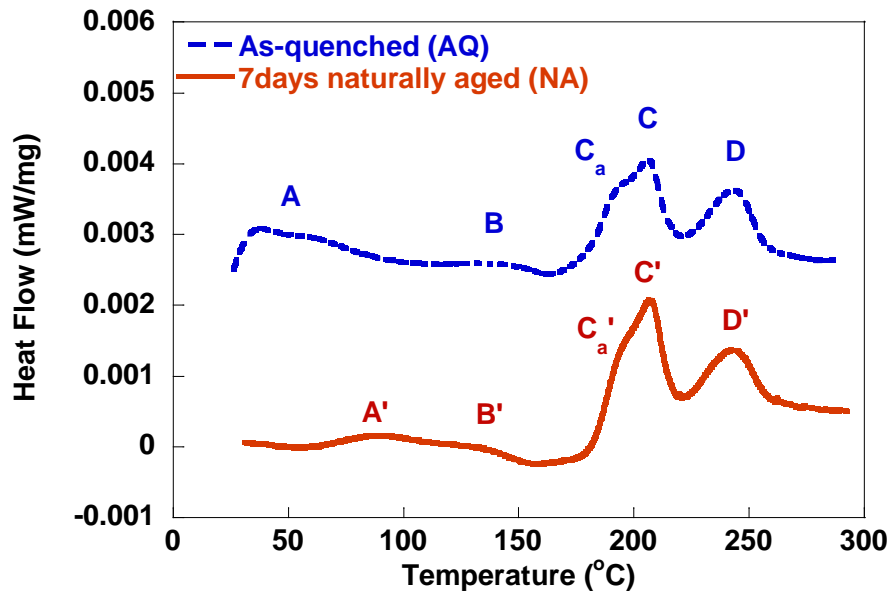


Figure 5-1. The DSC thermograms for the as-quenched (AQ) and naturally-aged (NA) samples.

The effect of prior natural aging on the precipitation behaviour during annealing of cold-rolled AA6451 has been studied by performing DSC runs on the cold-rolled samples with and without prior natural aging, i.e. AQ-CR and NA-CR, respectively. DSC thermograms for these conditions are shown in Figure 5-2. For comparison, the DSC curve of the cold-rolled pure aluminum, i.e. Al-CR, is also plotted in the same figure. In the DCS thermograms of both AQ-CR and NA-CR conditions, two exothermic peaks are observed. No noticeable heat effect is observed on the DSC trace of the Al-CR sample.

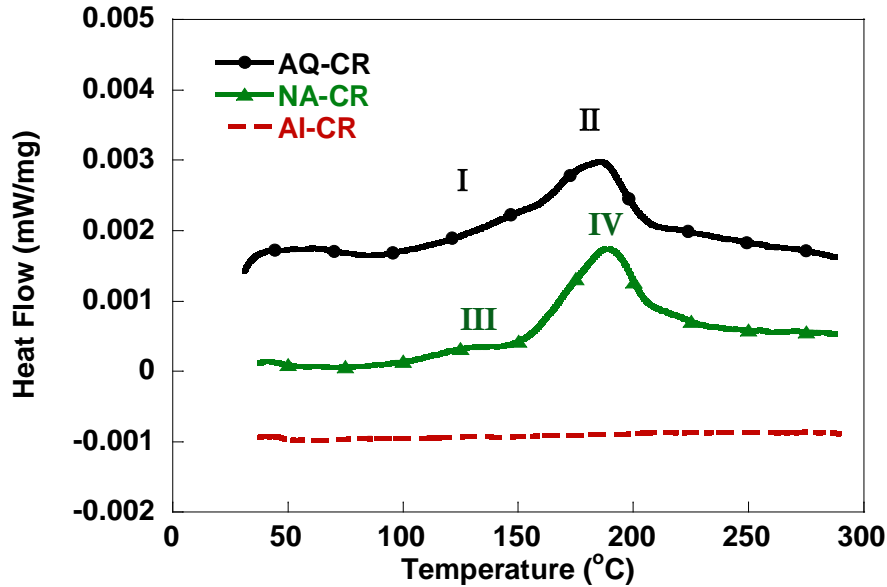


Figure 5-2. The DSC thermograms for the as-quenched and cold-rolled (AQ-CR), and naturally-aged and cold-rolled (NA-CR), and cold-rolled pure aluminum (Al-CR) samples.

## 5.2. Characterization of precipitate hardening and annealing softening

The results of hardness measurements on NA, NA-CR, AQ-CR and Al-CR samples annealed to various temperatures are presented in this section. These results help to follow precipitation hardening and annealing softening during non-isothermal annealing.

Variation of hardness with temperature during non-isothermal aging/annealing for NA and NA-CR conditions are shown in Figure 5-3. The results of the tests on the NA sample provide information on the precipitation hardening behaviour of the naturally-aged sample with no deformation. The hardness of the NA sample slightly increases when heating from 50°C to 180°C. A remarkable increase in hardness is observed up to 230°C, where hardness reaches its maximum value of 131 HV; annealing beyond 230°C results in a sharp decrease of hardness. Hardness evolution in the NA-CR sample represents the overlapping effects of precipitation hardening and annealing softening. Initially, the hardness of the NA-CR sample increases with annealing temperatures up to 180°C, where peak of hardness, i.e. 155 HV, is

achieved. The continuation of annealing to higher temperatures results in the reduction of hardness. At the annealing temperature of 300°C, a sudden change in the slope of hardness reduction is observed; hardness falls with a larger slope until a plateau appears at the end of the plot between 340°C and 360°C.

The effect of natural aging prior to the deformation on softening behaviour has been studied through measuring hardness evolution in the AQ-CR sample. Compared to the NA-CR sample, the initial value of the hardness is lower for the AQ-CR sample. However, the amount of hardness increase from 50°C to 180°C is larger for AQ-CR. Both NA-CR and AQ-CR conditions follow a similar trend for the decrease of hardness above 180°C. For comparison, hardness evolution for cold-rolled pure aluminum is also provided in Figure 5-3. No remarkable hardness change is observed for the AI-CR sample up to about 150°C, where hardness starts to decrease gradually up to 300°C and is followed by a plateau above 300°C.

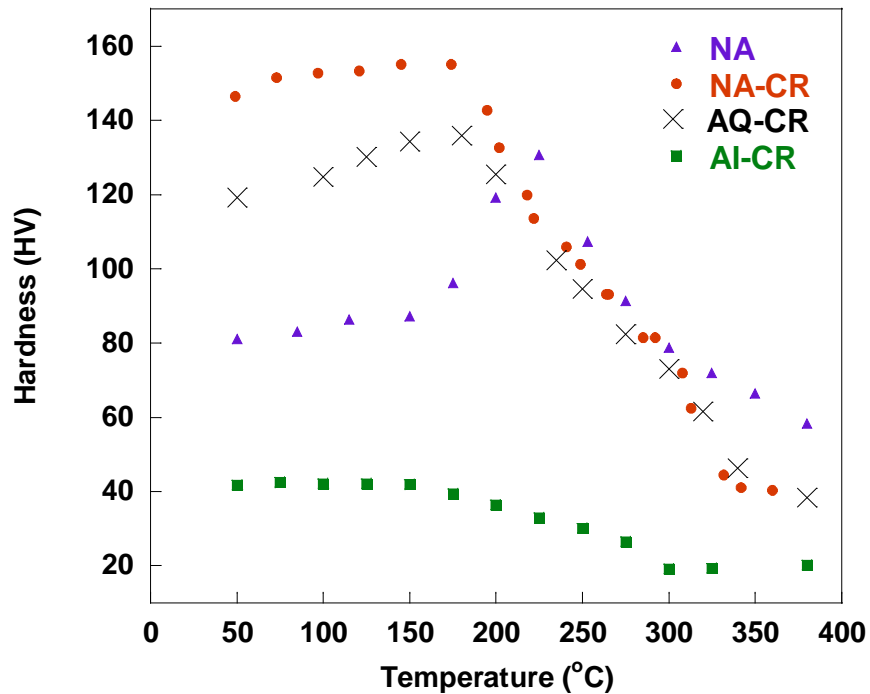


Figure 5-3. Microhardness evolution of naturally-aged (NA), naturally-aged and cold-rolled (NA-CR), as-quenched and cold-rolled (AQ-CR), and cold-rolled pure aluminum (AI-CR) samples.

### 5.2.1. Microstructural characterization through TEM

The objective of the TEM experiments has been to gain insight into the microstructural changes during annealing, and particularly, dislocations and precipitate distributions, their mutual interactions, and their effects on the progress of recovery and recrystallization. The results of TEM investigations on the as-deformed (NA-CR) sample and on naturally-aged and cold-rolled samples, which have been non-isothermally annealed to various temperatures, are presented in this section.

#### TEM analysis on the as-deformed sample

TEM studies on the as-deformed NA-CR sample have revealed a uniform distribution of dislocations with no trace of dislocation cell formation, as shown in Figure 5-4. No precipitates have been detected through bright or dark field TEM analysis on this sample.

#### TEM studies on the samples annealed to 180°C

Dislocation distribution after annealing to 180°C has been investigated on the NA-CR-180 sample. As shown in Figure 5-5, dislocations seem to have a uniform distribution with no specific arrangement. The TEM investigations performed at various magnifications and tilt conditions on different parts of the samples have not revealed dislocation cell or subgrain formation at this annealing stage. Precipitate distribution after annealing to 180°C has been studied by analysing the NA-CR-180-20m sample as shown in Figure 5-6. Although even at high magnifications, precipitates are not clearly visible in the bright field image (Figure 5-6 (a)), the dark field image (Figure 5-6 (b)) shows the presence of very small precipitates which are located along the perpendicular  $\langle 100 \rangle$  directions of the matrix. The bright field image clearly shows dislocations, while the dark field image highlights the small precipitates in

bright contrast. The comparison of these two micrographs shows that the apparent density of precipitates on dislocations is higher than the rest of the microstructure. At this annealing condition, the precipitates are too small to be identified by EDX analysis or through their morphology.

#### TEM analysis on the samples annealed to 235°C

Figure 5-7 shows the dislocation distribution in the NA-CR-235 sample. Compared to NA-CR and NA-CR-180, a minor rearrangement of dislocations is observed for this sample. Examining the microstructure of NA-CR-235 at higher magnifications than that of Figure 5-7 reveals formation of small dislocation-free regions. Figure 5-8 provides evidence for the presence of these regions surrounded by sharp boundaries. The dislocation-free regions are indicated by arrows in Figure 5-8 (a). The same area has been examined more closely at different tilting angles as shown in Figure 5-8(b) and Figure 5-8(c), in order to identify whether the surrounding boundaries are high angle or low angle. High angle grain boundaries (HAGB) do not disappear when the sample is tilted, while the low angle grain boundaries (LAGB) disappear by tilting. Figure 5-8 shows that as the sample has been tilted, boundaries that surround the dislocation-free regions in marked area A have disappeared. Therefore, it is implied that the disappearing boundaries are LAGB, and, consequently, the observed regions are considered as subgrains. Additional TEM studies have shown that subgrains form at various areas of the sample with no specific preferred location, including regions well inside the deformed grains, close to grain boundaries and adjacent to large particles. Figure 5-9 shows subgrains that have formed close to a large particle. The EDX spectrum of the particle which is provided in the same figure identifies it as an Al(Fe, Mn, Cu)Si particle.

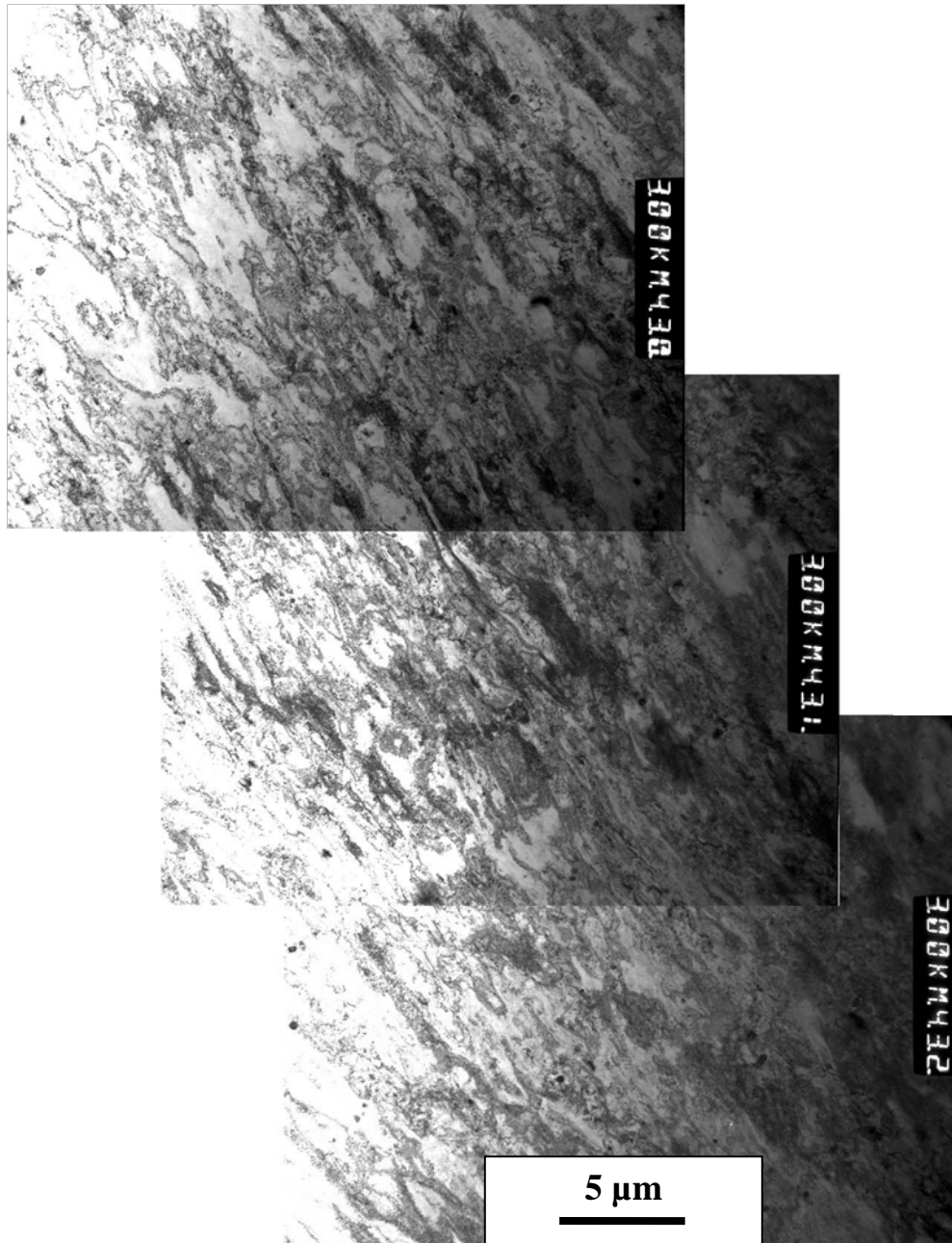


**Figure 5-4. Bright field TEM micrograph showing dislocation distribution in the as-deformed (NA-CR) sample (TEM operated by X. Wang).**

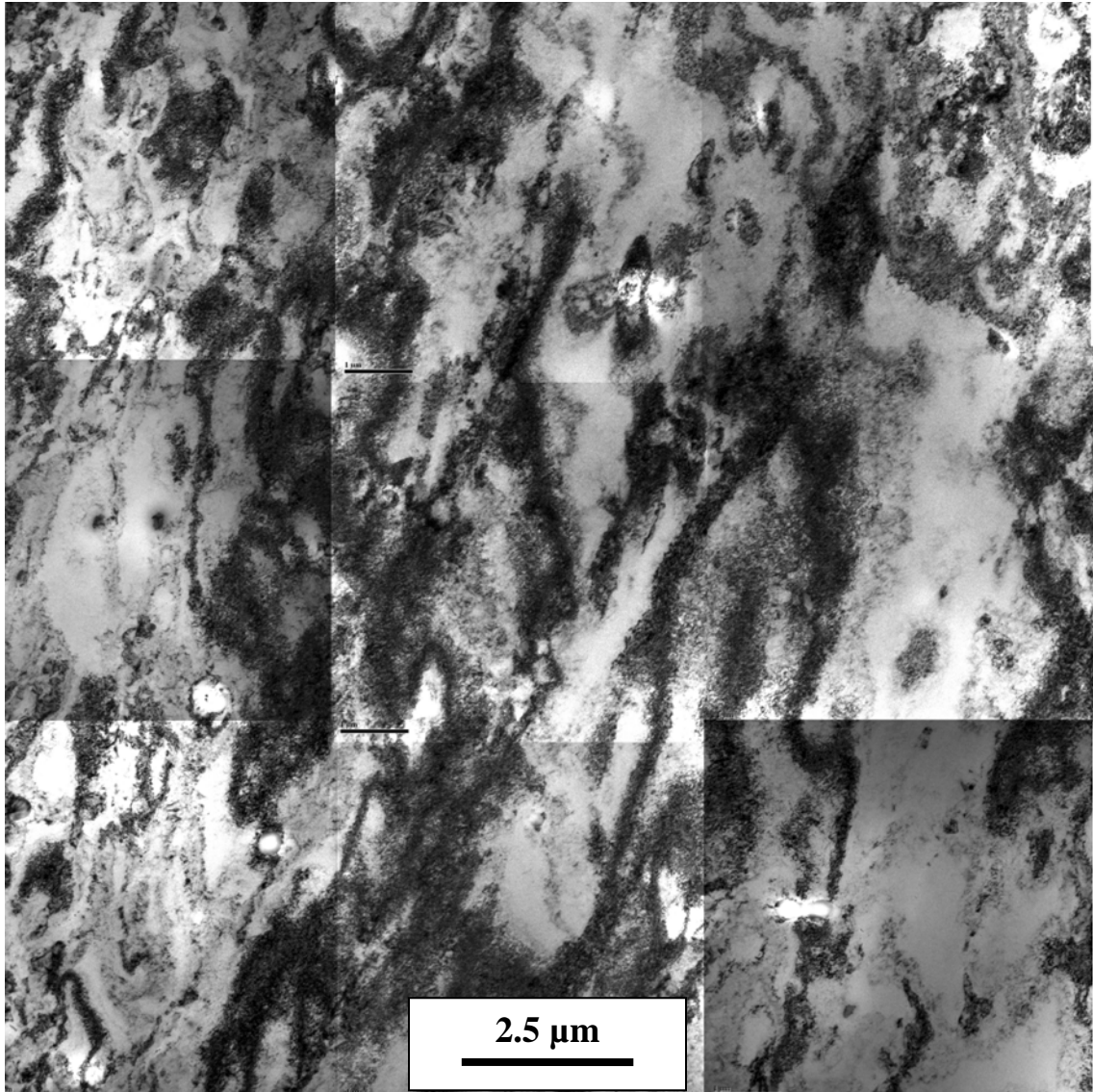


**Figure 5-5. Bright field TEM micrograph showing dislocation distribution in the NA-CR-180 sample (TEM operated by X. Wang).**

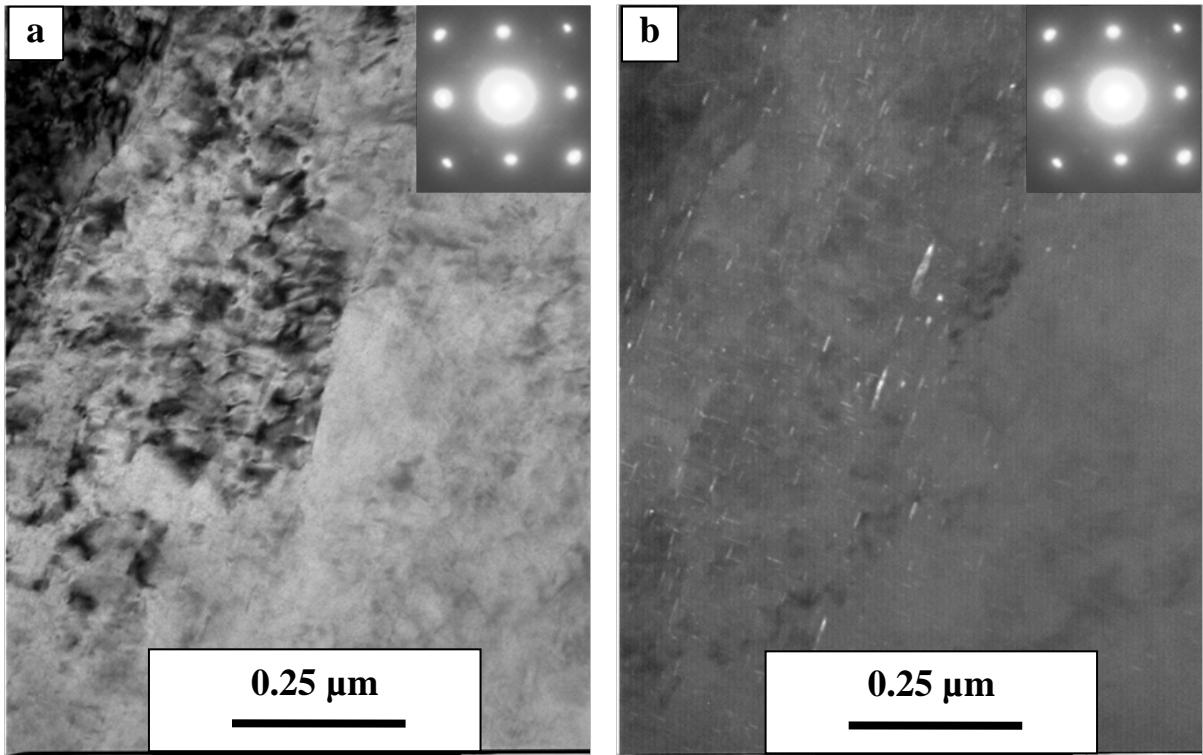


Figure 5-6. TEM micrographs of NA-CR-180-20m a) bright field image and b) dark field image taken at  $[001]_{Al}$  zone axis from an identical area of the sample (TEM operated by X. Wang).

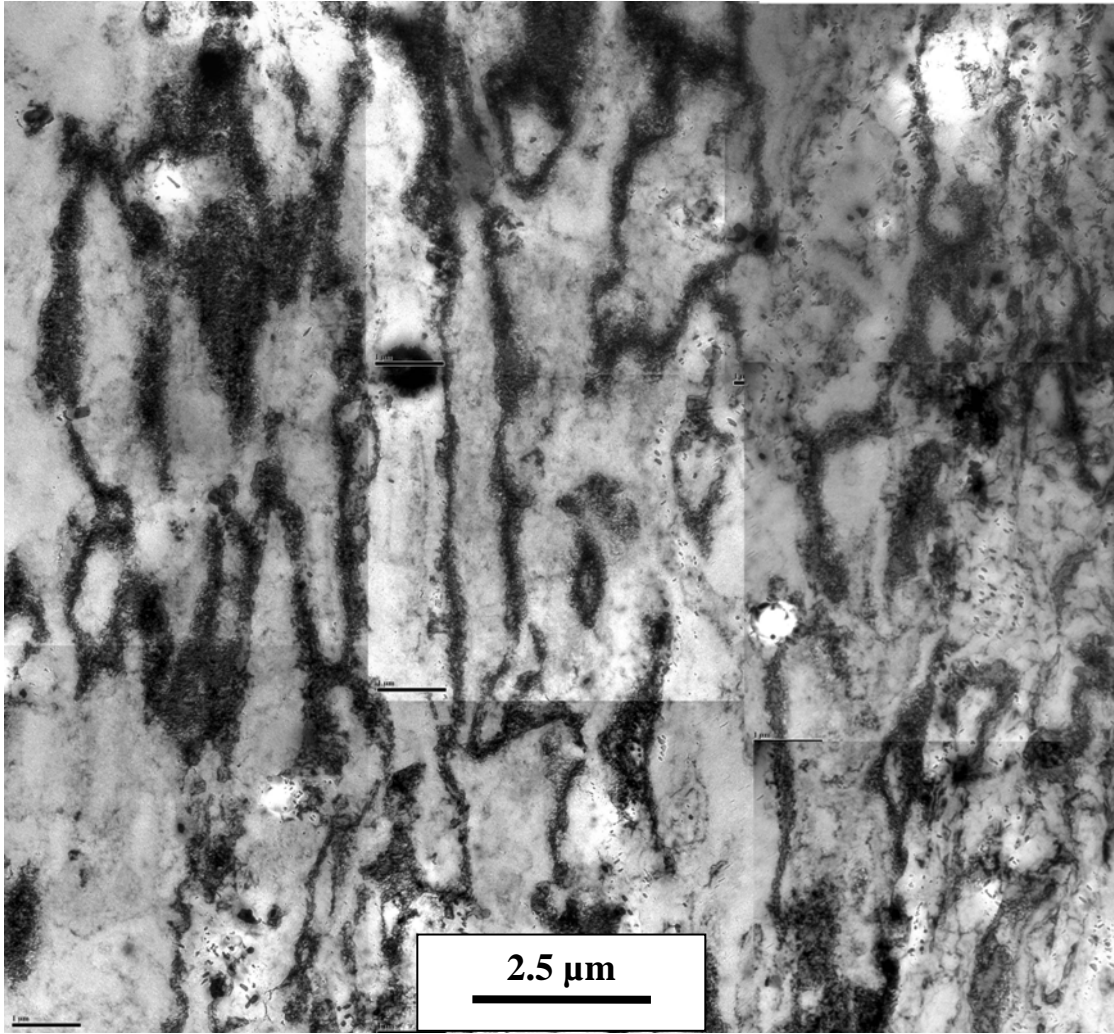
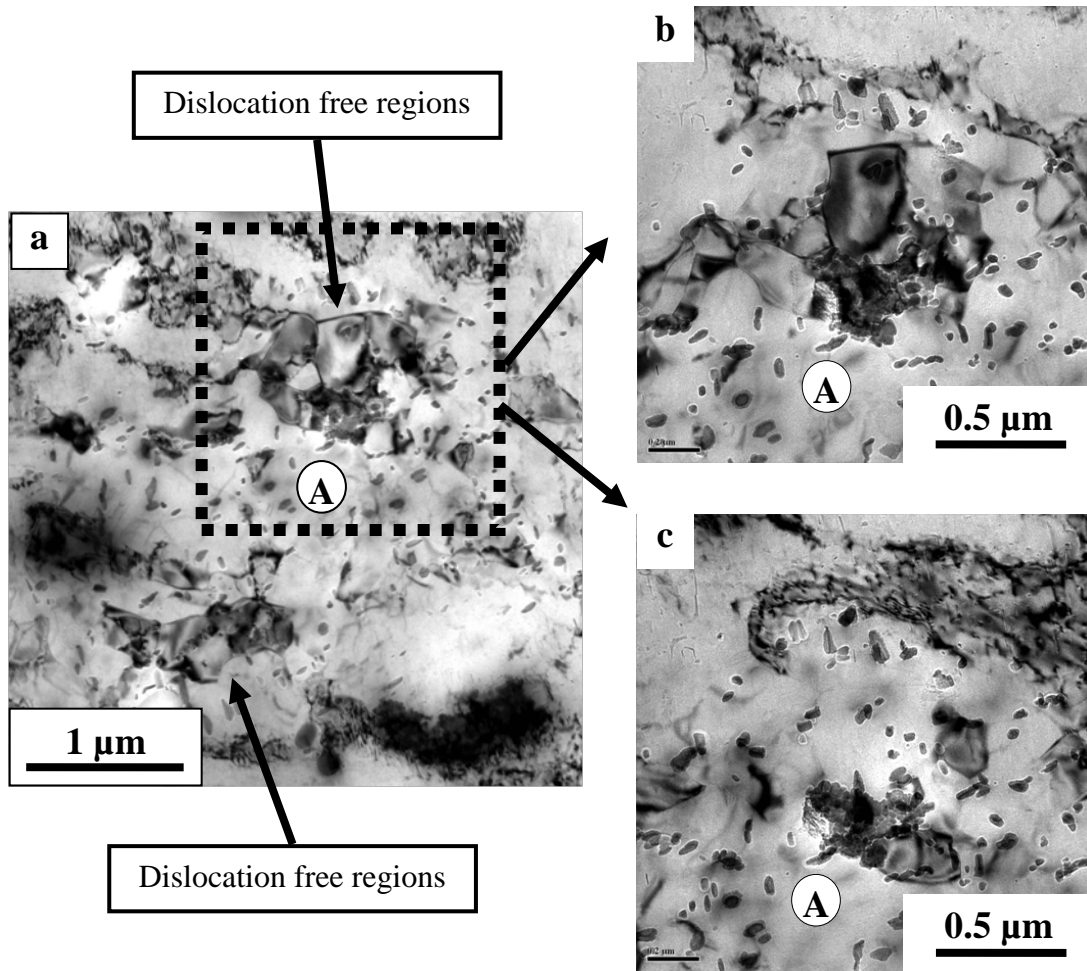
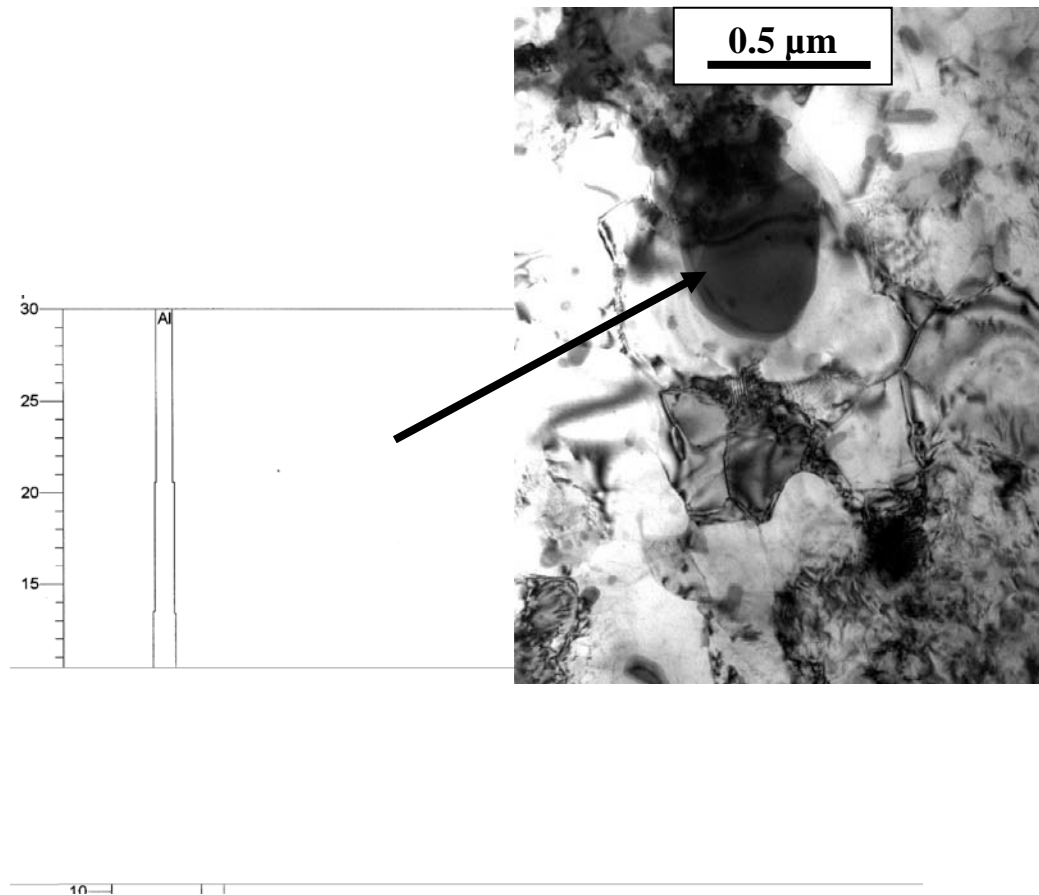


Figure 5-7. Bright field TEM micrograph showing dislocation distribution in the NA-CR-235 sample (TEM operated by X. Wang).



**Figure 5-8. TEM bright field micrograph showing presence of subgrains in the NA-CR-235 sample at different magnification and tilting conditions. For clear observation, the same area of the microstructure is marked by (A) in the micrographs (TEM operated by X. Wang).**



**Figure 5-9. TEM micrograph of the NA-CR-235-20m sample showing subgrains formed adjacent to a dispersoid particle with accompanying EDX spectrum (TEM operated by X. Wang).**

The nature of precipitates and their interactions with dislocation and grain boundaries have been investigated through TEM analysis on the NA-CR-235-20m sample at high magnifications. The TEM micrograph of this sample as presented in Figure 5-10 (a) shows the presence of precipitates with two different cross-sectional morphologies forming along  $\langle 100 \rangle$  directions of the matrix. Considering the results of a TEM analysis on a similar alloy [19] (Figure 2-2 (a) in Section 2.1.1), the precipitates with circular and rectangular cross-sectional areas are considered as pre-cursors of  $\beta$  and Q phases, respectively. These precipitates can interact with both dislocations and grain boundaries. Dislocation-precipitate interaction has

been studied through a combination of dark field and bright field TEM investigations on the NA-CR-235-20m sample. Figure 5-11 shows precipitate distribution adjacent to a wall of dislocations. Precipitates are seen in the entire micrograph with larger precipitates being located on one side of the dislocation wall. In general, compared to the NA-CR-180-20m sample, precipitates are larger in this condition. The pinning of subgrain boundaries by precipitates has also been observed for this annealing condition. A TEM image showing pinned low angle grain boundaries is presented in Figure 5-12, where pinning precipitates are pointed to by arrows.

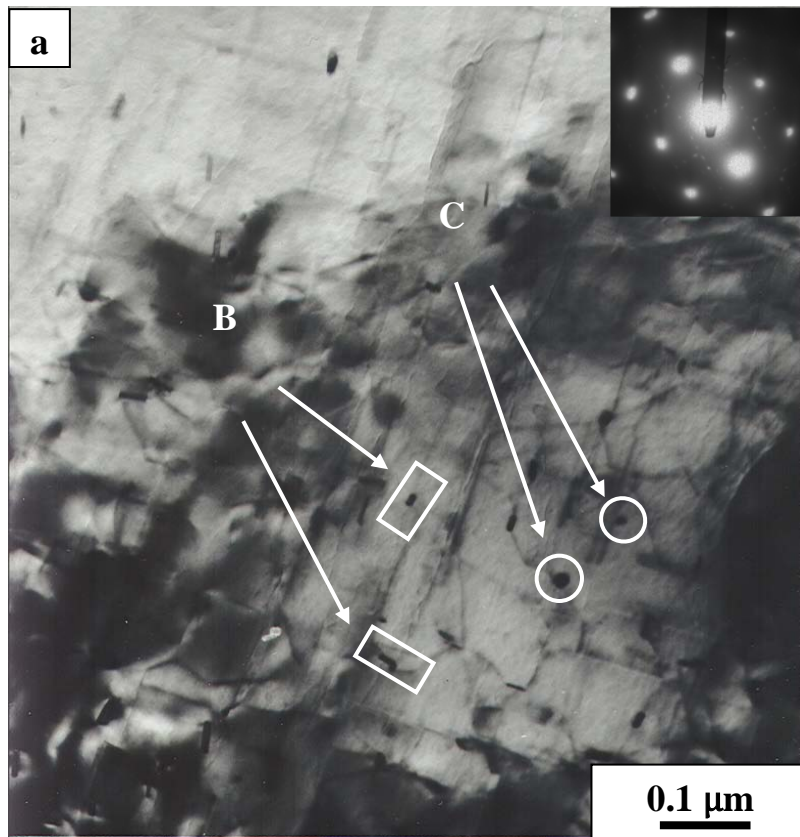


**Figure 5-10. a) TEM micrographs of NA-CR-235-20m taken at  $[001]_{Al}$  zone axis showing precipitates with rectangular cross-sectional areas (marked B) and circular cross-sectional areas (marked C) (TEM operated by D. Steele).**

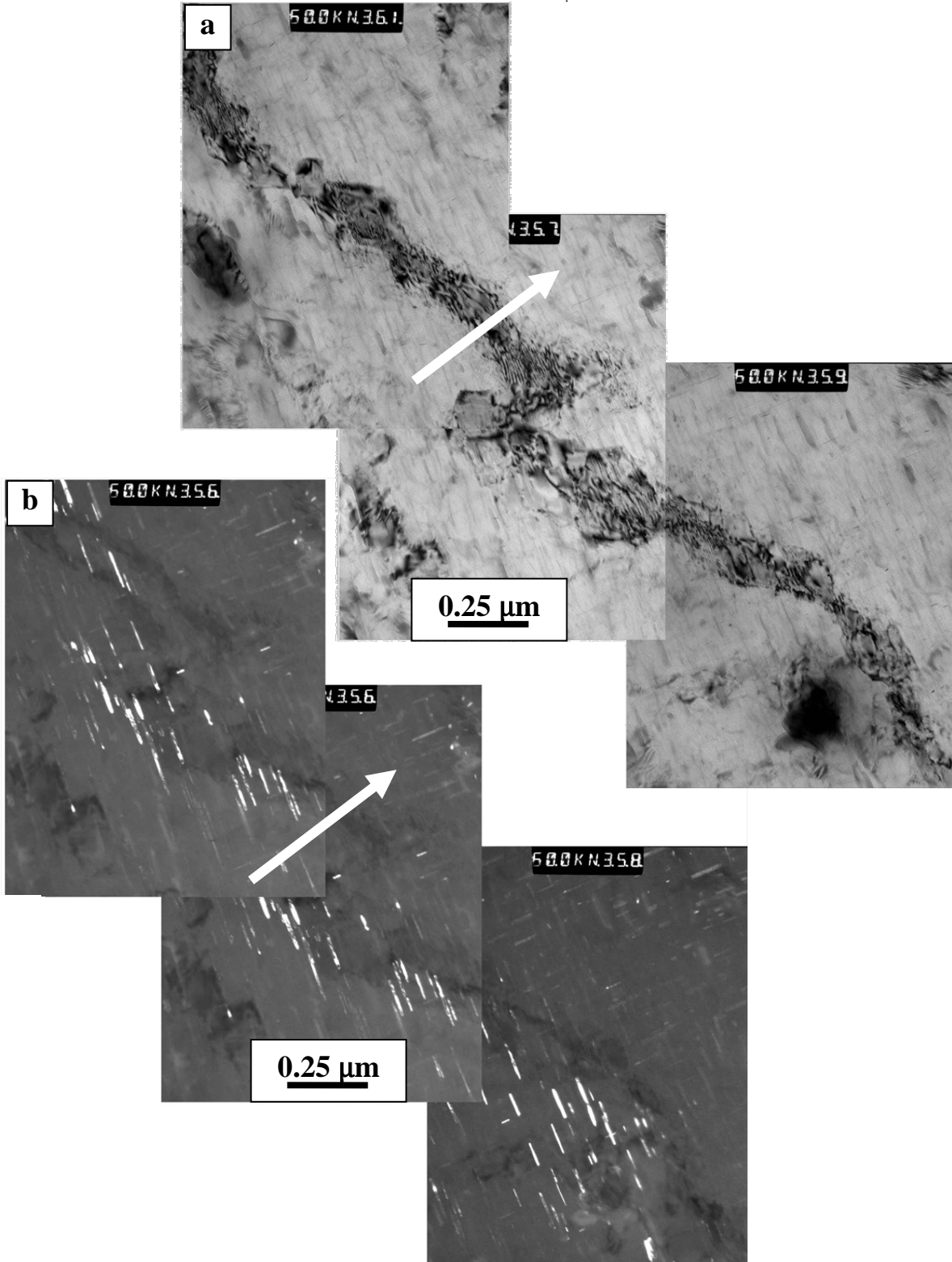
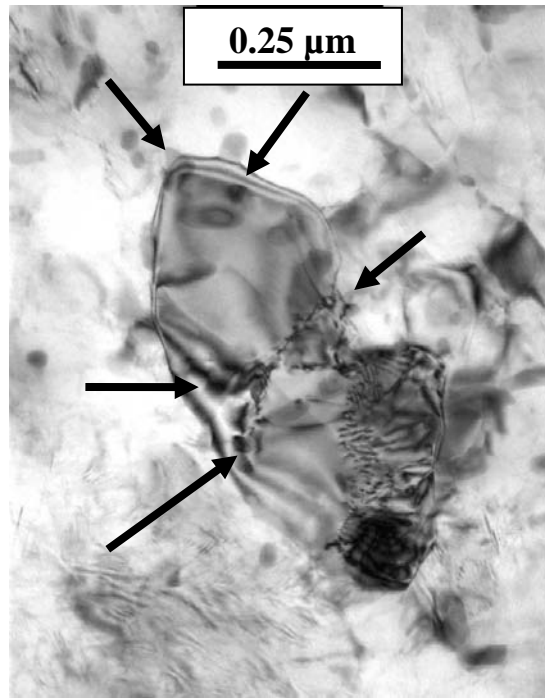


Figure 5-11. TEM micrographs of NA-CR-235-20m a) bright field image and b) dark field image (TEM operated by X. Wang).



**Figure 5-12. TEM micrograph of the NA-CR-235-20m sample showing subgrains pinned by precipitates (TEM operated by X. Wang).**

#### TEM analysis on the samples annealed to 300°C

The TEM micrograph showing dislocation distribution in the NA-CR-300 sample is presented in Figure 5-13. It is seen that by continuing annealing to 300°, part of the dislocations has been annihilated and, compared with lower annealing temperatures to which the samples have been annealed, a partially recovered structure with a lower density of dislocations has been formed. However, extended recovery, where the entire microstructure transforms to subgrains [3], has not been observed through TEM analysis on this annealing condition. On the other hand, a large number of recrystallized nuclei, as well as subgrains, have been observed in the microstructure of the NA-CR-300 sample. Recrystallized grains/nuclei have been seen to form both inside the deformed grains, with no preferential locations, and on the grain boundaries. Figure 5-14 (a) and (b) show subgrains surrounded by

LAGBs and a recrystallized nucleus partly bounded by HAGB. LAGBs and HAGBs have been identified employing different tilting angles. Figure 5-14 (c) shows the same area as Figure 5-14 (a), after tilting; similarly, Figure 5-14 (d) shows the tilted micrograph of the same area represented in Figure 5-14 (b). To make it clearer, the identical areas in Figure 5-14 (a) and (c) and in Figure 5-14 (b) and (d) are marked by letter (B) and (C), respectively. It is worth mentioning that precipitates remain unchanged by tilting. Figure 5-14 (a) and (c) show that by tilting, the dislocation free regions marked by arrows disappear. They are therefore considered as subgrains. On the other hand, the dislocation free region marked by arrows in Figure 5-14 (b) and (d) remain unchanged by tilting and, as a result, is considered as a recrystallized nucleus. In addition to nuclei (partly surrounded by HAGB) and subgrains (surrounded by LAGB), recrystallized grains have also been observed at this annealing condition. Figure 5-15 and Figure 5-16 show recrystallized grains formed on an existing grain boundary and a recrystallized grain formed inside a grain, respectively. For better observation, a dashed line is superimposed on the grain boundary in Figure 5-15. The original TEM images for this area are provided in Appendix (A1).

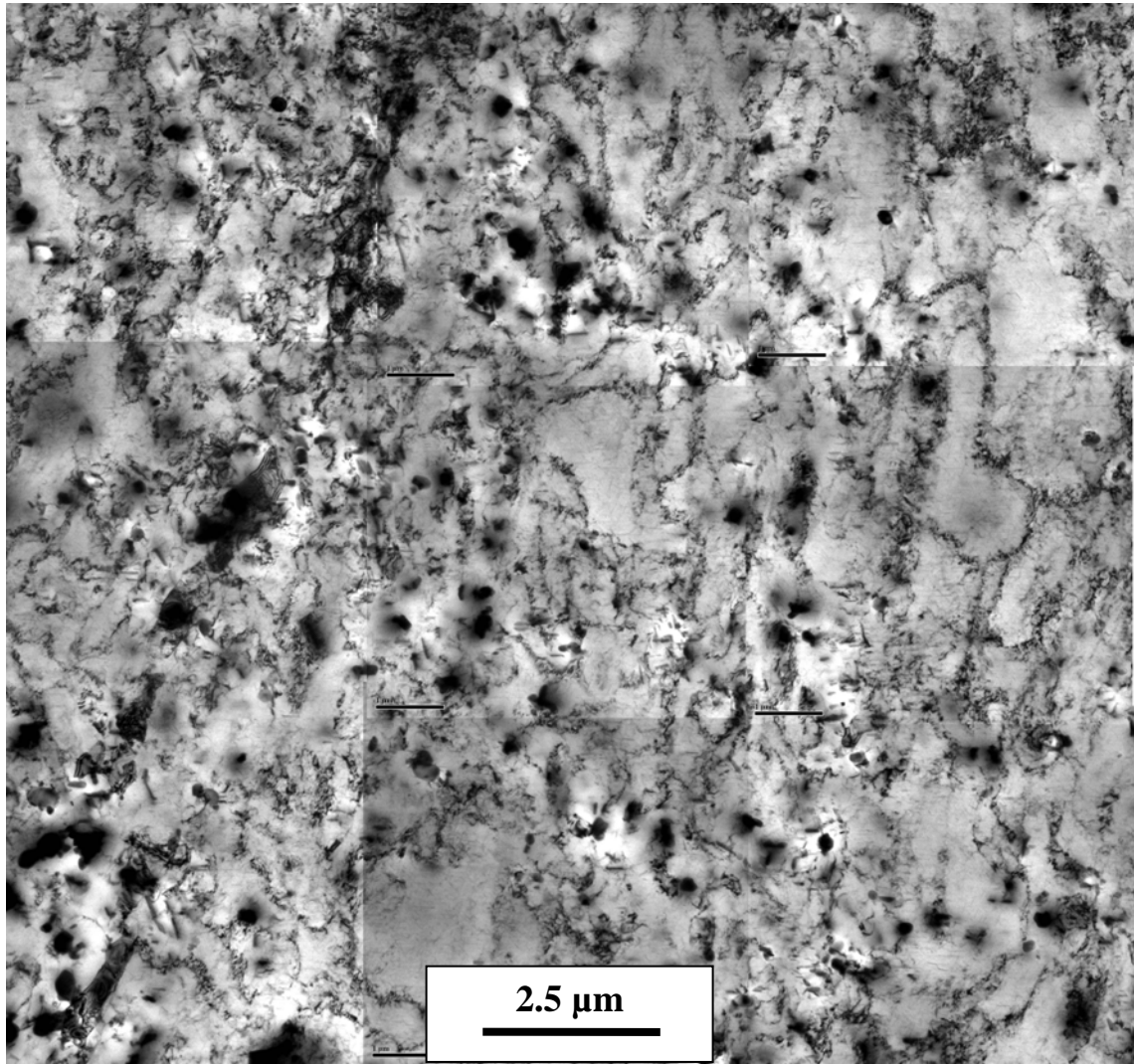
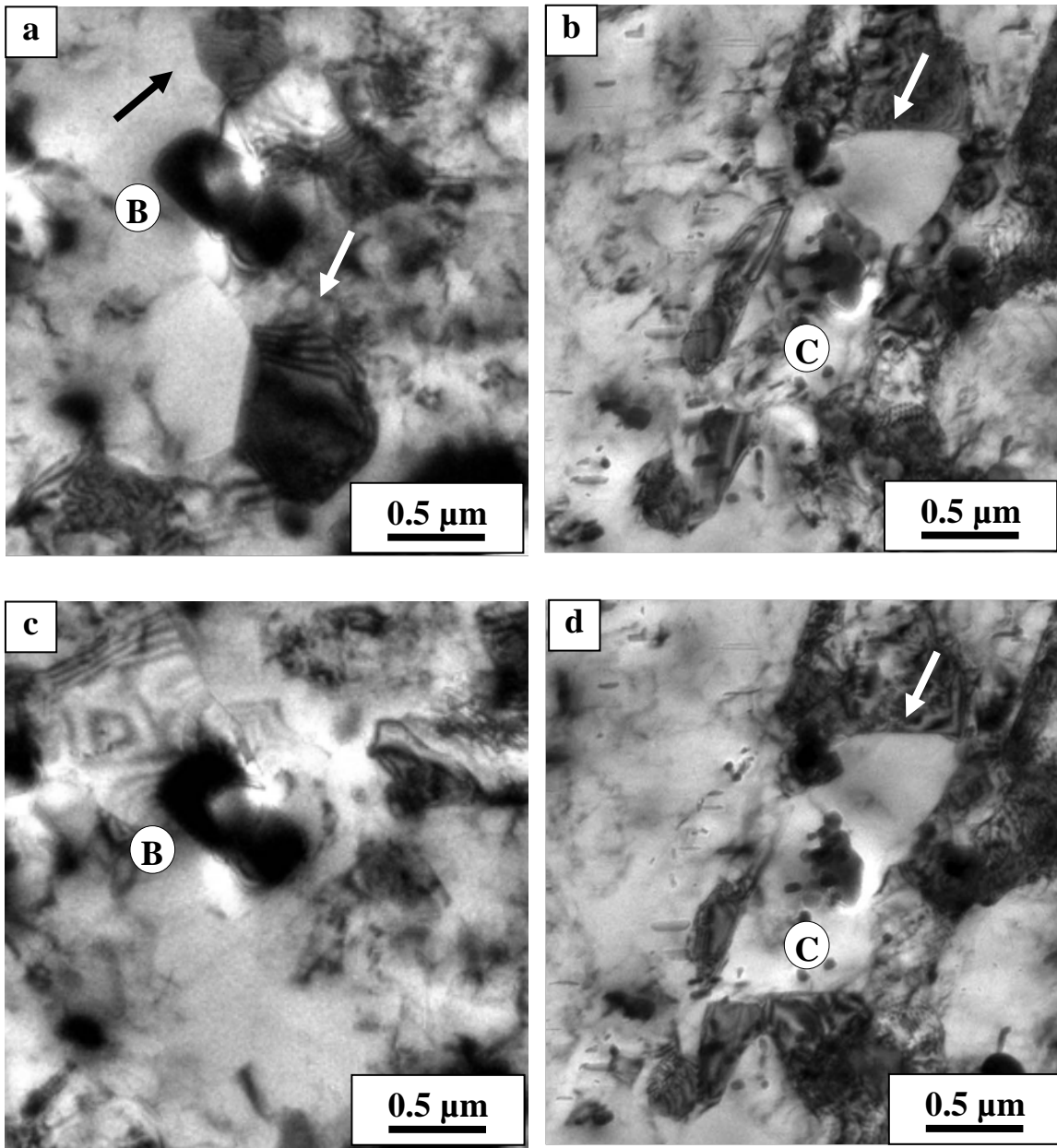


Figure 5-13. Bright field TEM micrograph showing dislocation distribution in the NA-CR-300 sample (TEM operated by X. Wang).



**Figure 5-14. TEM micrographs of the NA-CR-300 sample showing a) subgrains, marked by arrows, b) a recrystallized nucleus, marked by arrow, c) the same area presented in part a) after tilting, and d) the same area presented in part b) after tilting . The same regions of the micrographs (before and after tilting) are marked identically (TEM operated by X. Wang).**

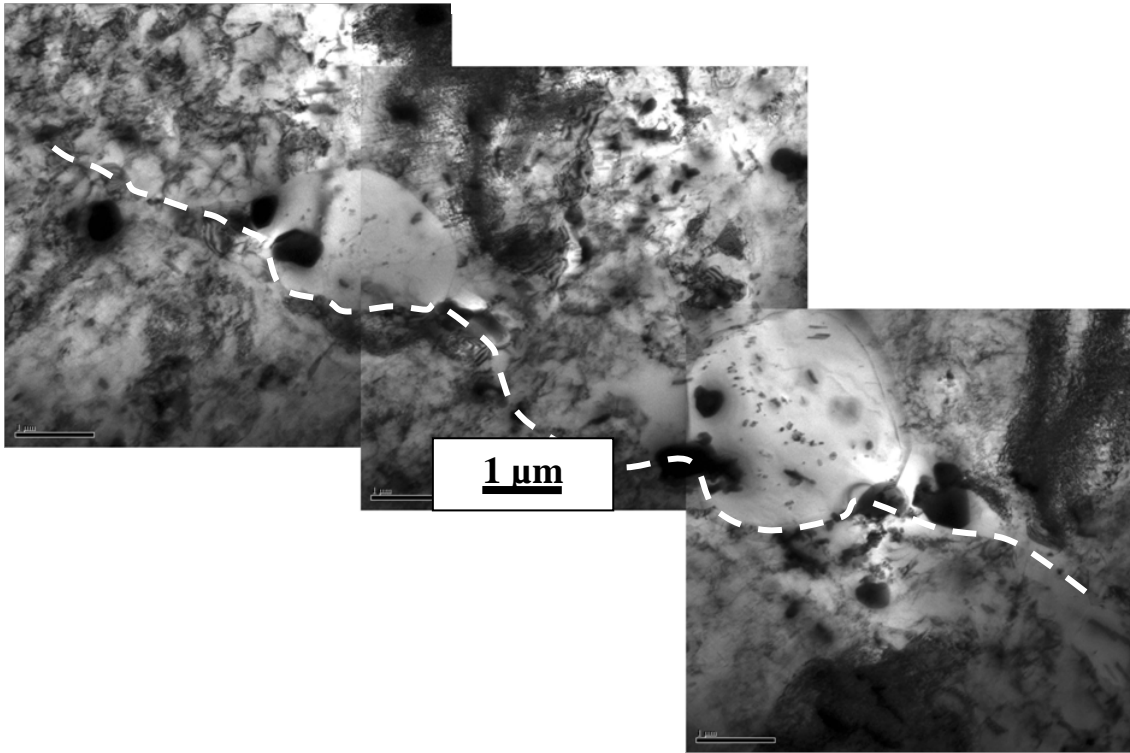


Figure 5-15. TEM bright field micrographs of the NA-CR-300 sample showing recrystallized grains on a pre-existing grain boundary (TEM operated by X. Wang).

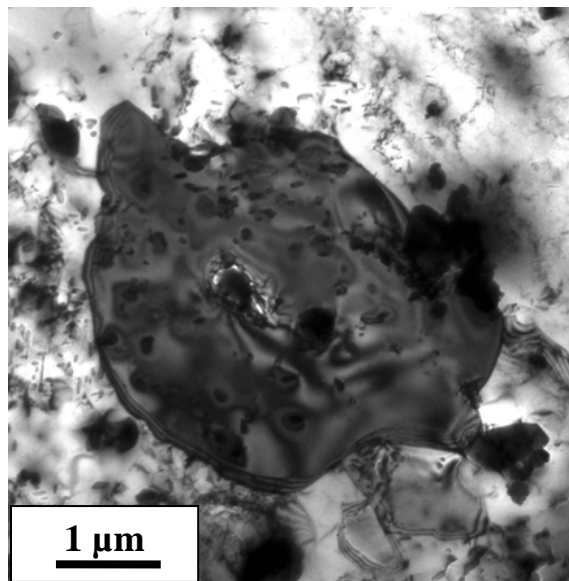
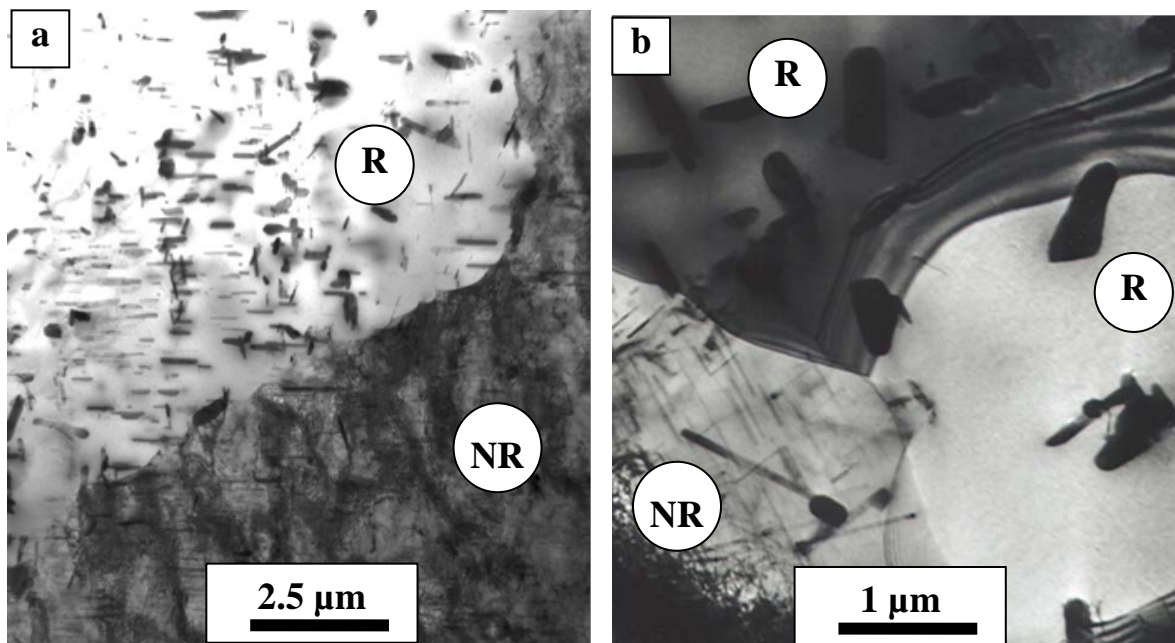


Figure 5-16. TEM bright field micrograph of the NA-CR-300 sample showing a recrystallized grain formed within the deformed structure (TEM operated by X. Wang).

### TEM analysis on the samples annealed to 340°C

The progress of recrystallization has been examined by TEM investigations on the NA-CR-340-20m sample. The TEM studies have revealed evidence for both recrystallized and non-recrystallized areas in the microstructure. However the fraction of detected non-recrystallized areas has been found to be significantly smaller than that of recrystallized areas. The two adjacent recrystallized and non-recrystallized regions are shown in Figure 5-17, and marked by (R) and (NR), respectively. Comparing R and NR areas, it is observed that precipitates located in the recrystallized regions are noticeably larger than the precipitates in non-recrystallized regions.



**Figure 5-17. TEM bright field micrographs from different areas showing recrystallized (R) and non-recrystallized (NR) regions in the NA-CR-340-20m sample (TEM operated by D. Steele).**

## TEM analysis on the samples annealed to 380°C

TEM studies on the NA-CR-380-20m sample have revealed a recrystallized structure with a large number of coarsened precipitates as shown in Figure 5-18. No non-recrystallized area has been detected in this condition.

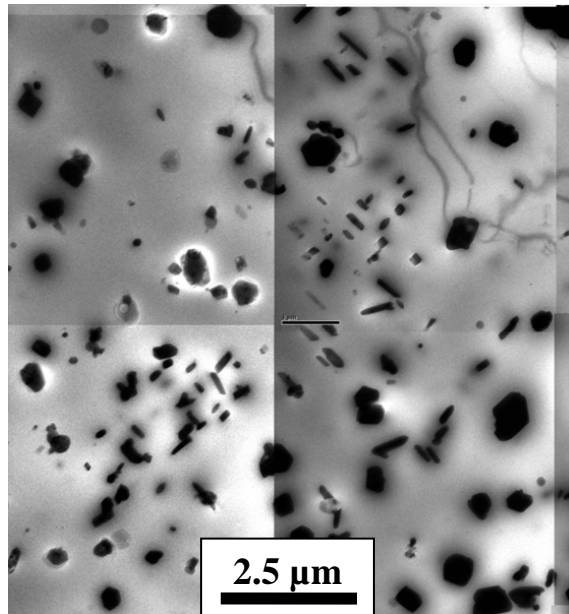


**Figure 5-18. TEM bright field micrographs showing recrystallized structure in the NA-CR-380-20m sample (TEM operated by X. Wang).**

### **5.2.2. Microstructural characterization through SEM**

SEM has been mainly employed to study overall microstructural characteristics, including: distribution of dispersoids and constituents, recrystallized grains, and large precipitates in selected annealing conditions. In this section the results of the SEM analysis are presented.

The backscattered SEM image of Figure 5-19 shows the typical distribution of dispersoid and constituent particles in the NA-CR-235 sample. As dispersoid and constituent

particles contain heavier elements than the matrix and precipitates, they appear in bright contrast in backscattered SEM images. A relatively random distribution of the particles with no preferential allocation is observed. The average diameter and area fraction of these large particles are estimated as  $1.96\mu\text{m}$  and  $0.32\%$ , respectively. These values have been used in generating the digital microstructure containing large particles for the simulation technique described in Section 6.3.

The overall distribution of recrystallized and non-recrystallized areas in the NA-CR-320 sample has been studied by SEM analysis on a large area of the sample, as shown in Figure 5-20. This figure shows a partly recrystallized structure with evidence for the formation of recrystallized bands in the structure. The recrystallized bands are marked by dashed lines. The average distance between recrystallized bands in this condition, has been estimated as  $650\mu\text{m}$ .

When the sample is completely annealed, the microstructure evolves to a uniform structure Figure 5-21. The pair of backscattered and secondary SEM images in Figure 5-21 represents the overall distribution of precipitates and grain boundaries in the NA-CR-380-20m sample. As the figure shows, at this final stage of annealing an overaged microstructure with uniformly distributed precipitates is formed. SEM observation at a higher magnification has revealed grain boundary pinning by precipitates as shown in Figure 5-22. The boundaries that are pinned are bowed in and are marked by arrows in the figure.

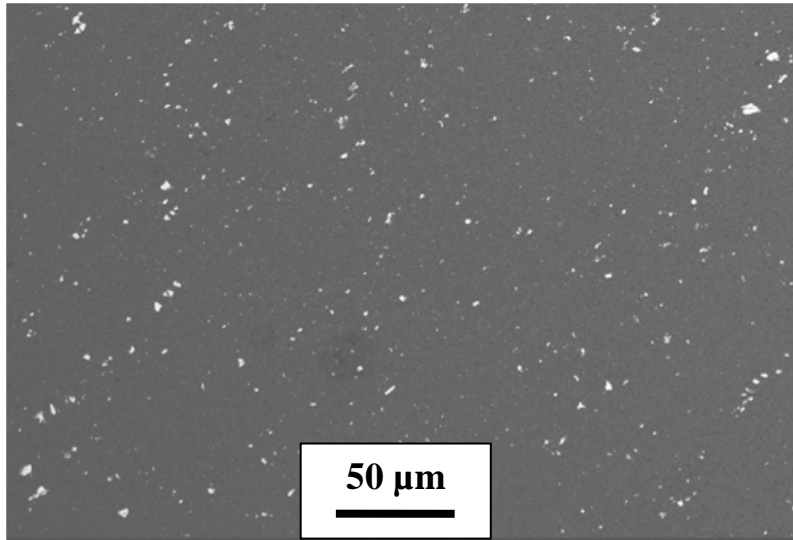


Figure 5-19. Backscattered SEM micrograph showing distribution of dispersoids and constituents in the NA-CR-235 sample.

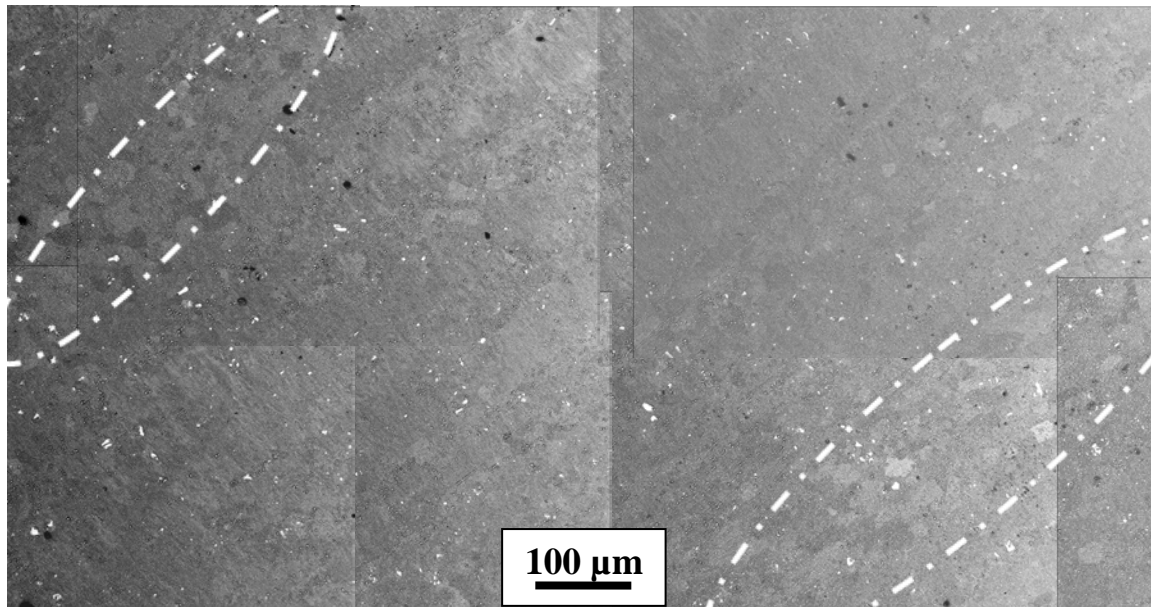


Figure 5-20. Backscattered SEM image showing recrystallized bands formed in the NA-CR-320 sample.

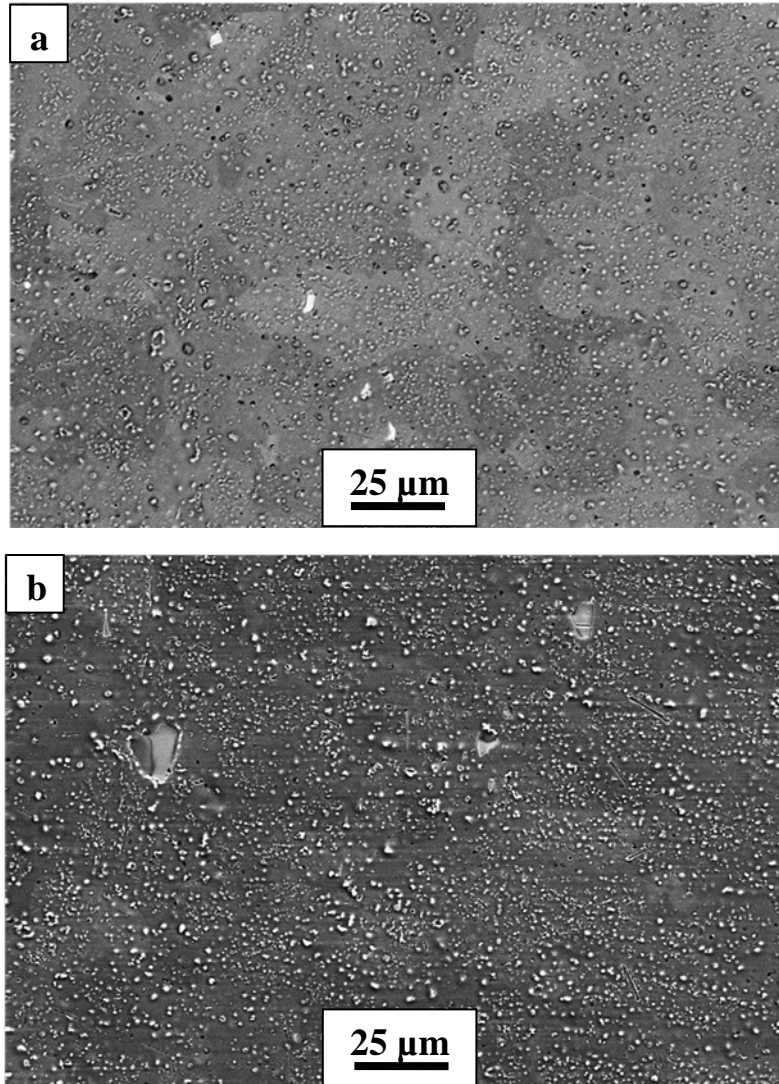
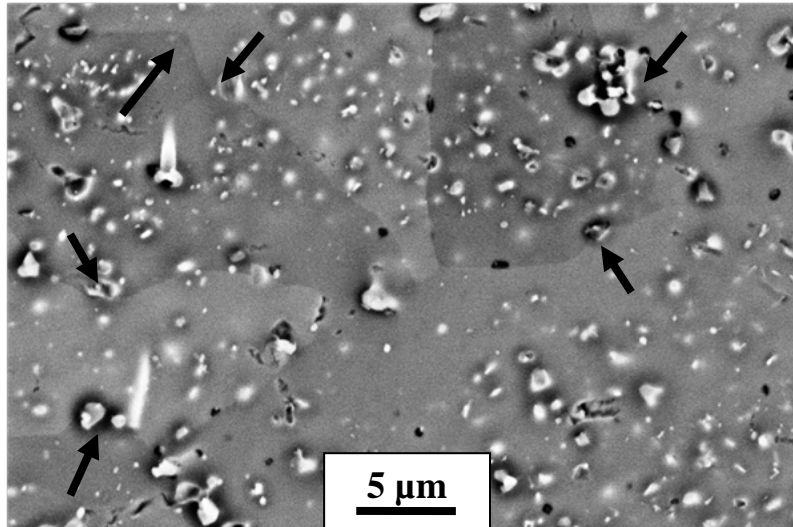


Figure 5-21. a) Backscattered and b) secondary SEM images of an identical area of the NA-CR-380-20m sample.



**Figure 5-22. Backscatter SEM image of the NA-CR-380-20m sample. Arrows point to grain boundary pinning by precipitates.**

### **5.2.3. Microstructural characterization through EBSD**

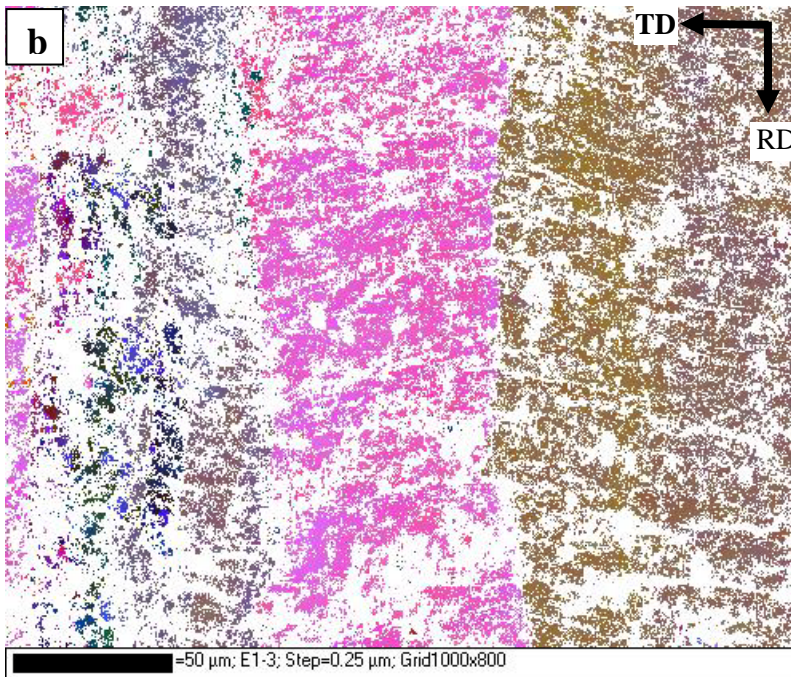
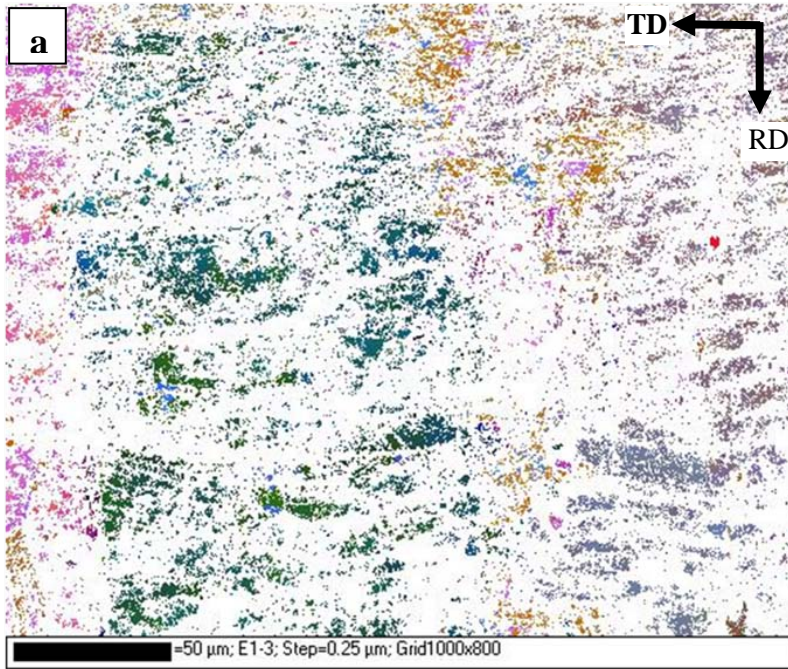
The main objective of the EBSD analysis has been to study microstructural evolution through the formation of recrystallized nuclei/grains, as well as the evolution of grain boundary misorientation. The results of the EBSD tests, which have been performed on the cold-rolled samples annealed to various temperatures in the range of 180°C to 380°C, are presented in this section.

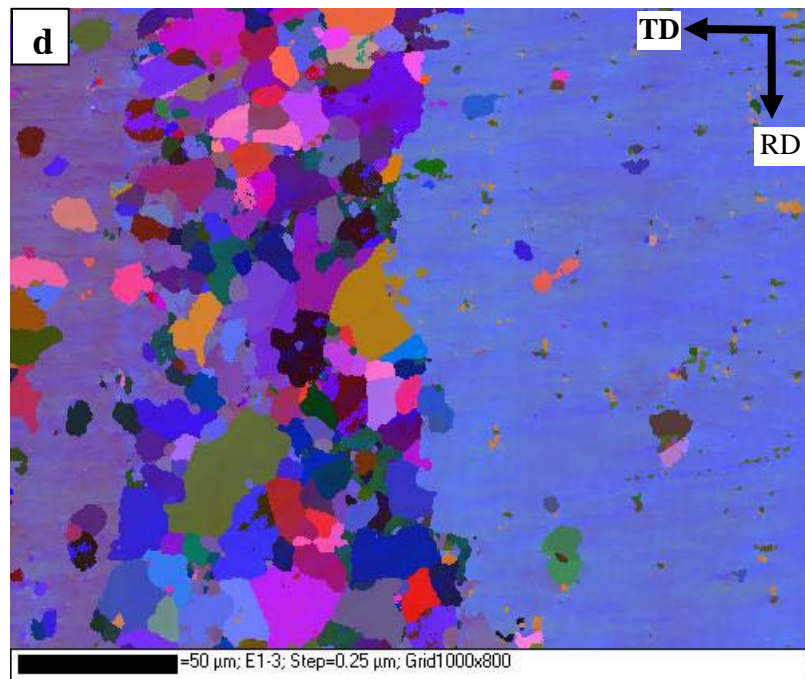
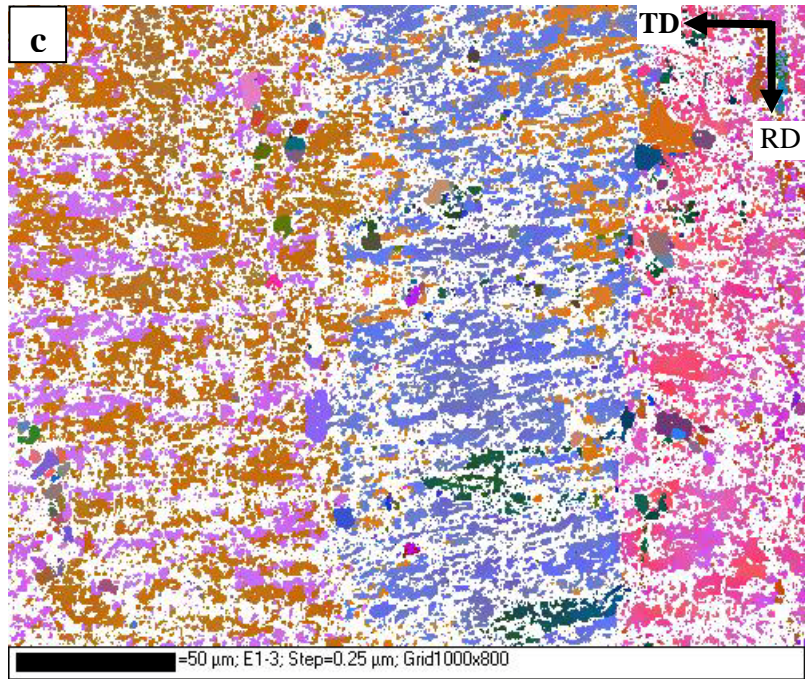
The EBSD orientation maps of these samples are presented in Figure 5-23. The orientation maps are constructed from crystal orientations collected point by point over the scanned area. Euler orientation for each point is represented by a different color on the map. The white points of the map arise from the non-indexed data points. A significantly higher frequency of these points is observed in the EBSD map of the NA-CR-180 sample, as compared to the rest of the samples.

In addition to grain structure maps, EBSD analysis can provide detailed information on the local misorientation of different sites of the microstructure. Therefore, to obtain a clear view of the low/high angle grain boundary distribution, grain boundary maps have been produced by HKL channel 5 software\*. In Figure 5-24, blue and black lines represent boundaries with misorientation of 2-15° and over 15°, respectively. Due to the large number of undetected points in the EBSD map of the NA-CR-180 sample, the boundary map for this condition contains artifacts, and as a result, is not included in Figure 5-24. The EBSD orientation map of the NA-CR-180 sample (Figure 5-23 (a)) does not show formation of any recrystallized area. Few recrystallized nuclei/grains are observed in the grain boundary map of the NA-CR-235 sample (Figure 5-23(b) and Figure 5-24(a)). The EBSD maps of the sample annealed to 300°C show the formation of new recrystallized grains surrounded by high angle grain boundaries. The newly recrystallized grains are observed both in the orientation and grain boundary maps (Figure 5-23(c) and Figure 5-24(b)). These new grains are mainly distributed uniformly inside the deformed grains, while some of them are formed on the previously existing grain boundaries. Continuing annealing to 320°C has led to an increase in the recrystallized area fraction. The EBSD maps of the NA-CR-320 sample show a non-uniform distribution of recrystallized grains at this condition. A recrystallized band consisting of large grains is observed, while in the rest of the map, randomly distributed small recrystallized grains are present (Figure 5-23(d) and Figure 5-24(c)).

---

\* The software that has been used for EBSD data acquisition.





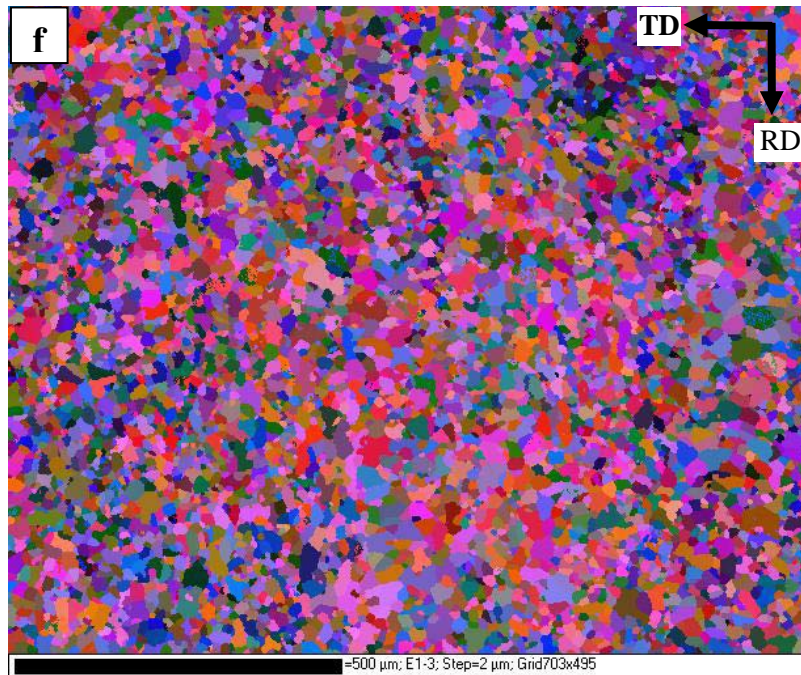
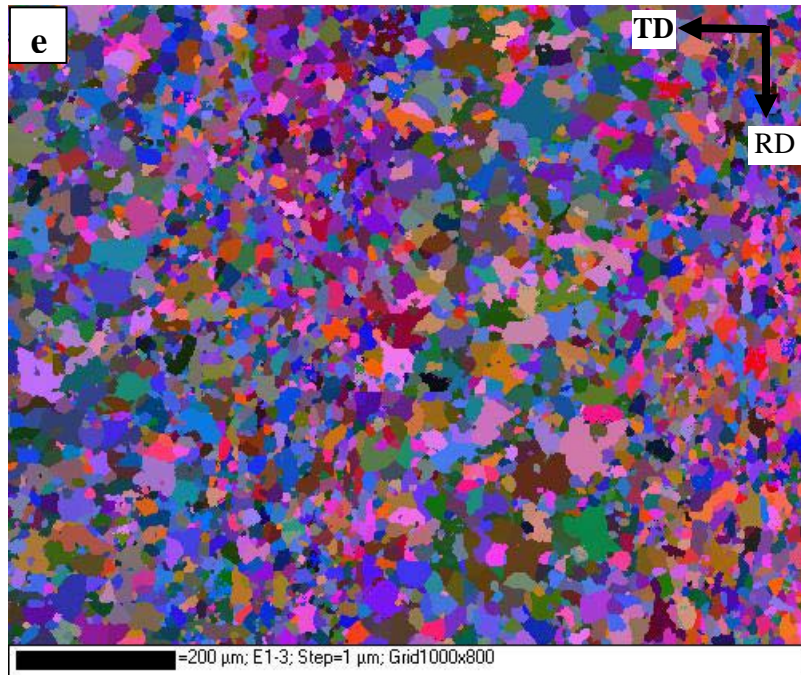
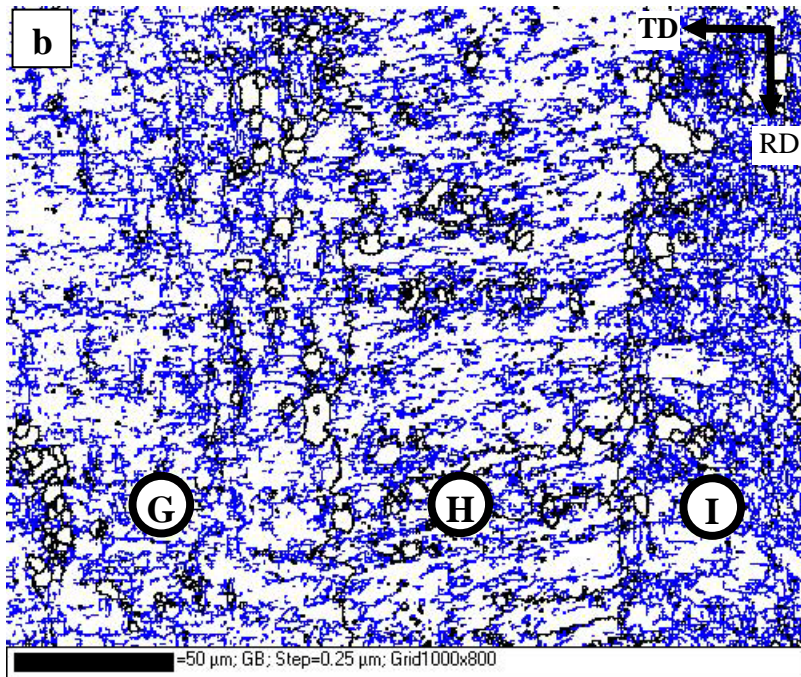
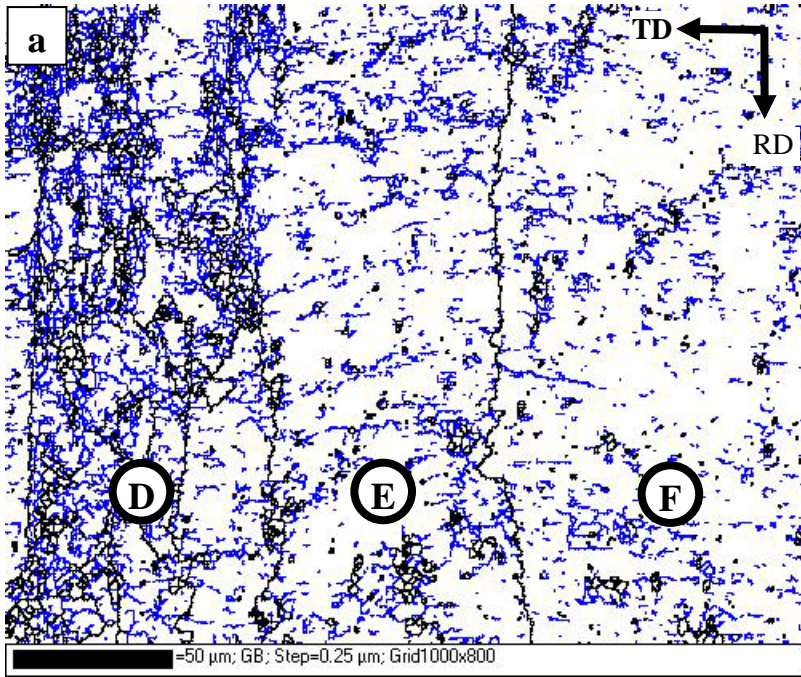


Figure 5-23. EBSD orientation maps of a) NA-CR-180, b) NA-CR-235, c) NA-CR-300, d) NA-CR-320, e) NA-CR-340, and f) NA-CR-380-20m samples (EBSD test performed by H. Jin).



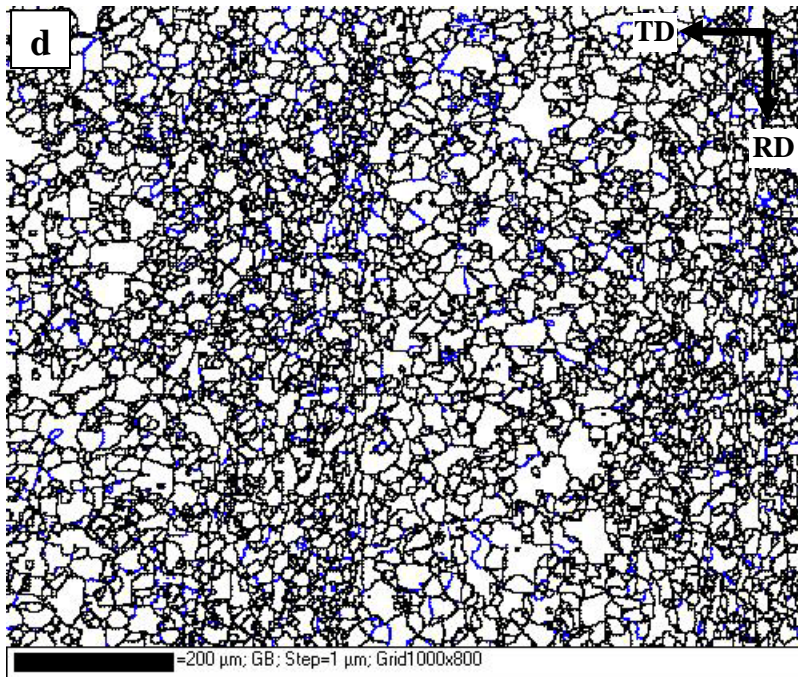
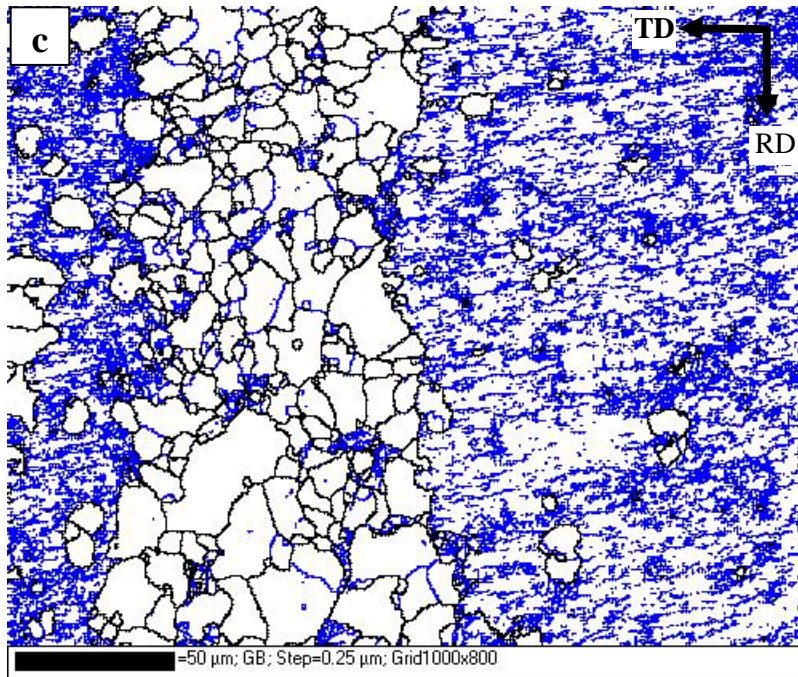


Figure 5-24. EBSD grain boundary maps of a) NA-CR-235, b) NA-CR-300, c) NA-CR-320, d) NA-CR-340 samples ; black  $\geq 15^\circ$ , blue =  $2^\circ - 15^\circ$  (EBSD test performed by H. Jin).

EBSD analysis of the NA-CR-340 and NA-CR-380-20m samples (Figure 5-23(e) and (f) and Figure 5-24(d)) have revealed the formation of substantially recrystallized structures. The grain size distributions for these two conditions are presented by the histograms of Figure 5-25. A lognormal distribution of grain size is observed for these two conditions. Average grain diameters of NA-CR-340 and NA-CR-380-20m, have been calculated as 9.8 $\mu$ m and 11.44, respectively.

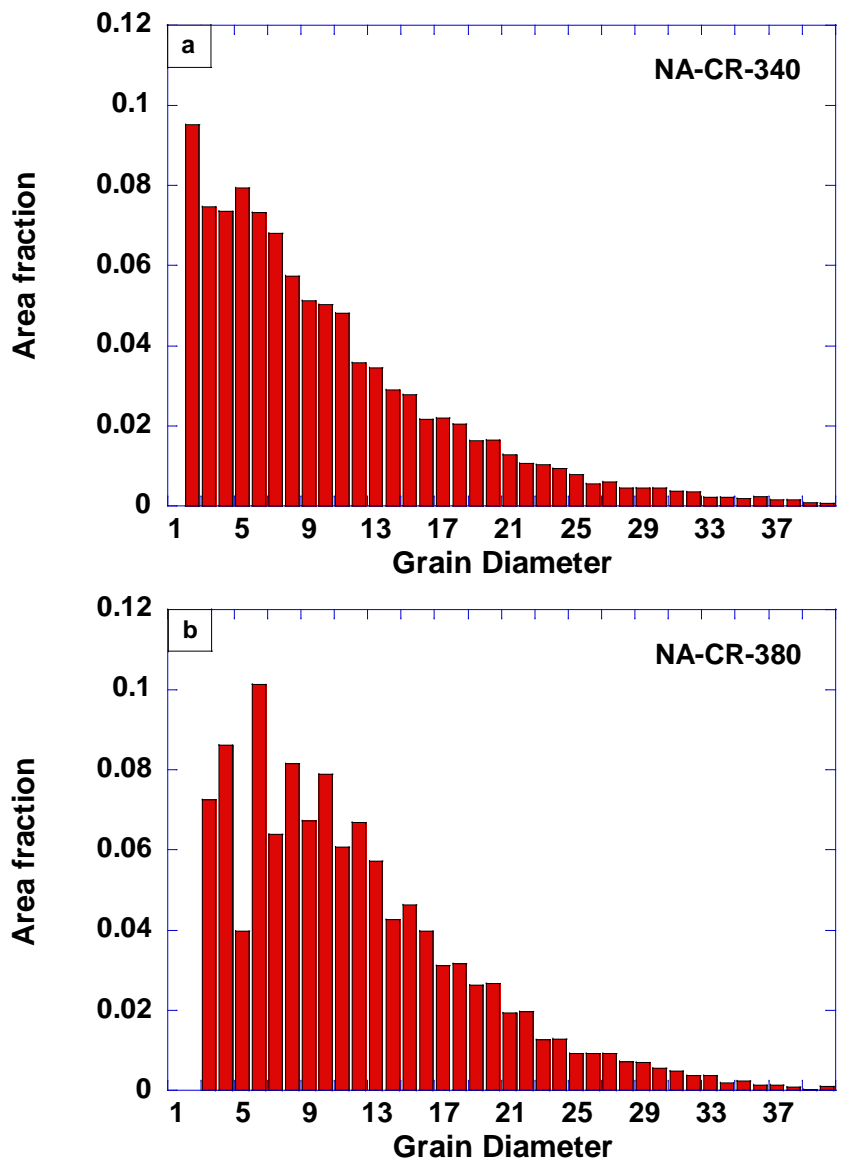


Figure 5-25. Grain size distribution calculated from EBSD results on a)NA-CR-340, and b)NA-CR-380-20m samples.

### **5.3. Discussion**

In this section, experimental results which have been presented in Section 5.1 are discussed and analysed to better understand the interactions between precipitation and annealing phenomena and to identify the mechanism of microstructural evolution during the TPM. The results of this section will be used in simulating microstructural evolution during recrystallization as presented in Section 6.3.

#### **5.3.1. Precipitate evolution during non-isothermal annealing**

Precipitates have a strong effect on dislocation distribution during deformation as well as microstructural evolution during annealing [2, 4, 6, 103]. Precipitates which form during natural aging and early stages of the annealing are too fine to be detected through conventional TEM investigation. Therefore, in this section, DSC results are used to analyse and discuss precipitation states prior to cold rolling, in the as-deformed condition, and during non-isothermal annealing.

Precipitation events initiate prior to cold rolling, when the solutionized alloy plate undergoes natural aging process. The precipitate state of the naturally-aged plate is examined by comparing DSC thermograms of the AQ and NA samples presented in Figure 5-1. The difference between these two DSC traces arises from natural aging. The remarkable reduction in the height of the clustering peak of the DSC thermogram of the NA plate, compared to AQ condition, provides evidence for the formation of clusters during natural aging. This observation is supported by the literature that has been widely reported cluster formation during natural aging of AA6xxx alloys (e.g. [18, 133]). The presence of major precipitation peaks on the DSC thermogram of the NA sample shows that natural aging does not result in

the complete depletion of matrix from solute. Therefore, the naturally-aged plate contains clusters and solutes, prior to rolling.

Annealing phenomena and precipitation are both exothermic events and occur concurrently during the DSC tests on cold-rolled samples. The results of tests on Al-CR are discussed to determine if the recorded exothermic heat effects of cold-rolled samples are purely due to precipitation or whether they are an overlap effect from annealing and precipitation processes. As shown in Figure 5-3, the Al-CR sample softens during non-isothermal annealing. This softening is due to the recovery and recrystallization mechanisms [3]. Since no noticeable heat effect is observed on the DSC trace of Al-CR, it is concluded that the amount of heat released due to annealing effects, in pure Al and consequently in AA6451 samples, in the temperature range of 25-300°C, is too small to be detected by the DSC machine employed in this study. Such observation is not unexpected, as the amount of heat released during recovery and recrystallization is remarkably smaller than the heat released during precipitation [3]. Thus, all the peaks observed on the DSC curves of the cold-rolled samples (NA-CR and AQ-CR) are considered as being arisen from precipitation events. Therefore, the DSC curves for the deformed and non deformed samples are considered to be comparable.

To have a better perspective on the effect of cold rolling on the precipitation behaviour, DSC traces of AQ-CR, NA-CR, AQ and NA samples are plotted in Figure 5-26. Comparing DSC traces of NA-CR and NA samples, it is observed that the initial part of the curves, between 50°C and 100°C, are very similar. As explained in Section 2.1.3, dislocations may suppress the formation of clusters by consuming the quenched-in vacancies. Therefore, the absence of clustering peak in the DSC trace of the NA-CR sample does not necessarily mean

that clusters have been present before performing the DSC run (i.e non-isothermal annealing). In fact, they might dissolve during deformation by dislocation shearing [46, 91], and subsequently new clusters did not form during the DSC run due to the consumption of quenched-in vacancies by dislocations [49, 55]. However, the higher initial hardness of the NA-CR sample compared to that of the AQ-CR sample (Figure 5-3) provides strong evidence for the presence of a significant population of clusters at the start of annealing of the NA-CR sample. Furthermore, the absence of peak A on the DSC trace of the AQ-CR samples suggests that either the sample has lost its clustering potential due to the loss of quenched-in vacancies, or some clusters have formed dynamically during the cold rolling operation of the as-quenched sample. However, the pronounced similarity between the DSC traces for AQ-CR and NA-CR suggests that the starting microstructure of AQ-CR also had clusters.

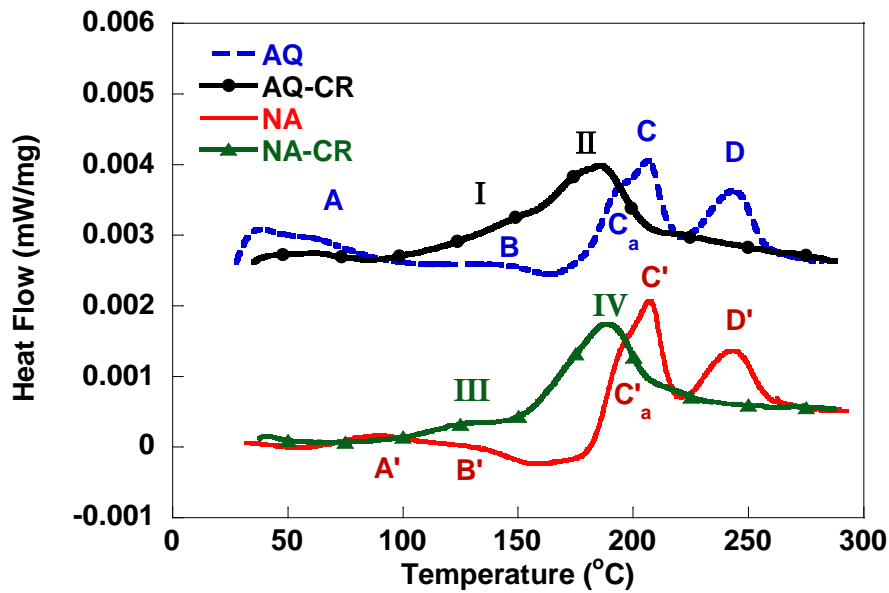


**Figure 5-26.** The DSC thermograms for the as-quenched (AQ), as-quenched and cold-rolled (AQ-CR), naturally-aged (NA), and naturally-aged and cold-rolled (NA-CR) samples.

The precipitation events that occur during the non-isothermal annealing part of TMPM, are represented by the heat effects in the DSC thermogram of the NA-CR and AQ-CR samples. In comparing the DSC thermograms of the cold-rolled samples with those of the non-deformed samples, it is seen that, in agreement with literature [49-52, 54, 58], deformation enhances precipitation kinetics and shifts precipitation events to lower temperatures. Main precipitation events on the cold-rolled alloy seem to start at temperatures as low as 100°C during the non-isothermal annealing process.

The evolution of precipitation in the NA-CR sample, at various annealing conditions, is examined through the co-presentation of DSC and microhardness measurement results for NA and NA-CR samples (Figure 5-27). These results show that early stage precipitates associated with peaks A' and B' provide small hardening effects, while precipitates associated with peaks C<sub>a</sub>', C' and D' are highly effective in increasing hardness. The maximum level of hardness coincides with the completion of precipitation event C'. The subsequent decrease in hardness is therefore attributed to the coarsening of C'-type precipitates and their replacement by a D'-type precipitate phase [135]. The results of the microhardness measurements on the NA-CR sample represent overlapping effects of precipitation and recovery-recrystallization processes. This overlap at the initial stages of annealing comprises hardening due to precipitation and potentially partial recovery of accumulated dislocations. In the later stages, softening mechanisms for precipitate coarsening/transformation and recovery/recrystallization overlap. The slight initial increase in hardness matches well with the associated small exothermic event I on the DSC trace of NA-CR and the lack of significant dislocation recovery (i.e. no or small softening effect) as suggested by the TEM results on the NA-CR-180 sample. On the other hand, hardness evolution suggests that softening mechanisms become prevalent when

annealing is extended above 180°C. Comparing the hardness results of the NA-CR and NA samples, the similar trends in the softening behaviour with increasing temperature in the temperatures range of 230°C to 300°C indicates the major role of precipitate coarsening/phase transformation in the softening of NA-CR when the maximum temperature of the main exothermic peak (i.e. peak II) is reached during annealing. The TEM results presented in Section 5.2.1 support precipitate coarsening above 180°C, as well. Interestingly, the two samples demonstrate significantly different softening behaviours when the temperature is increased beyond 300°C: while the hardness of the NA sample gradually decreases, hardness of the NA-CR sample shows a sudden fall. The combination of EBSD and TEM results provide compelling evidence for the initiation of recrystallization at this temperature. Therefore, this sudden change in the rate of hardness reduction is attributed to additional softening through recrystallization, while precipitation coarsening also occurs concurrently. These concepts have been used in the next chapter for including precipitate evolution in the simulation algorithm.

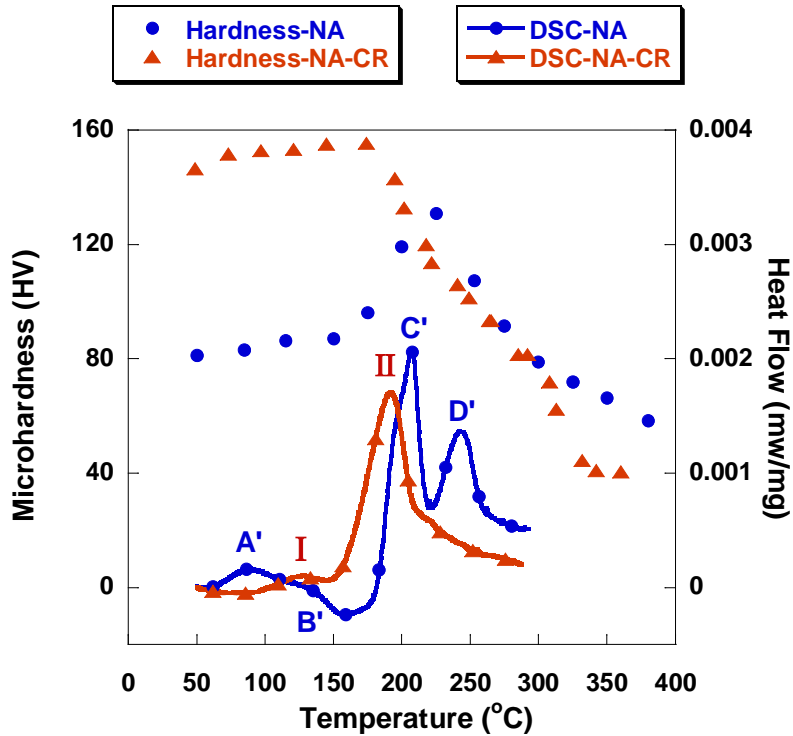


Figure 5-27. DSC thermograms and hardness evolution of naturally-aged and cold-rolled (NA-CR), and naturally-aged (NA) samples.

### 5.3.2. Dislocation arrangement in the as-deformed state

The dislocation distribution in the as-deformed material is the balance of dislocation generation and dislocation annihilation through dynamic recovery [3]. As shown in Figure 2-5, an extensively recovered microstructure forms when pure aluminum is cold-rolled to 80% reduction of thickness [86]. The uniform distribution of dislocations observed through the TEM analysis of the NA-CR sample indicates that dynamic recovery has been strongly inhibited during the deformation stage of TMPM. As discussed earlier, clusters that formed during natural aging, as well as solute elements, are present in the microstructure of the plate prior to deformation. During deformation, clusters act as obstacle against dislocation movement and inhibit or delay their re-arrangement. Dislocation movement is also inhibited

through the drag effect of remaining solutes in the matrix (Section 2.2.1.2). The combination of these two effects retards dynamic recovery during deformation. The delayed dynamic recovery leads to the presence of a rather randomly distributed high density of dislocations in the as-deformed structure and provides a large driving force for both recovery and recrystallization during annealing [3, 103, 113].

### **5.3.3. Interactions of precipitates and dislocations during annealing**

The TEM micrograph of the NA-CR-180 sample in Figure 5-5 shows a similar dislocation distribution as that of the NA-CR sample (Figure 5-4). This resemblance indicates the retardation of recovery events during annealing, from 50°C to 180°C, in spite of the high driving force available for recovery. The presence of a large number of non-indexed points on the EBSD maps of the NA-CR-180 sample (Figure 5-23(a)), which is the characteristics of highly deformed structures [133, 137], supports retardation of recovery on a larger scale than the TEM field of observation. Inhibition of recovery is mainly due to the retarding effect exerted by precipitates against dislocation movement, as discussed below. It should be mentioned that, the uniform dislocation distribution has been used as the basis for generation of initial structure in the computational modeling technique described in Section 6.3.

TEM analysis on NA-CR-180 has revealed the presence of very fine precipitates at this annealing condition. As shown in the pair of dark field and bright field TEM micrographs of Figure 5-6, a large number of precipitates are present in areas with a high density of dislocations. Such precipitate distribution may be explained by the following reasons:

- 1- Dislocations are high energy areas and may act as heterogeneous nucleation sites for precipitation. Therefore, precipitates can easily nucleate on the areas with a high density of dislocation.

2- Dislocations act as easy diffusion paths for solutes and, thus, result in the enhanced growth of precipitates associated with them.

Previous works suggest that these precipitates which form during initial stages of the alloy's precipitation sequence are coherent/partially coherent precursors of the stable phases and act as shearable obstacles against dislocation movement [19, 36]. Therefore, their retarding effect against dislocation movement is analysed through Equation (2-16) [100]:

$$\tau_c = \frac{Gb}{L_p} \left( \frac{F_m}{2\Gamma} \right)^{3/2} \quad (2-16)$$

As reviewed in Section 2.2.2.2, by growth of these precipitates,  $F_m$  increases, while the average spacing between precipitates ( $L_p$ ) decreases. Therefore, the magnitude of the precipitate pinning effect, i.e.  $\tau_c$ , against dislocation movement, increases.

Although progress of precipitation in the temperature range of 50°C-180°C leads to the increase of their retarding effect against dislocation movement, precipitate nucleation and growth results in the depletion of the solute from matrix and, in turn, leads to reduction of the solute drag effect against dislocation movement. The overall dislocation movement during this early stage of annealing is controlled by the balance of the decreasing solute drag effect and the increasing precipitate pinning effect. Considering the structure observed in Figure 5-5, it is concluded that the overall retarding effect is strong enough to delay recovery in the sample annealed to 180°C.

As DSC, microhardness measurements and TEM results show, continuing annealing above 180°C results in overaging and precipitate coarsening. During coarsening, the average radius of precipitates, along with their interprecipitate spacing, increases. Considering that at this stage of precipitation, dependency of  $F_m$  to size of the precipitate decreases [31], an increase of  $L_p$  leads to a decrease of the retarding effect of precipitates against dislocation

movement. In addition, the enlargement of interprecipitate spacing facilitates dislocation movement on small scales (between precipitates).

The high concentration of uniformly distributed dislocations in the microstructure of the sample annealed to 235°C (Figure 5-7), suggests that due to the high number density of uniformly distributed precipitates, the large scale movement of dislocations is still inhibited for this annealing condition. TEM micrographs in Figure 5-11 help in analysing the dislocation-precipitate interaction for this annealing condition. In the micrograph of Figure 5-11, large precipitates are seen close to and on one side of the dislocation wall. On the other hand, in the sample which has been annealed to a lower temperature (Figure 5-6) larger precipitates have been seen to be located on the dislocations. Considering these two types of dislocation-precipitate distribution, the process of dislocation-precipitate interaction and movement of the dislocation wall are summarized into the following sequential steps:

1. At early stages of annealing (Figure 5-6), the dislocations are pinned with small shearable precipitates.
2. Through further annealing, the precipitates which are located on the dislocations and pinned them, coarsen/transform faster than other precipitates.
3. As the precipitates coarsen, their pinning effect decreases and dislocations can move.
4. When the dislocations move, they interact with new small precipitates which are located in areas with lower density of dislocations.
5. Small precipitates pin the moving dislocations and suppress their further movement.
6. Repeat of steps 2-5.

Considering the above sequence of precipitate-dislocation interactions, the direction of dislocation-wall movement is suggested to be along the arrows shown in Figure 5-11.

Although, large scale dislocation movements are strongly hindered by precipitates, high magnification TEM analysis (Figure 5-8) reveals subgrain formation after annealing to 235°C. These subgrains are formed through localized dislocations rearrangement, wherever the interacting forces between the dislocations, which provide the driving force for dislocation movement, can locally overcome the pinning effect of precipitates. These subgrains are surrounded by LAGBs which have limited mobility [3, 114]. Furthermore, it has been shown through TEM observations (Figure 5-12) that in the samples annealed to 235°C, subgrain boundaries are pinned by precipitates. The combination of the low mobility of LAGBs and the strong pinning effect of precipitates limits the growth of subgrains at 235°C.

Annealing to higher temperatures enhances diffusional mechanisms that lead to the increase in the precipitate coarsening rate, the enhancement of dislocation movement and an increase of grain boundary mobility. Such a condition favours both recovery and recrystallization. The TEM micrograph of the NA-CR-300 sample presented in Figure 5-13 shows a partially recovered microstructure with a low density of dislocations compared to NA-CR-235. The combination of microhardness results, EBSD and TEM analysis shows evidence for the initiation of recrystallization at this condition. Therefore, the observed microstructure in Figure 5-13 is believed to be evolved through a combination of recovery and recrystallization processes.

The above analyses show that large scale recovery is retarded by the strong pinning effect of precipitate during initial and intermediate stages of annealing. Therefore, a large driving force for recrystallization remains in the system. On the other hand, small scale dislocation movement provides uniformly-distributed subgrains. A subgrain may grow and transform to a recrystallized nucleus through further annealing. The combination of uniformly

distributed subgrains and the high driving force for recrystallization provides a favoured condition for the uniform distribution of recrystallized grains and the effective progress of recrystallization at later stage of the non-isothermal annealing.

#### **5.3.4. Microstructural evolution during recrystallization**

Although no recrystallized nuclei have been detected through TEM analysis on samples annealed to 235°C, the EBSD grain boundary map of the NA-CR-235 sample (Figure 5-24 (a)) shows the formation of new high angle grain boundaries. For a quantitative representation of misorientation distribution within the deformed grains of Figure 5-24 (a), point to point misorientation (PPM) is calculated across the grain boundary map. To obtain a representative scan of the whole structure, scans have been performed along three equally-spaced lines crossing the EBSD boundary map. No remarkable difference between the three scans is observed, implying that the misorientation distribution inside each grain is fairly uniform. Misorientation is computed through the technique described in Appendix (A2) based on the Euler angles obtained from the EBSD analysis. PPM graphs along with the original EBSD boundary map are presented in Figure 5-28. Misorientation peaks above 15° show the presence of HAGBs. This figure shows that while most of the boundaries within grains E and F are LAGBs, grain D includes a large number of HAGBs. Formation of new HAGBs in a specific grain is related to the activation of extended recovery mechanisms in that grain [138]. It has been suggested that extended recovery occurs due to the enhanced dislocation glide on low indexed planes of preferentially oriented grains and, in turn, facilitates dislocation rearrangement [138]. However, texture analysis has revealed that the fraction of the microstructure which undergoes extended recovery is limited [138]. Hence, it is suggested that in most of the structure, progress of recovery is inhibited due to the pinning effect of

precipitates. The absence of recrystallized nuclei in the TEM analysis of the NA-CR-235 sample, therefore, is due to the fact that TEM observations have not been conducted on preferentially orientated grains. As TEM foils have been prepared from random sites of the sheet, and considering that only a small fraction of grains undergoes preferential recovery, there is a small chance that these foils contain the grain preferentially orientated for extended recovery.

The same type of PPM graphs have been presented in Figure 5-29 for the NA-CR-300 sample. The remarkable formation of HAGBs for this condition implies initiation of recrystallization in all three grains of the EBSD map. TEM observations on NA-CR-300 have supported the formation of a large number of recrystallized nuclei (Figure 5-14) as well as well-developed recrystallized grains (Figure 5-15 and Figure 5-16).

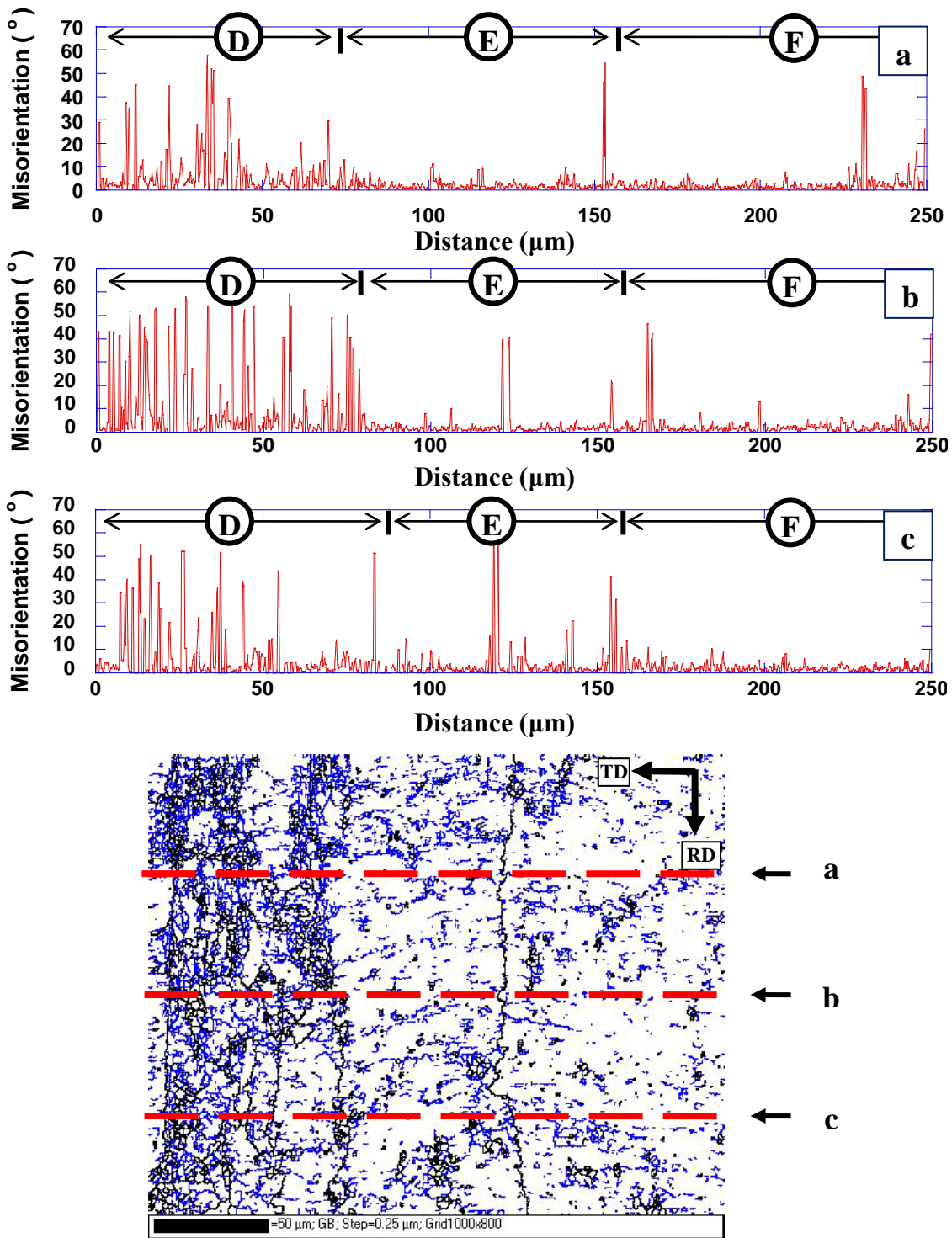


Figure 5-28. Point to point misorientation distribution along a) dashed line a b) dashed line b and c) dashed line c on the EBSD boundary map of the NA-CR-235 sample.

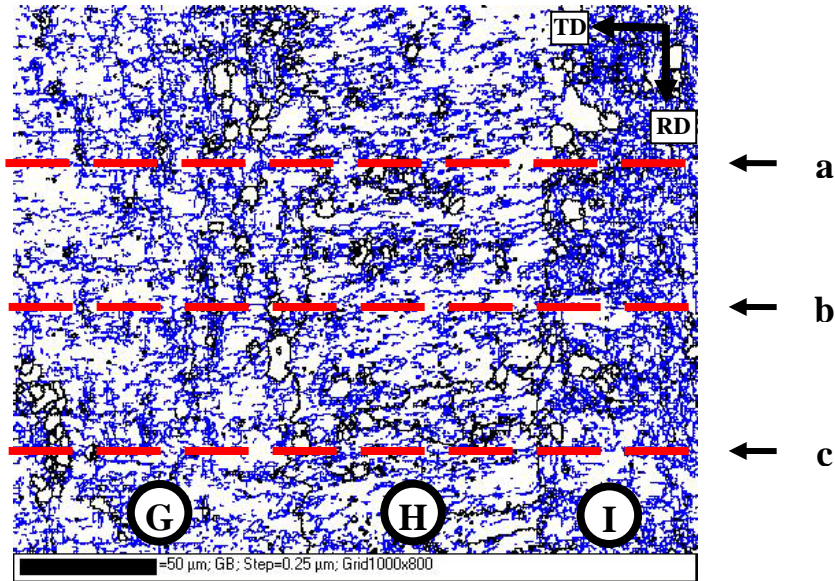
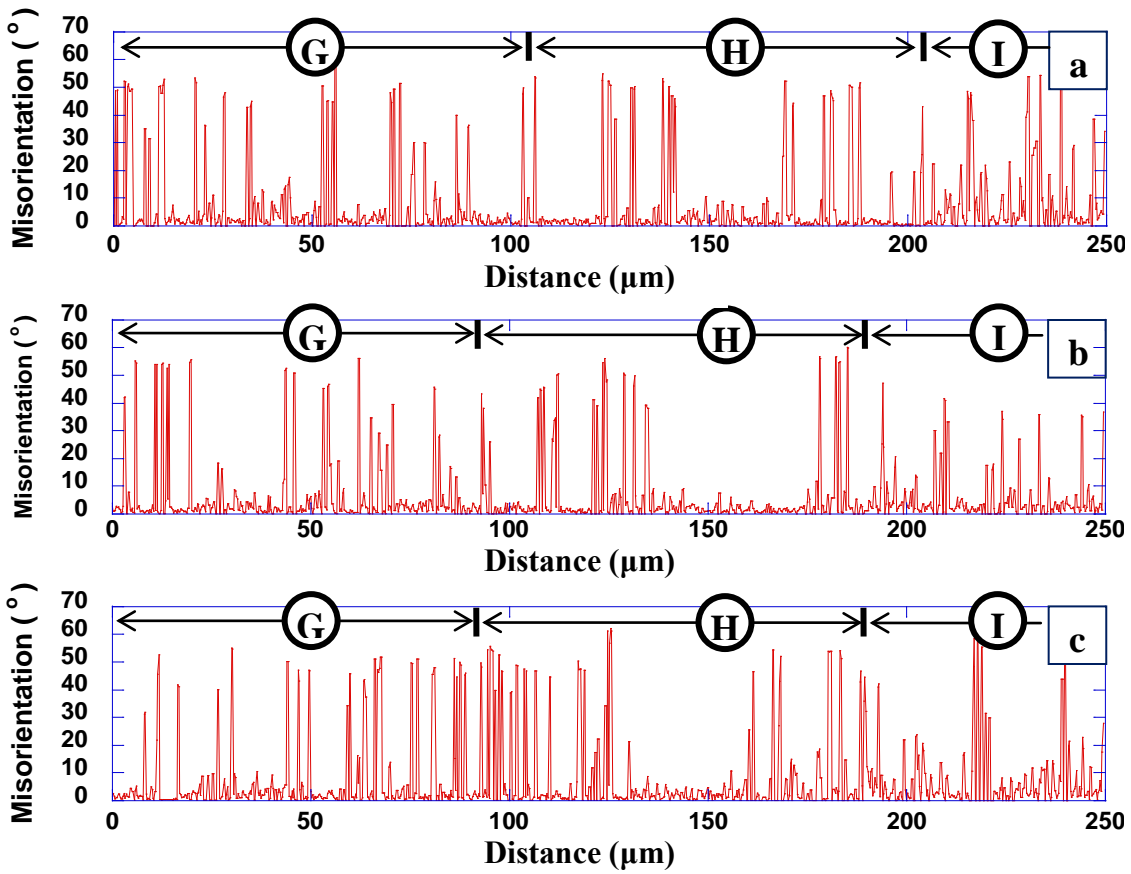
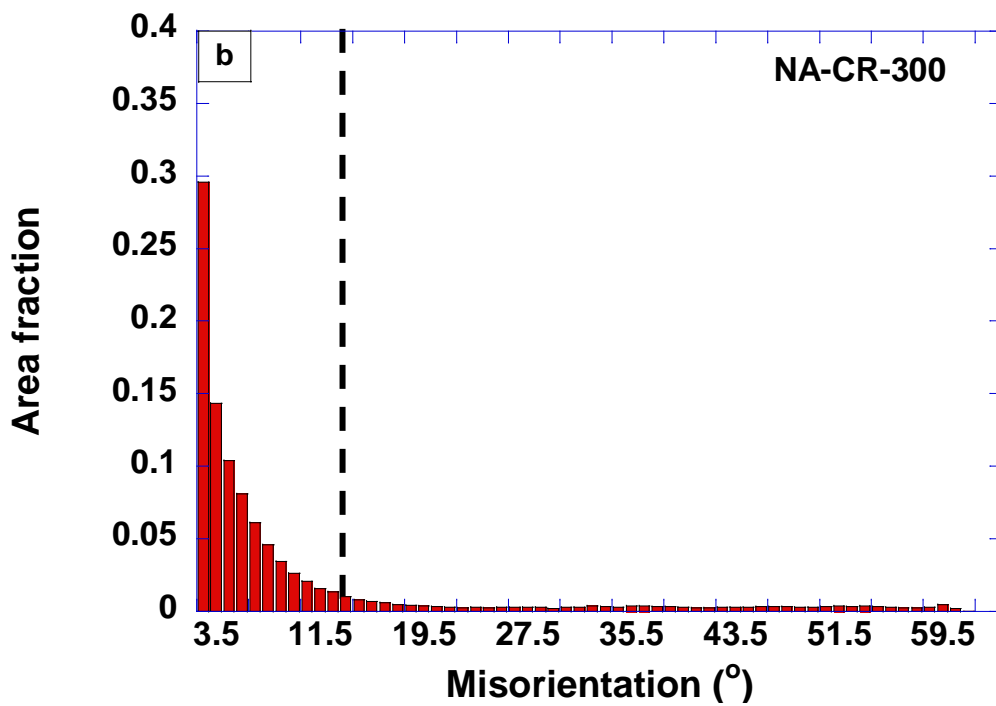
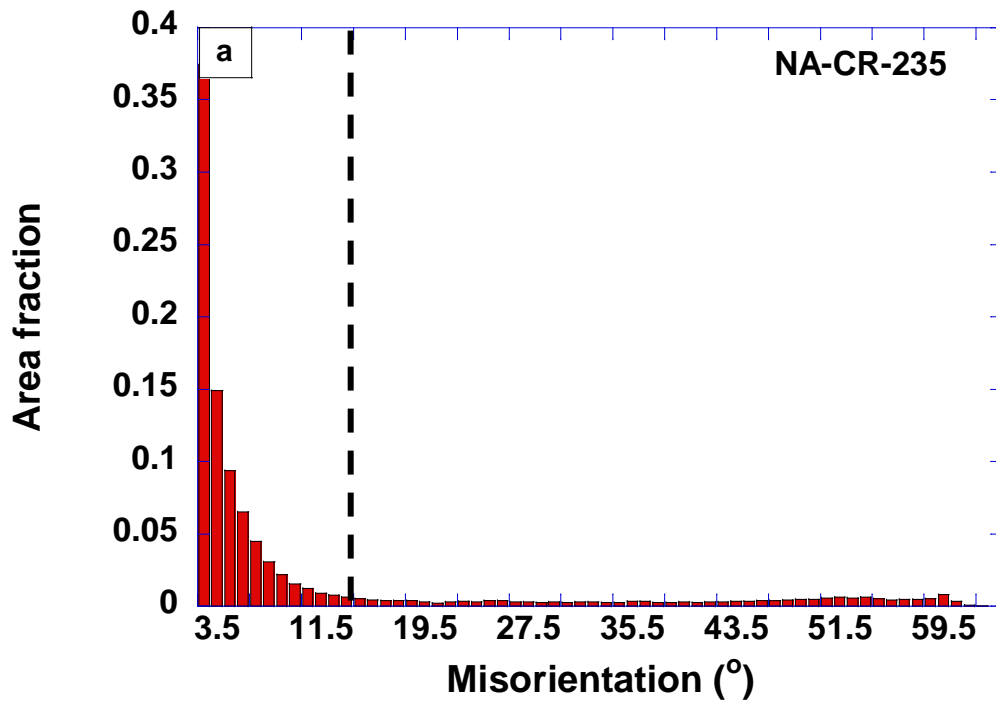
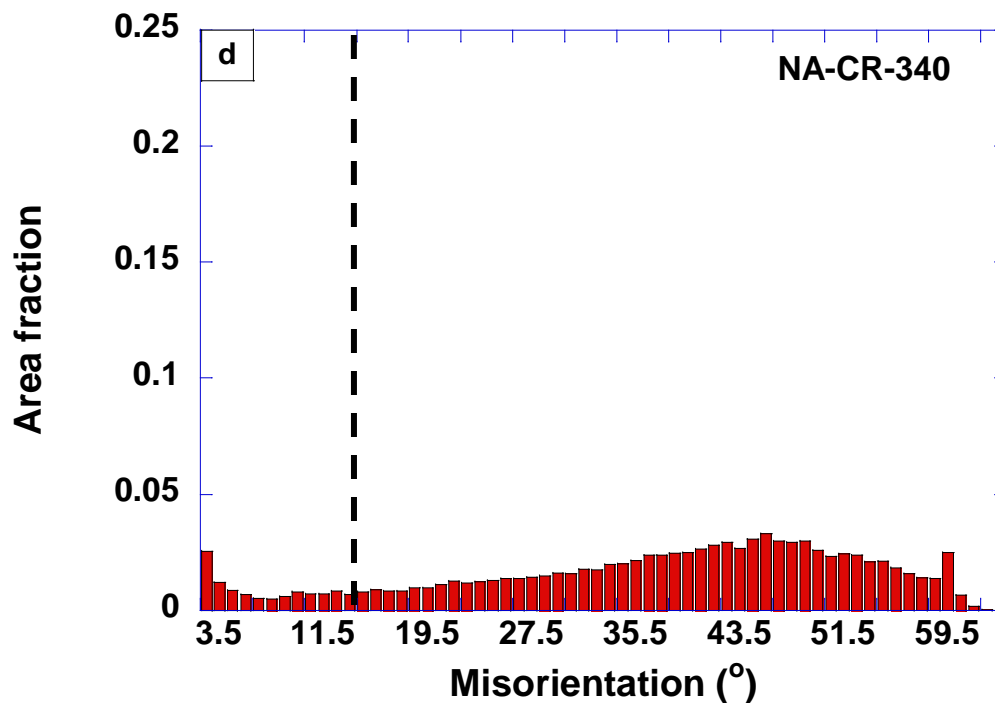
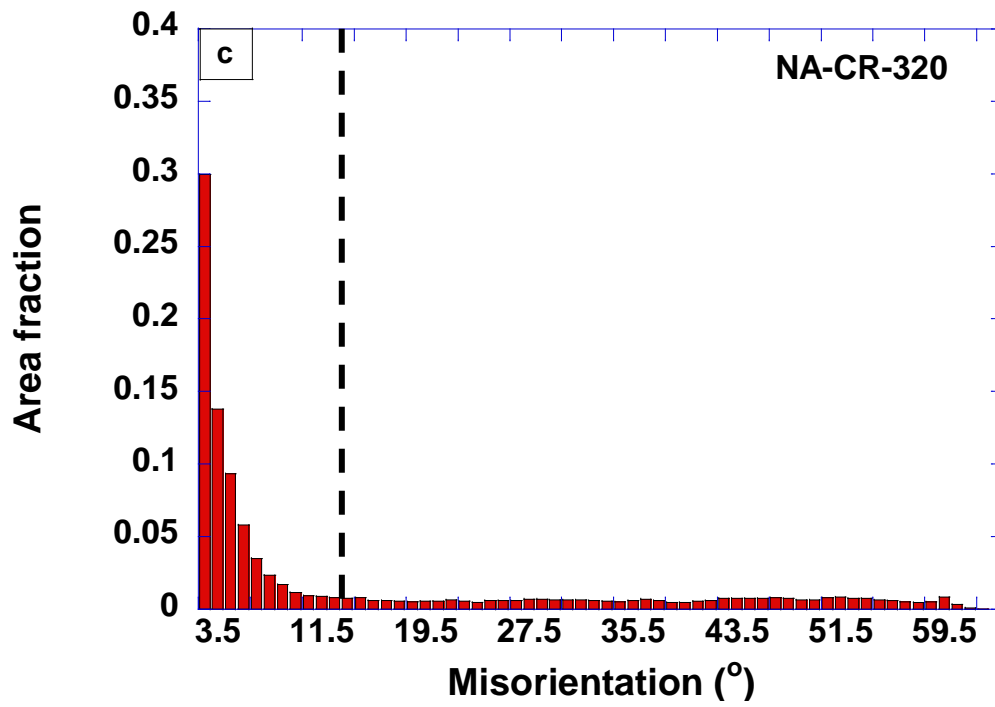


Figure 5-29. Point to point misorientation distribution along a) dashed line a b) dashed line b and c) dashed line c on the EBSD boundary map of the NA-CR-300 sample.

Qualitative analysis of EBSD boundary maps presented in Figure 5-24 provide evidence for an increase in the fraction of HAGBs through the formation of new nuclei/grains by progress of recrystallization. Such behaviour may be better analysed when the distribution of misorientation for each condition, which is obtained from channel 5 software, is plotted as histograms. Figure 5-30 shows the misorientation distribution for the EBSD maps of Figure 5-24(a) to (d). The boundary character distribution data provided in Figure 5-30 is separated into high angle and low angle grain boundaries by division at  $15^\circ$ . For the samples annealed to  $235^\circ\text{C}$ ,  $300^\circ\text{C}$  and  $320^\circ\text{C}$  the peak of histogram is located below  $15^\circ$ . On the other hand, the histogram peak for samples annealed to  $340^\circ\text{C}$  and  $380^\circ\text{C}$  are located above  $15^\circ$ . Shift of the histogram peak to higher values during non-isothermal annealing, implies progress of recrystallization. As proposed by other researchers (e.g. [108, 109]), the evolution of HAGB during annealing may be used as a characterization parameter to follow recrystallization. To analyse evolution of boundary characteristics during annealing, area fractions of boundaries with various misorientation angles are computed using Channel 5 software. Subsequently, this data has been used to calculate fraction of HAGBs (i.e. misorientation angles of  $15^\circ$  and above) for each condition as plotted in Figure 5-31.





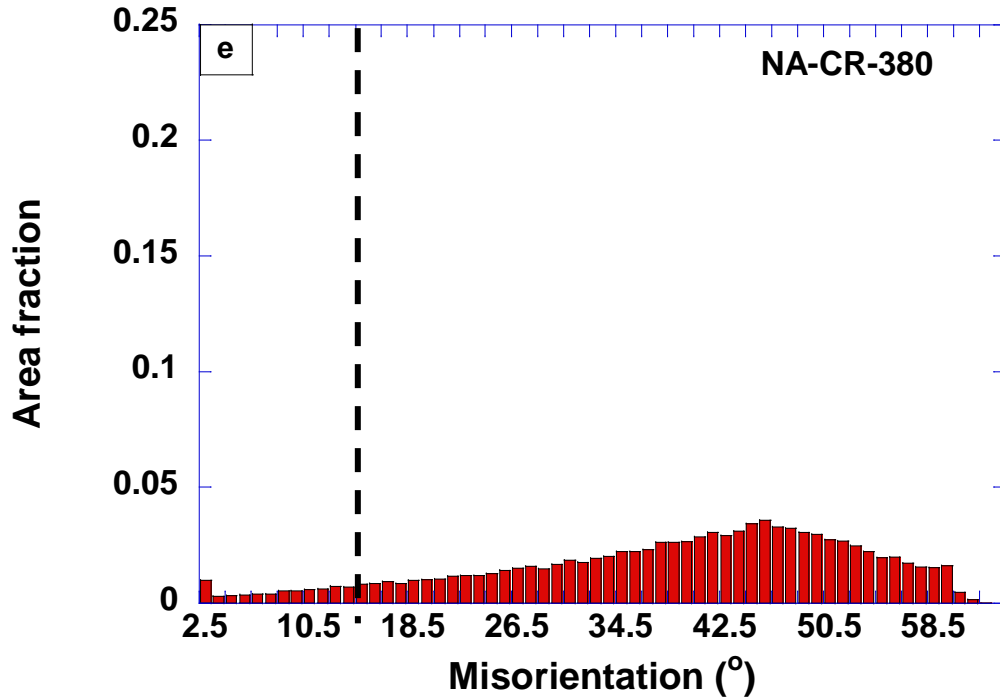


Figure 5-30. Grain boundary character distribution for the EBSD maps of a) NA-CR-235, b) NA-CR-300, c) NA-CR-320, d) NA-CR-340 and e) NA-CR-380. The dashed line shows the division between high angle and low angle boundaries ( $15^\circ$ ).

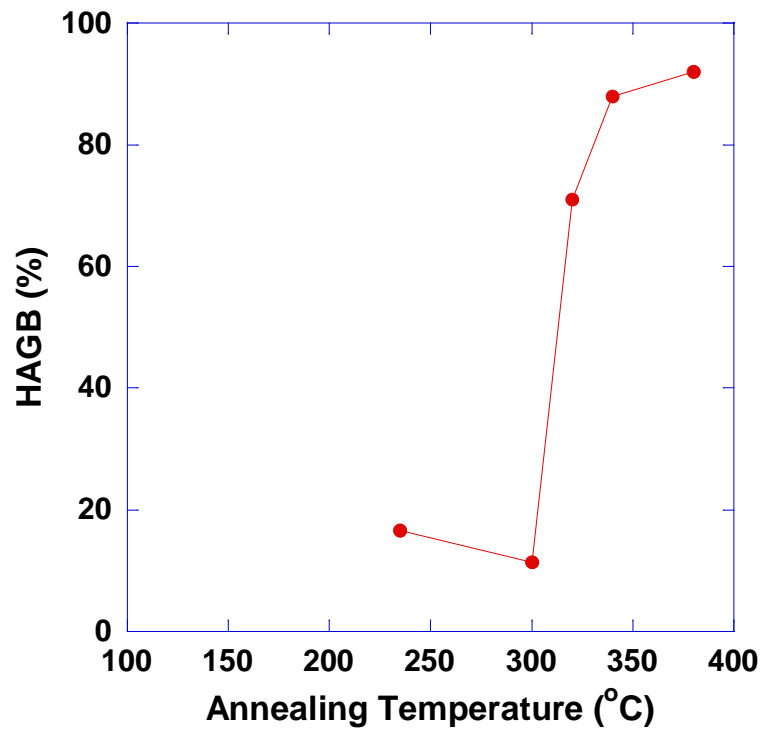


Figure 5-31. Evolution of high angle grain boundary fraction (HAGB%) as a function of the end annealing temperature of the non-isothermal annealing process.

In a general view, the evolution of HAGB% with temperature presents an *S* shape curve, which is in agreement with the typical sigmoidal shape when recrystallization fraction is plotted vs. annealing time/temperature [3, 103]. Interestingly, the curve shows a sharp increase in HAGB% in the temperature range of 300°C to 340°C. This sharp increase is the characteristic of discontinuous recrystallization where the deformed substructure is consumed by the recrystallizing grains [108, 109]. It should be mentioned that if continuous recrystallization occurs as the general recrystallization trend, small changes in the HAGB% would be observed and the deformed structure would gradually transform into the recrystallized structure [108, 109]. TEM and EBSD analysis have also provided evidence for microstructural evolution through nucleation and growth, which is the characteristic of discontinuous recrystallization. The sharp increase in %HAGBs also implies that recrystallization mainly occurs in the temperature range between 300°C and 340°C. TEM and microhardness measurement results support this behaviour. Accelerated recrystallization between 300°C and 340°C is attributed mainly to the following main reasons:

1. large driving force for recrystallization due to the delay of recovery which leads to the maintenance of a high density of dislocations in the deformed regions, up until significant recrystallization occurs;
2. increase in grain boundary mobility due to the temperature rise (Equation (2-20));
3. enhanced precipitate coarsening due to temperature rise (Equation (2-3)) and, as a result, decrease in the precipitate pinning effect against grain boundary movement (Equation (2-21)).

The EBSD maps of the sample annealed to 320°C (Figure 5-23(d) and Figure 5-24 (c)) show preferred recrystallization in one of the grains, while the neighbouring grains are still at

the early stages of recrystallization. The result of texture and orientation analyses related this behaviour, as in the case of lower temperatures (Figure 5-28), to preferential recovery in specific grains [138]. The result of the SEM analysis on a relatively large area of the NA-CR-320 sample (Figure 5-20) supports the formation of recrystallized bands at this annealing condition. However, Figure 5-20 shows that recrystallized bands occupy only a small portion of the structure. Therefore, it is concluded that the contribution of preferred orientation on microstructural evolution is small. Such a conclusion has also been supported by a texture analysis associated with this work [138]. It has been shown that preferential recrystallization in specific orientation results in the formation of bands with a significant Cube texture component. Considering the fact that a randomized texture has been achieved after the entire structure is recrystallized, the occurrence of extended recovery in specific grains and the subsequent enhanced recrystallization in these grains is minimal [138].

Continuing annealing to 340°C results in the formation of a substantially-recrystallized structure as shown in Figure 5-23 (e). Considering that the approximate average distance between recrystallized bands for the NA-CR-320 condition is 650µm (Figure 5-20), and the fact that the EBSD map of Figure 5-23(e) represents an 800µm x 1000µm area, it may be safely assumed that the presented EBSD map includes regions evolved through enhanced recrystallization. The relatively uniform microstructure of NA-CR-340 provides further evidence for the small effect of the early recrystallized grains in microstructural evolution. In general, combination of EBSD, TEM and microhardness measurement has suggested that recrystallization mainly occurs through a nucleation and growth mechanism. Although, evidence for preferential nucleation at constituents/dispersoids (PSN effect) and grain boundaries has been detected through TEM analysis, the number of randomly distributed

recrystallized nuclei in the microstructure is much larger than the preferentially nucleated grains. It should be noted that the effect of PSN on recrystallization nucleation has been studied through implementing TPM on a custom-fabricated high purity, and a conventional extruded AA6111 bar with similar composition to AA6451<sup>†</sup> [140]. The amount of constituent/dispersoids (which can act as PSN sites) in the high purity alloy is remarkably smaller than that of the conventional alloy. Fully recrystallized microstructures have been achieved for both alloys through implementing TPM. EBSD analysis revealed a similar recrystallized structure with comparable grain size and distribution for both conditions. Therefore, it has been concluded that PSN is not the dominant nucleation mechanism during the TPM route. Similarly, nucleation at the grain boundary cannot be the main nucleation mechanism, as the smallest average grain diameter which can be achieved through this mechanism is half of the width of the deformed grain. Width of the deformed grain in Figure 5-23 and Figure 5-24 is about 70 $\mu\text{m}$  while the average grain diameter in the fully recrystallized condition (NA-CR-380-20m) is 11.4 $\mu\text{m}$ . Considering the above analysis and the large number of randomly distributed recrystallized nuclei, it is suggested that recrystallization mainly occurs through growth of the randomly distributed nuclei. These recrystallized nuclei are believed to evolve from small dislocation-free regions that pre-existed in the deformed microstructure [3, 103, 112]. This type of nucleation has been used in developing the computer simulation technique in Section 6.3 where a site saturated nucleation mechanism, i.e. all nuclei have been present at the start of annealing, has been assumed.

Although a mostly recrystallized microstructure is attained after annealing to 340°C, as the TEM micrograph presented in Figure 5-17 shows, some non-recrystallized regions, which contain smaller precipitates compared to recrystallized areas, are still present. Considering

---

<sup>†</sup>Material for this study has been provided by N. Parson at Rio Tinto Alcan.

high diffusion rates along grain boundaries, the larger precipitates may be either the result of preferential coarsening on moving grain boundaries during recrystallization, or the result of enhanced phase transformation on these boundaries [2]. Characterizing the precipitates located in recrystallized and non-recrystallized areas helps in identifying which of the coarsening or phase transformation mechanism leads to the precipitate size variation. Wang [139] employed EDX analysis to identify the chemical composition of the precipitates in these two regions. The results of that analysis, as presented in Figure 5-32, imply that (large and small) precipitates located in both recrystallized and non-recrystallized areas have the same composition. Wang [139] also conducted detailed analysis on the selected area diffraction patterns taken from particles inside and outside of the recrystallized regions. These analyses have shown that precipitates in both sides are equilibrium Q phase [139]. The above results suggest that no phase transformation occurs on moving grain boundaries, and precipitates located on these boundaries only coarsen due to enhanced diffusion mechanism along the boundaries. It should be mentioned that precipitate coarsening is also accelerated by the dislocations which are located inside the non-recrystallized regions and LAGBs [41-43]. Ardell [41] has shown that the average precipitate size (i.e.  $r$ ) evolution through coarsening obeys a relationship in the form of  $r \propto t^{1/n}$ , where  $n$  varies between 3 and 4 for precipitates located on high and low angle grain boundaries, respectively; while the magnitude of  $n$  is estimated as 5 for precipitates located on a dislocations. In light of the above, although dislocations enhance precipitate coarsening, the effect of grain boundaries is more enhanced, and as a result precipitates in the recrystallized regions are larger. The presence of coarsened precipitates in recrystallized regions suggests that progress of recrystallization is dependent on the precipitate coarsening process. Therefore, it is concluded that movement of the grain

boundary is controlled by the balance of the retarding force of the precipitates (which is reduced by precipitate coarsening) and forwarding force on grain boundary (which originates from the difference of the energy between the deformed and recrystallized regions). A pinned grain boundary can move forward when precipitates coarsen enough to allow the forwarding force overcome the retarding force of precipitates. Through continuation of annealing, a fully recrystallized structure has been achieved. It is seen that by completion of recrystallization in NA-CR-380-20m a more uniform structure with a slightly larger average grain diameter (i.e. 11.4 $\mu$ m) compared to NA-CR-340 condition (i.e. 9.8  $\mu$ m) is obtained.

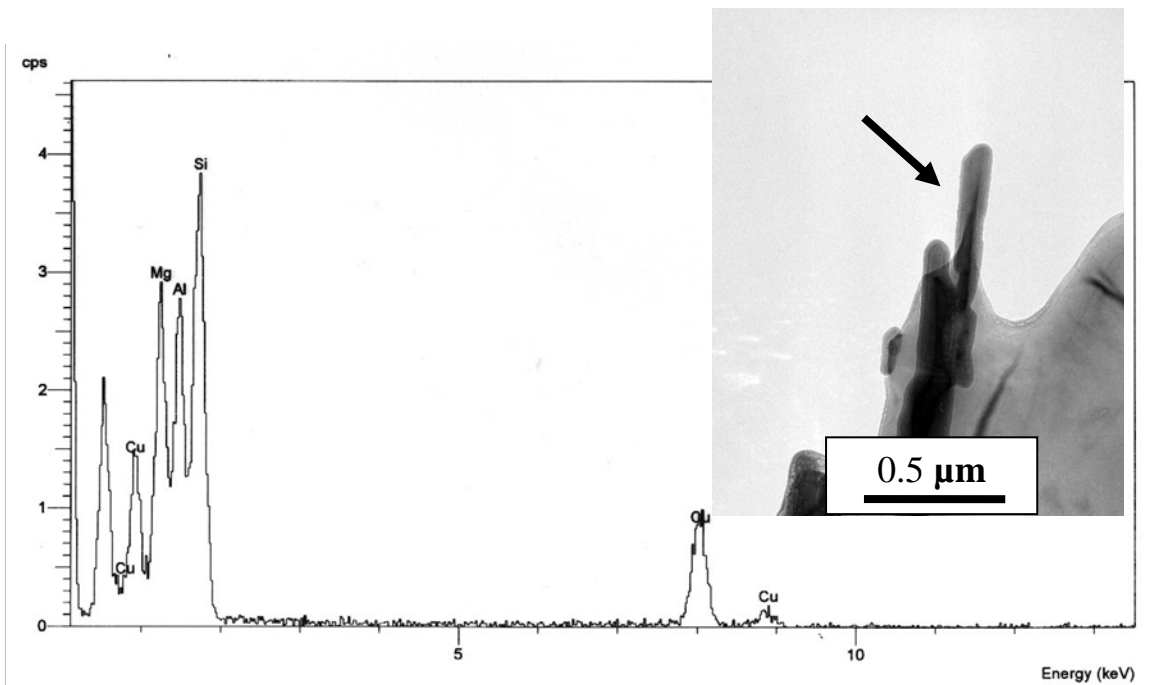
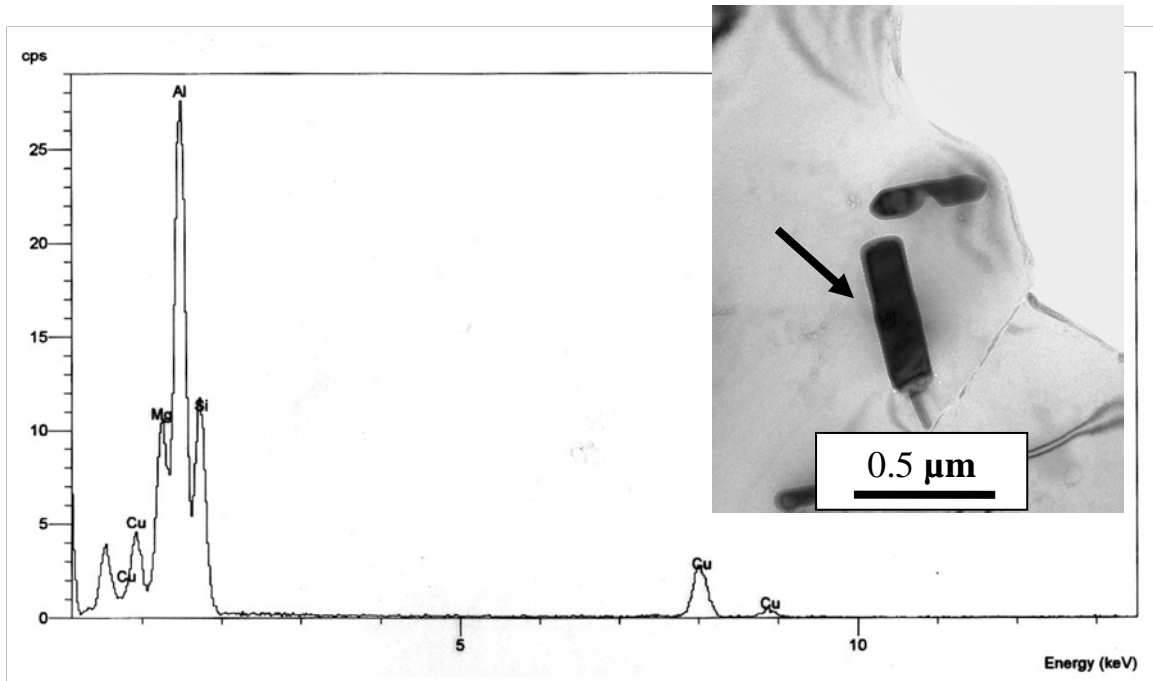


Figure 5-32. EDS analysis on precipitates in a) a recrystallized area and b) a non-recrystallized area of the NA-CR-340-20 [139].

The SEM images in (Figure 5-22) show that even after completion of recrystallization, precipitates interact with grain boundaries and inhibit grain growth. The investigation of the grain size stability during various extended annealing processes has shown the maintenance of the grain size distribution and limited grain growth at high temperature exposure [131]. Although, TEM studies showed that the local precipitate distribution may not be completely uniform due to the interactions of precipitates with dislocation (during deformation and early stages of annealing) and with recrystallization (during later stages of annealing), the overall distribution of precipitates, as reported through Figure 5-21, has been found to be very homogeneous. The uniform distribution of precipitates can be linked to the following reasons:

- 3- homogeneous nucleation of precipitates at low annealing/aging temperature;
- 4- uniform distribution of dislocations which may act as heterogeneous nucleation sites for precipitation;
- 5- growth of the uniformly nucleated precipitates at intermediate stage of annealing and consumption of all solute eliminates tendency of grain boundary (i.e. heterogeneous) precipitation at elevated annealing temperatures.
- 6- In summary, the combination of the above analyses shows that recrystallization progresses in a discontinuous manner through nucleation and growth processes. Due to the large number of uniformly distributed recrystallized nuclei and the high driving force for recrystallization, microstructure evolves uniformly through recrystallization and a fine grained homogenous microstructure forms after completion of recrystallization.

### **5.3.5. Concluding remarks**

In this chapter microstructural evolution in AA6451 alloy during non-isothermal annealing was discussed and interactions between precipitates, dislocations and grain

boundaries were analysed. The acquired knowledge has been used to develop a new computer simulation method for the prediction of microstructural evolution during non-isothermal annealing. The computational modeling technique will be presented in the next chapter.

## **Chapter 6. COMPUTATIONAL MODELLING AND SIMULATION**

The aim of this chapter is to develop a simulation technique for prediction of microstructural evolution in precipitation-hardenable aluminum alloys, where recovery, recrystallization and precipitate coarsening occur concurrently. In the first part of this chapter (Section 6.1) the results of EBSD analysis (Section 5.2.3) are quantified through a Matlab system. In the second part of the chapter (Section 6.2), a Monte Carlo simulation technique for simulating microstructural evolution during isothermal annealing of AA6xxx alloys is developed. The third part (Section 6.3) is devoted to extending the developed simulation technique for simulating the non-isothermal annealing conditions. Finally, the limitation and range of applicability of the developed simulation technique is discussed (Section 6.4).

### **6.1. Computer assisted quantitative analysis of EBSD results**

In order to validate the simulation results which are presented in Section 6.3, quantitative information on recrystallized structure is required. The results, which are provided by HKL Channel 5 software<sup>‡</sup> include combined information on both recrystallized and non-recrystallized areas. Therefore, a Matlab code is generated for quantitative analysis of recrystallized regions in the partly recrystallized samples. This code initially identifies recrystallized areas from non-recrystallized regions in the EBSD maps, and then computes the recrystallized volume fraction and average size of the recrystallized grains. In this section, the details of analysis are described and the quantified EBSD results on the fully- and partially-recrystallized microstructures are presented.

---

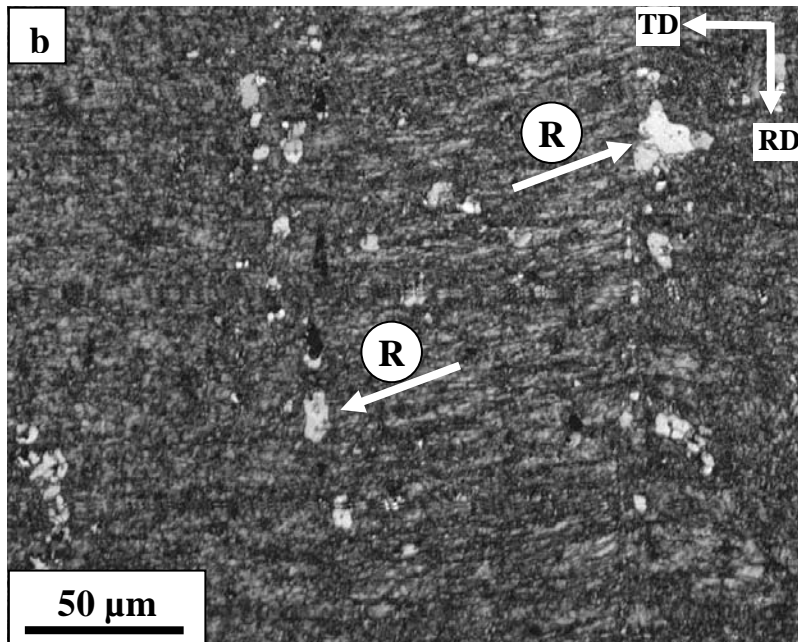
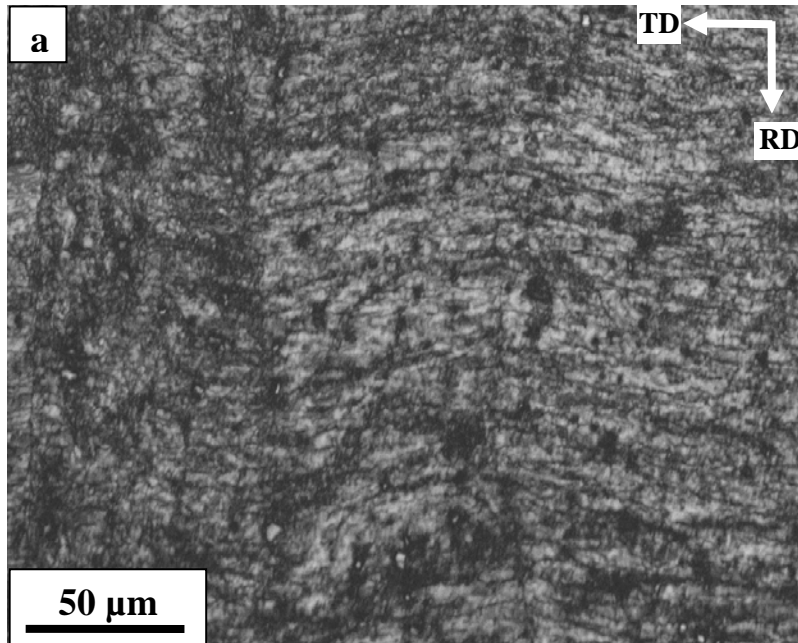
<sup>‡</sup> The software that has been used for EBSD data acquisition.

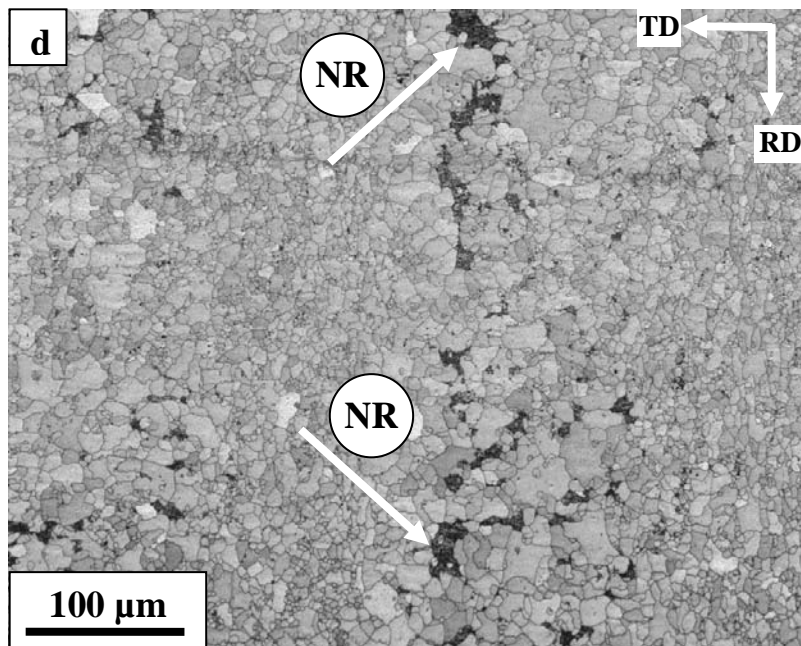
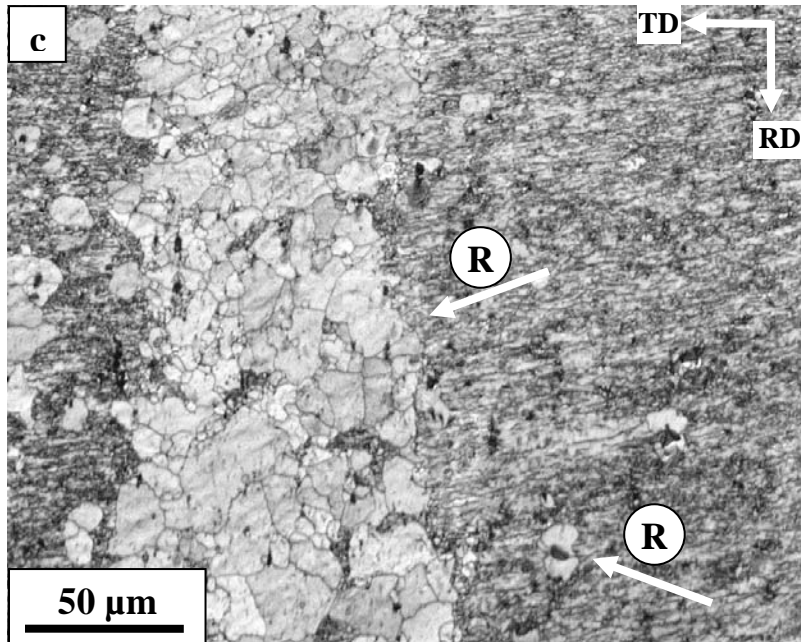
The analysis of recrystallized microstructure using EBSD results is based on different characteristics of the EBSD scans of deformed and recrystallized regions [137, 141, 142]. These differences, therefore, can be used to partition EBSD maps into the deformed and recrystallized regions. There are two main differences between EBSD scans of deformed and recrystallized regions: the indexing quality (IQ) [143-145], and the degree of misorientation [137, 141, 142]. The magnitude of IQ corresponds to the ability of correct indexing of the diffraction pattern which depends on the perfection of the crystal lattice [137]. EBSD analysis reveals relatively low IQ values for grain boundaries and deformed regions. On the other hand, high values of IQ have been detected by EBSD scans of recrystallized regions [137, 143-145]. Several studies have used quantitative differences in IQ to differentiate recrystallized grains from deformed structures (e.g. [143-145]). However, the relative value of IQ is strongly affected by specimen preparation and EBSD scan parameters [141, 143]. Therefore, in order to use IQ values as an individual value for distinction of recrystallized regions, samples with superb surface qualities are required.

The degree of misorientation in a metallic sample corresponds directly to the level of dislocation density [137, 143-145]. The misorientation variation inside grains is represented by Grain Average Misorientation (GAM). GAM values are determined by averaging the misorientation between the neighbouring pixel pairs inside a grain [141]. A high value of GAM indicates a high level of dislocation density, and as a result represents deformed microstructure; whereas the recrystallized grains are characterized by low dislocation content and a corresponding lower value of GAM [137, 141, 142, 146]. The measured orientation, from which the misorientation values are calculated, in contrast to IQ values, are relatively unaffected by surface quality [141, 147]. However, un-indexed points in EBSD

microstructures affect the misorientation values [137], and in turn GAM values. During, EBSD tests, when a lattice site cannot be indexed, its orientation is assigned according to the orientation of its neighbours [137], therefore, a low level of misorientation between the un-indexed lattice and its neighbours exists that results in an estimation of low value of GAM. In the present work, to provide a reliable distinction between recrystallized and non-recrystallized regions, and to overcome the limitation of the use of IQ or GAM as individual criteria, a combination of both parameters is used.

Distribution of the IQ values which have been obtained through EBSD analysis across the scanned area can be visualized by IQ maps. A Matlab code has been generated to construct IQ maps. These maps are constructed by assigning various levels of contrast to different IQ values. The minimum IQ value in the scan is represented by black and the maximum by white, the rest of the gray values are scaled linearly between these two extremes. Figure 6-1 shows IQ maps corresponding to the EBSD results presented in Section 5.2.3. In these IQ maps, recrystallized regions are the areas with light contrast (high IQ values) that are surrounded by dark lines which represent grain boundaries (low IQ values), while non-recrystallized areas are seen by darker contrasts (low IQ values) compared to recrystallized regions. Recrystallized and non-recrystallized regions are marked by (R) and (NR) in the IQ maps of the partly-recrystallized samples (Figure 6-1 (b), (c) and (d)).





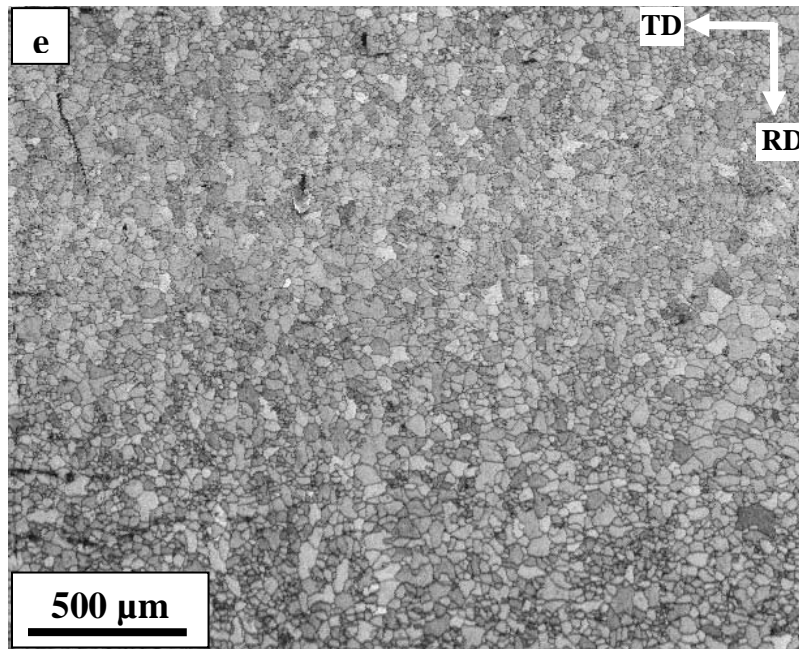


**Figure 6-1. Indexing quality maps generated by Matlab coding based on the measured IQ value for each point of the EBDS maps of a) NA-CR-235, b)NA-CR-300, c)NA-CR-320, d)NA-CR-340 and e)NA-CR-380-20m samples.**

In order to use IQ variation to differentiate recrystallized and non-recrystallized areas, a cut off value is required [143-145]. This cut off value is obtained by comparing the distribution of IQ values in deformed and recrystallized microstructure [143]. The population of IQ values for ideal fully recrystallized and completely deformed samples, is presented in the schematic graph of Figure 6-2. For this ideal case, there is no intersection between the two graphs and the IQ\_limit shown in the figure can be considered as the cut off value: when IQ is higher than the IQ\_limit, the measured point is considered to be recrystallized, whereas when IQ is lower than the IQ\_limit the associated point is considered to be non-recrystallized. However, the distribution shown in Figure 6-2 is rarely observed through real experimental analysis [143], as there are always some regions with low IQ values in the fully recrystallized

samples and some regions with high values of IQ in the deformed sample. Therefore, usually the two curves intersect and a common area exists between them. Such a condition has been observed when the population of IQ values for the two extreme cases of NA-CR-235 and NA-CR-380-20m are plotted, as shown in Figure 6-3. This plot shows that, in general, higher IQ values correspond to the NA-CR-380-20m sample as compared to the NA-CR-235 sample. The two distribution plots intersect at  $IQ_{cr}$  and a common area is observed between the two curves. The common area in Figure 6-3 is divided into two sections: LI and HI. The low IQ values of NA-CR-380-20m in the LI region correspond to those parts of the sample which have relatively lower IQ values including grain boundaries and regions with poor surface quality. Considering the IQ Map in Figure 6-1(a), the high IQ values in region HI cannot necessarily be considered as recrystallized areas, since a qualitative analysis on Figure 6-1(a) shows that the area fraction of recrystallized grains should be very small. Therefore, area HI, is concluded to be arisen from those pixels which have high levels of IQ, but cannot be considered as recrystallized grains. These areas might be dislocation free-regions with are not surrounded by high angle grain boundaries (such as subgrains) or areas which contain small amount of dislocations. Based on the above analysis,  $IQ_{cr}$  is considered as the IQ limit, but for the correct isolation of recrystallized grains, the grain average misorientation, i.e. GAM, is also taken into account as an additional criterion.

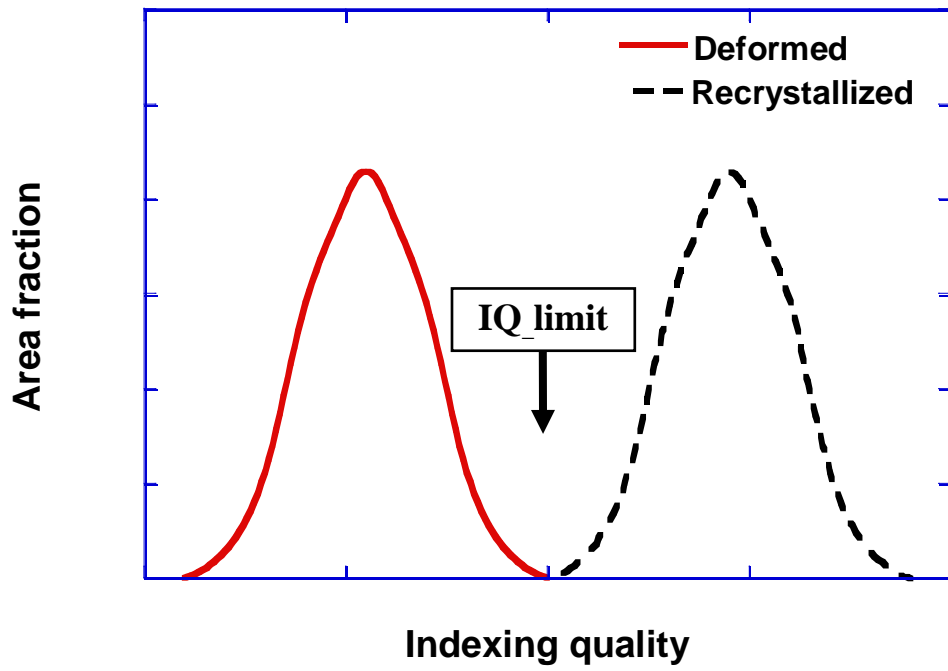


Figure 6-2. The schematic distribution of indexing quality for ideal recrystallized and deformed samples.

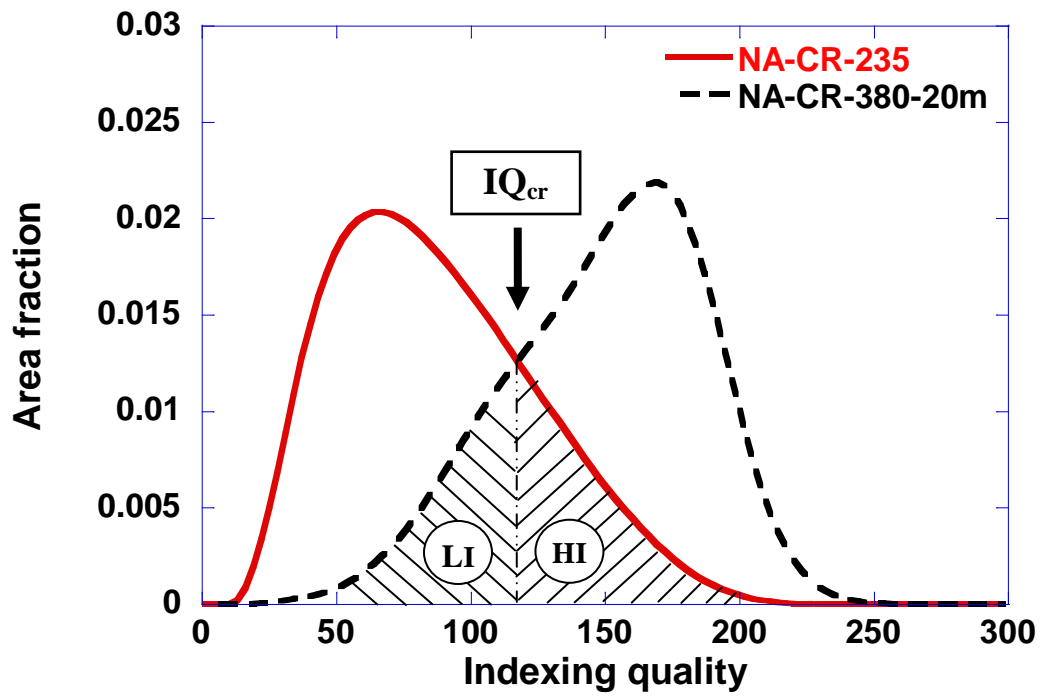


Figure 6-3. Distribution of indexing quality values for NA-CR-235 and NA-CR-380-20m.

To calculate GAM values, initially the misorientations of neighbouring pixels pairs are calculated based on the technique described in Appendix . Consequently, GAM values for the regions surrounded by high angle grain boundaries are computed through a Matlab code. Population of GAM values for NA-CR-235 and NA-CR-380-20m are plotted in Figure 6-3. The low values of GAM in the NA-CR-380-20m sample correspond to the large fraction of recrystallized structure in this annealing condition. Similar to the IQ graph, a common area is observed between two curves. This area is divided into two regions: HG and LG. The HG region corresponds to grain boundary areas and any remaining non-recrystallized regions in the NA-CR-380-20m sample. Considering that the fraction of recrystallized areas in the NA-CR-235 sample should be very small, the LG region is concluded to be mainly associated with the un-indexed lattice sites in the EBSD map of NA-CR-235 sample. As the IQ value of un-indexed sites is very small, these lattice sites can be distinguished from the real recrystallized sites, by considering their IQ value. By this consideration, the part of the LG region which does not correspond to recrystallized sites is eliminated, and the intersecting point between the two curves of Figure 6-4, i.e.  $GAM_{cr}$ , is considered as the GAM limit for distinction of recrystallized regions from non-recrystallized regions.

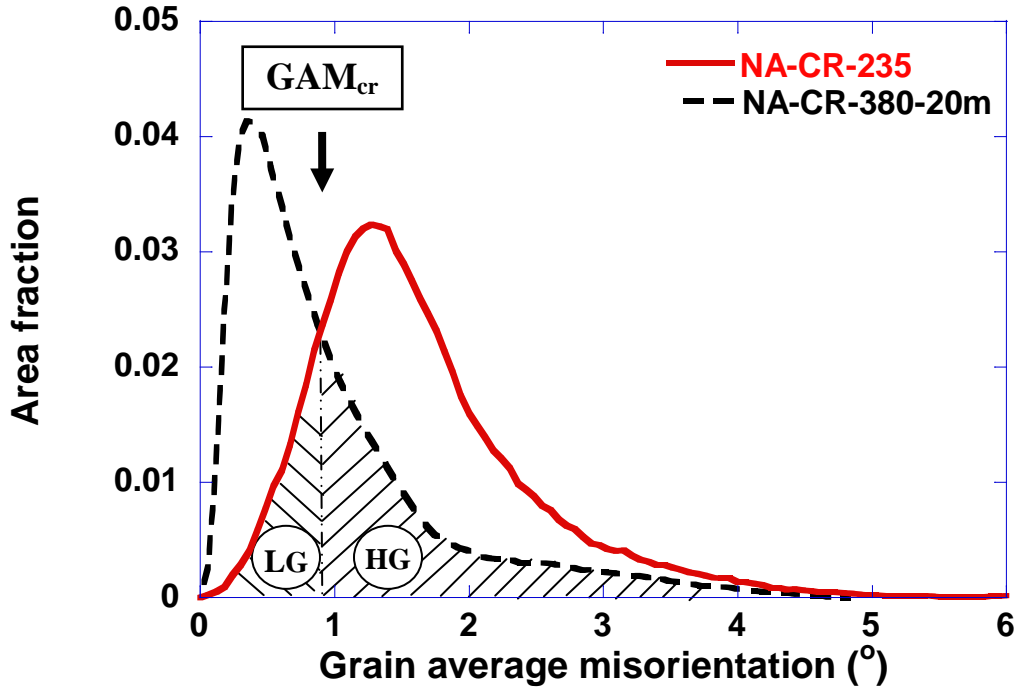


Figure 6-4. Distribution of grain average misorientation values for NA-CR-235 and NA-CR-380-20m.

In addition to the criteria defined by  $GAM_{cr}$  and  $IQ_{cr}$ , a recrystallized grain should be surrounded by grain boundaries and be larger than a specific size [137]. Considering the above analysis on IQ and GAM, in present research, the criteria for a region to be considered as a recrystallized grain are set as follows:

- 1- the average image quality of the surrounded region should be larger than a defined limit,  $IQ_{cr}$ ;
- 2- the average misorientation inside the surrounded region should be smaller than a defined misorientation limit,  $GAM_{cr}$ ;
- 3- the region should be surrounded by boundaries above a certain angle,  $\theta_{cr}$ ;
- 4- the average equivalent diameter of the surrounded region should be larger than a defined size limit,  $d_{cr}$ .

To be consistent with the experimental setup explained in Section 4.3.5,  $\theta_{cr}$  is defined as  $7.5^\circ$ . Similarly, considering TEM observation,  $d_{cr}$  is designated as  $1\mu\text{m}$ . The  $\text{GAM}_{cr}$  and  $\text{IQ}_{cr}$  are defined as  $0.9^\circ$  and 118, respectively through the results presented in Figure 6-3 and Figure 6-4. Based on these criteria, a Matlab programming system has been developed for identifying recrystallized grains and calculating recrystallized fraction as well as the equivalent average diameter of the recrystallized grains. Considering the corresponding low IQ and high GAM values of grain boundaries, grain boundaries would be considered as non-recrystallized regions in the programming system which would affect calculation of recrystallized fraction. To eliminate this effect, it is assumed that the microstructure consists of recrystallized, non-recrystallized and grain boundary areas. Therefore, the summation of recrystallized area fraction,  $f_{rex}$ , non-recrystallized area fraction,  $f_{non-rex}$ , and grain boundaries area fraction,  $f_{gb}$  equals unity as given by:

$$f_{rex} + f_{non-rex} + f_{gb} = 1 \quad (6-1)$$

To confirm accuracy of the calculation, average diameter and size distribution of recrystallized grains for the fully recrystallized condition (i.e. NA-CR-380-20m) is calculated and compared with the same results obtained using Channel 5 software. Considering that, for the NA-CR-380-20m sample most of the grains are recrystallized, a good agreement between computed and EBSD results is expected. The average computed grain size is  $11.04\mu\text{m}$  which agrees well with the Channel 5 calculations, i.e.  $11.44\mu\text{m}$ . For further examination, the distribution of grain sizes, obtained from computed results are compared with that of Channel 5 software. The comparison of size distribution is provided in Figure 6-5.

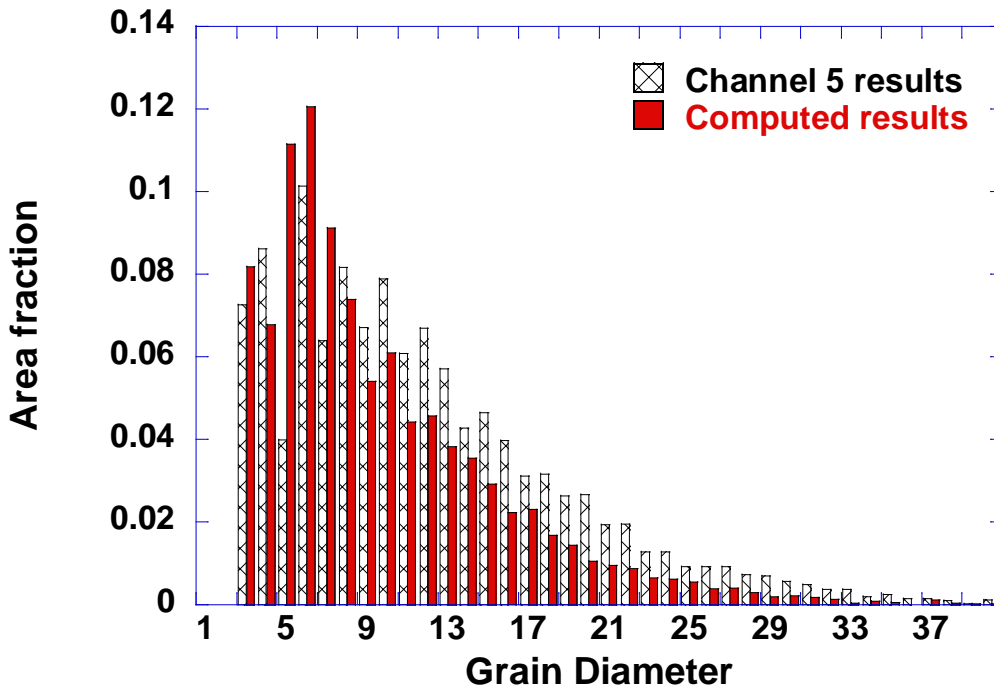
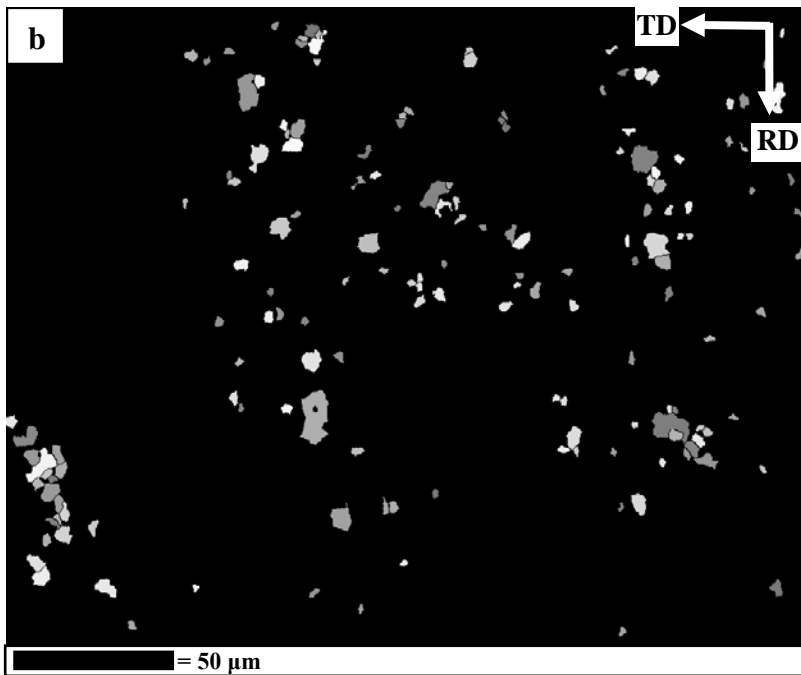
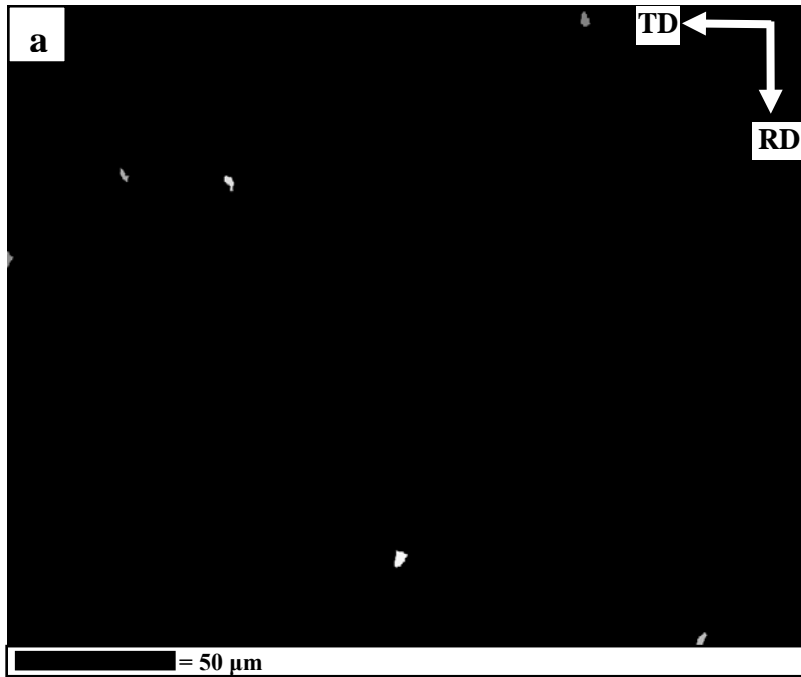
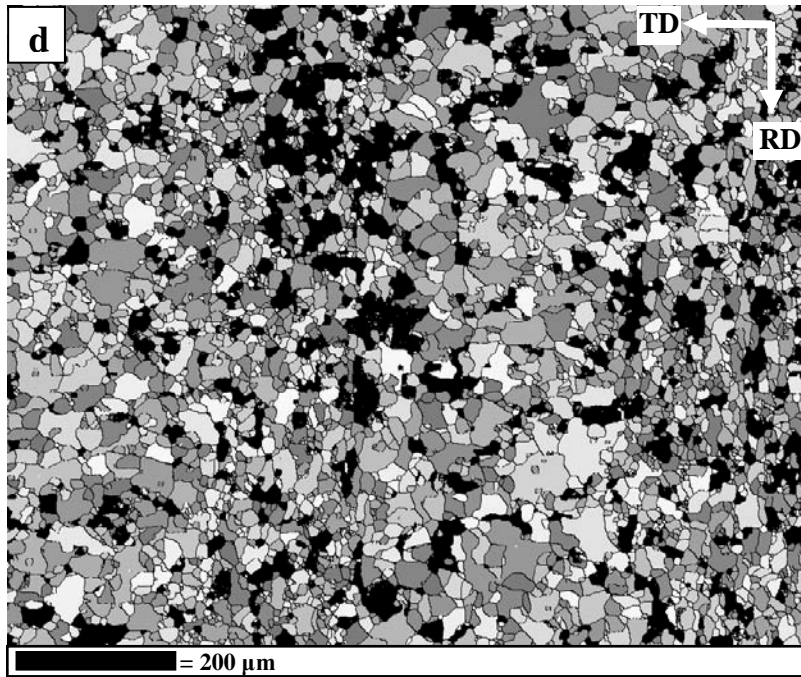
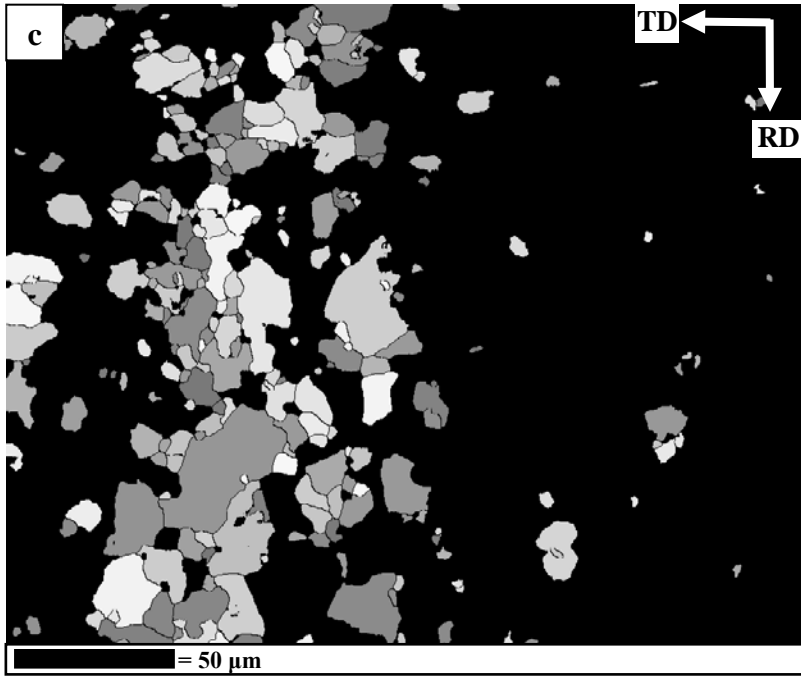


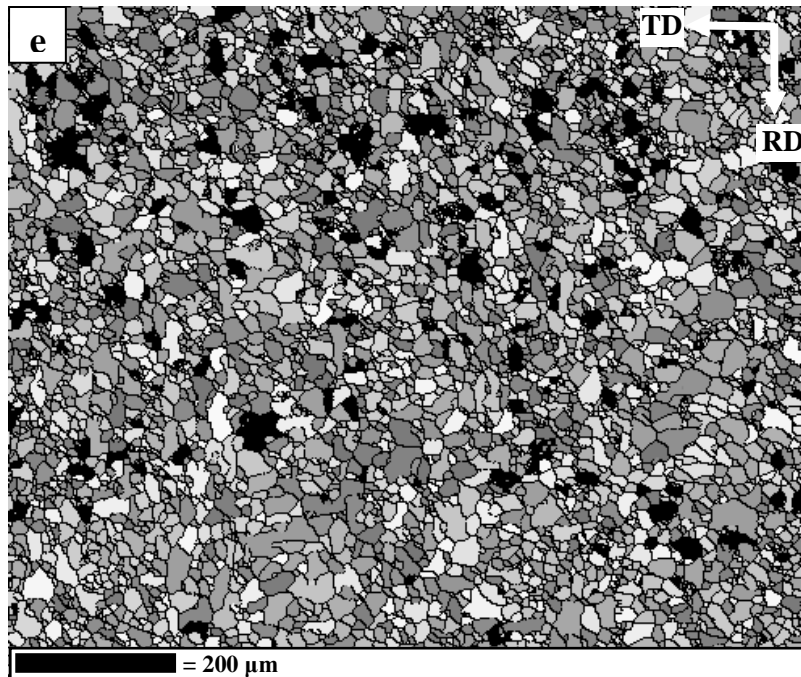
Figure 6-5. Grain size distribution in NA-CR-380-20m; comparison of Channel 5 analysis results and computed results.

Figure 6-5 shows a good agreement between the computed results and Channel 5 calculations. The slight difference between the two sets of data is due to the fact that the computed results are restricted to the size of recrystallized grains while Channel 5 results are calculated for all of the grains (recrystallized and non-recrystallized). The observed agreement validates the technique developed for calculation of recrystallized grain size.

The computed results are provided in Figure 6-6 as recrystallized grains maps. In these maps, recrystallized grains appear in different gray contrasts while non-recrystallized (i.e. deformed) areas appear in black shade. Due to the clear distinction between recrystallized and non-recrystallized areas in the recrystallized grains maps, the very small recrystallized grains, which are not clearly observable in EBSD maps of Figure 5-23 or Figure 5-24, are visible in these figures.







**Figure 6-6. Recrystallized grains maps of a)NA-CR-235, b) NA-CR-300, c) NA-CR-320, d) NA-CR-340, and e) NA-CR-380-20m; non-recrystallized areas are shown in black shade.**

To obtain a quantitative analysis of the evolution of grain size during annealing, the average diameters of recrystallized grains for each annealing condition have been calculated. The quantified results are plotted in Figure 6-7. The computed results have been also used to calculate recrystallized area fraction as a function of annealing temperature. Comparing Figure 6-7 and Figure 6-8, it is seen that grain size and volume fraction evolution show similar trends with the increase in temperature.

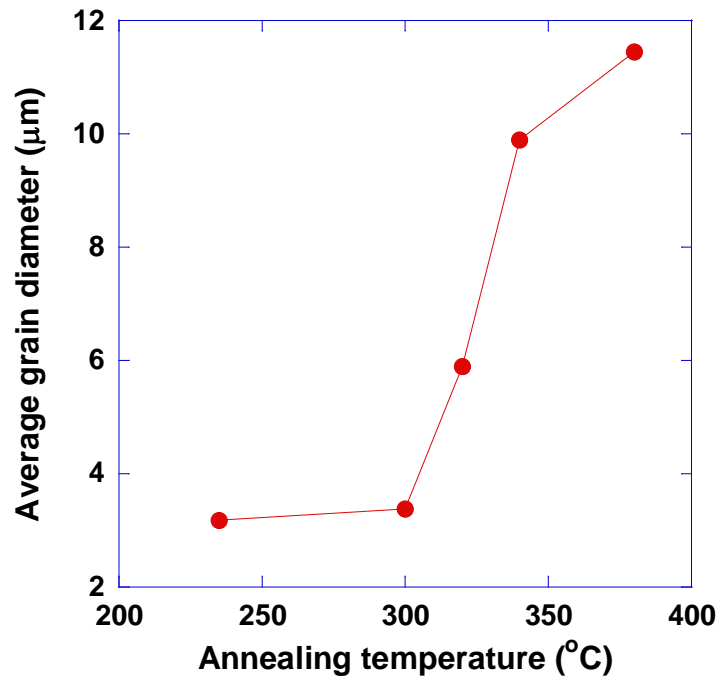


Figure 6-7. Quantified EBSD results showing the evolution of average grain diameter as a function of the end temperature of the non-isothermal annealing process.

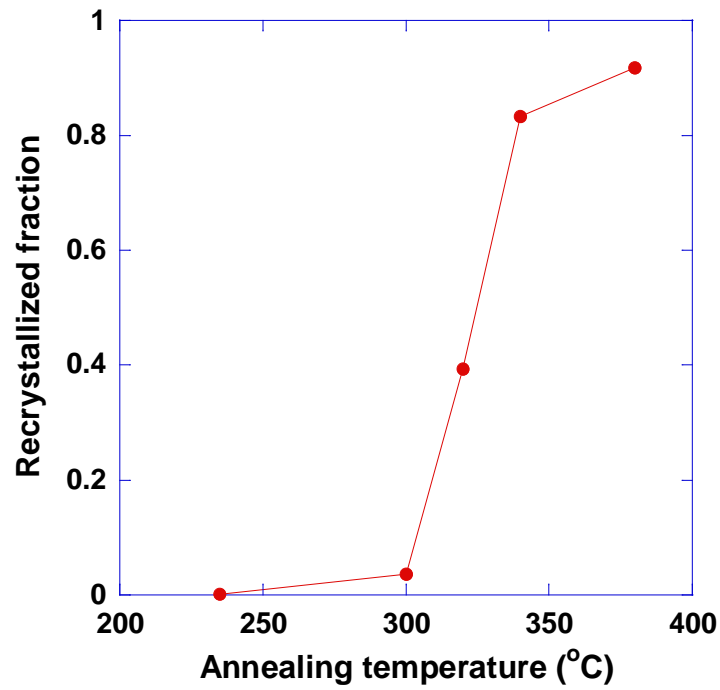


Figure 6-8. Quantified EBSD results showing the evolution of recrystallized fraction as a function of the end temperature of the non-isothermal annealing process.

The quantified EBSD results presented in Figure 6-7 and Figure 6-8 will be used to validate the simulation results in Section 6.3. It should be noted that the quantified EBSD results strongly depend on the criteria which have been considered for identifying recrystallized and non-recrystallized regions. Although these criteria are assigned based on accepted physical concepts, the magnitude of  $IQ_{cr}$  and  $GAM_{cr}$  are affected by the quality of the EBSD scan, which in, turn, is dictated by parameters (e.g. surface quality) which have not been considered in the computation technique. As extra care has been taken in EBSD sample preparation and conducting the EBSD tests, the contribution of these effects, and in turn, levels of errors in the quantified results are considered to be minor.

## **6.2. Simulating isothermal annealing**

This section (i.e. Section 6.2) is identical to the published paper: Sepehrband, P., Esmaili, S., “A methodology for Monte Carlo simulation of recrystallization in an overaged and cold rolled precipitation-hardenable aluminum alloy,” *Scripta Materialia*, Vol. 63, 2009, pp.4-7 [148]. To make this section consistent with the other parts of the thesis, subtitles have been added to the original text of the paper and numbering of figures, tables, equations and references are updated. The additional information which has been provided for clarity is isolated between double parallel lines and separated from the main text. Abstract and acknowledgement of the paper are not included in this section. At the end of the section, the flowchart of simulation, which has not been included in the paper, is provided.

### 6.2.1. Introduction

AA6xxx aluminum alloys are the alloys of choice in the automotive industry for lightweight skin panel applications. The use of these alloys is expected to rise in coming years due to the ever increasing need for significant weight reduction in automobile manufacturing. The widespread applications of these alloys, however, will require further research and development activities in various areas related to the processing, process optimization and properties of the alloys. One such area involves developing novel thermomechanical processing (TMP) methods to achieve fine-grained sheets with superior high temperature deformation behaviour [1, 8, 16]. Optimization of processes and sheet characteristics requires development of physically-based models to predict microstructural evolution during processing of the alloys. The microstructural characteristics of AA6xxx alloys following TMP are dictated by a complex series of interactions between various microstructural inhomogeneities (i.e. deformation induced inhomogeneities and pre-existing intermetallic particles), precipitates, and annealing phenomena [6, 8, 16, 92, 131]. Currently, no physically-based model or effective computer simulation methodology is available for predicting the microstructural evolution during annealing of these alloys. This work is the first stage of developing a comprehensive model, based on a combination of analytical and computational approaches, to predict the multi-variable nature of microstructural evolution in thermomechanically-processed AA6xxx alloys. The Monte Carlo technique, which has previously been used for the simulation of recrystallization in less complex systems (e.g. in [7-9]), is utilized for the computational work.

### **6.2.2. Objective**

The objective of the present work is to model microstructural evolution of an overaged and deformed AA6111 aluminum alloy during annealing.

### **6.2.3. Analytical formulation**

The microstructure at the start of annealing includes (a) particles which pre-existed the aging process (i.e. large particles), and (b) precipitates which formed during overaging of the alloy. The large particles, which accumulate significant energy during the deformation process, can act as the favourable sites for the nucleation of new recrystallized grains during annealing treatment (i.e. particle stimulated nucleation, PSN) [3]. The role of precipitates, which undergo coarsening during annealing, is interfering with the annealing phenomena through pinning dislocations and grain boundaries (i.e. inhibiting recovery and growth during recrystallization, respectively). The equations governing these phenomena are listed in Table 6-1. As shown in the table, the accumulated stored energy is related to dislocation density [3, 60], while the recovery of the stored energy is assumed to be due to thermally activated glide and cross slip [86, 94, 95]. The equations, originally developed for less complex systems, are advanced in this work to consider both the effects of large particles on the energy storage and precipitate coarsening on the recovery process.

Table 6-1. Analytical equations

Phenomena	Equations	Ref.	Comments
Dislocation accumulation	$\rho_t = \rho_l + \rho_g$	(6-2)	* $\rho_t$ : total dislocation density; $\rho_l$ : dislocation density around large particles; $\rho_g$ : dislocation density in the grains
	$\rho_t = \left(\frac{\sigma_{dis0}}{0.5Gb}\right)^2$	(6-3)	[60] $\sigma_{dis0}$ : dislocation contribution to yield strength at the start of annealing; $G$ : shear modulus of aluminum $b$ : magnitude of Burgers vector
	$\rho_t = \frac{6f_l\varepsilon}{d_l b}$	(6-4)	[62] $f_l$ : volume fraction of large particles; [63] $d_l$ : averaged diameter of large particles; $\varepsilon$ : true strain of deformation
Stored energy accumulation	$H = 0.5\rho Gb^2$	(6-5)	[3] $H$ : stored energy of deformation
	$H_{0g} = 0.5\rho_g Gb^2$	(6-6)	* $H_{0g}$ : stored energy inside the grains;
	$H_{0l} = 0.5\rho_l Gb^2$	(6-7)	* $H_{0l}$ : stored energy around large particles

Phenomena	Equations	Ref.	Comments
Release of stored energy due to Recovery	$\sigma_d(t, T) = \sigma_{d0} - \frac{kT}{V_r} \ln \left( 1 + \frac{t}{t_1} \right) \quad (6-8)$	[86] [94] [95]	$T$ : annealing temperature; $t$ : annealing time; $t_1$ : reference time ; $k$ : Boltzmann's constant; $V_r$ : activation volume of recovery
	$H(t, T) = \left[ H_0^{1/2} - \frac{kT}{0.5^{1/2} G^{1/2} \theta_D} \ln \left( 1 + \frac{t}{t_1} \right) \left( 1 - \frac{N_{ppt}(t, T)}{0.5 \rho(t, T)^{3/2}} \right) \right]^2 \quad (6-9)$	†	$H_0$ : stored energy at the start of annealing; $N_{ppt}$ : number density of precipitates
Precipitate Coarsening	$N_p(t, T) = \frac{f_{ppt}}{4/3 \pi r_{ppt}(t, T)^3} \quad (6-10)$	*	$r_{ppt}$ : average radius of precipitates; $f_{ppt}$ : volume fraction of precipitates
	$r_{ppt}(t, T)^3 - r_0^3 = k_c(t - t_0) \quad (6-11)$	[31]	$r_0$ : radius of precipitates at $t_0$ , the start of annealing $k_c$ : rate constant

\* Formulation defined in this work.

† Equation (6-9) is formulated to define the evolution of stored energy in a precipitate containing system. This equation is derived by rewriting Equation (6-8) for stored energy and including the pinning affect of precipitates on dislocations. It is assumed that in precipitate-containing microstructures, recovery is restricted to a portion of the structure equal to  $\left(1 - \frac{N_{ppt}}{0.5 \rho^{3/2}}\right)$ . A similar approach was previously used by Zurob et al. [5] to model the evolution of yield strength during recovery of a precipitation hardenable system.

---



---

Derivation of Equation (6-9):

As explained in Section 2.2.2.1, the evolution of  $\sigma_{dis}$  during annealing through recovery is formulated as [86, 94, 95]:

$$\sigma_{dis}(t, T) = \sigma_{dis0} - \frac{kT}{V_r} \ln \left( 1 + \frac{t}{t_1} \right) \quad (6-12)$$

where  $t_1$  is a reference time given by [86]:

$$t_1 = \frac{kT}{K_1 V_r} \exp((U_r - V_r \sigma_{dis0})/kT) \quad (6-13)$$

where  $U_r$  is the activation energy for recovery and  $K_1$  has been treated as a constant. Parameter  $K_1$  can be calculated by comparing the original equation of recovery which has been developed by Friedel [95] (Equation (6-14) ) and the derivation of the recovery equation by Verdier et al. [86] (Equation (6-15)).

$$\frac{d\sigma}{dt} = -K_1 \exp \left( -\frac{U_r - V_r \sigma_{dis}}{kT} \right) \quad (6-14)$$

$$\frac{d\sigma}{dt} = -\frac{E\rho b^2 v_D}{M} \exp \left( -\frac{U_r}{kT} \right) \sinh \left( \frac{\sigma_{dis} V_r}{kT} \right) \quad (6-15)$$

By combining Equation (6-14) and (6-15),  $K_1$  is formulated as:

$$K_1 = \frac{E\rho b^2 v_D \exp \left( -\frac{U_r}{kT} \right) \sinh \left( \frac{\sigma_{dis} V_r}{kT} \right)}{M \exp \left( -\frac{U_r - V_r \sigma}{kT} \right)} \quad (6-16)$$

where  $E$  is the Young's modulus and  $v_D$  is the Debye frequency. Using Equation (6-3) and Equation (6-5),  $\sigma_{dis0}$  is related to  $H$  through Equation (6-17).

$$\sigma_{dis0} = (0.5GH_0)^{1/2} \quad (6-17)$$

Replacing  $\sigma_{dis0}$  in Equation (6-8), the changes of the stored energy with annealing time can be formulated. As a new addition in the present work, the pinning effect of the precipitates against recovery, originally introduced by Zurob et al. [5] in defining the evolution of yield stress during annealing (Equation (2-18)), is also included in the stored energy relationship. This gives a new relationship to define the evolution of stored energy,  $H$ , in a precipitate containing system:

$$H(t, T) = \left[ H_0^{1/2} - \frac{kT}{0.5^{1/2} G^{1/2} v_D} \ln \left( 1 + \frac{t}{t_1} \right) \right]^2 \left( 1 - \frac{N_{ppt}(t, T)}{0.5 \rho(t, T)^{3/2}} \right) \quad (6-9)$$


---



---

## 6.2.4. Simulation algorithm for isothermal annealing conditions

### 6.2.4.1 Generation of deformed structure

The Monte Carlo simulation algorithm is built based on the competition between recovery and recrystallization for reduction of the stored energy in the system. As the first step of the simulation, the deformed structure is generated from the non-deformed grain structure. To generate the deformed grains, as a first order approximation, the undeformed grain structure reported in [6] is elongated along the rolling direction according to the total level of deformation, and assuming plane strain and constant volume conditions. The deformed grain structure is mapped into a 240x200 square lattice of 240x200  $\mu\text{m}^2$  where, lattice sites located in each grain are given an arbitrary number, i.e.  $S$  [8]. Large intermetallic particles are, then, randomly added to the mapped structure. Number density and size of the particles are treated as calibration parameters which are characteristics of the non-deformed microstructure. As precipitates are too small for running the simulation in a reasonable time, the microstructure map does not include precipitate locations. Instead, the presence of a

uniform distribution of precipitates is indirectly included through the analytical formulation of their pinning effect against recovery and grain boundary movement.

The calculated stored energy from Equation (6-6) in Table 6-1 is distributed in the microstructure: inside the grains [124] and around large particles [3]. The energy of lattice sites located inside the grains is defined using a second degree polynomial function. Within each grain, stored energy decreases from its highest value, i.e.  $H_{0g}^{\max}$ , at the grain boundary to

its lowest value, i.e.  $H_{0g}^{\min}$ , at the centre of the grain. The ratio of  $\frac{H_{0g}^{\max}}{H_{0g}^{\min}}$  is assumed to be

equal to the ratio of  $\frac{\gamma}{\gamma_{\theta}}$ , where  $\gamma$  is the high angle grain boundary energy, and  $\gamma_{\theta}$  is the energy

of low angle grain boundaries at the center of the grain. The stored energy of each lattice site of the grain, i.e.  $H_{0g-i}$ , is, then, assigned according to the location of the site in the grain and

considering  $\sum_{i=1}^N H_{0g-i} = H_{0g}$ , where  $N$  is the total number of the lattice sites. This approach

results in the energy distribution profile as presented in Figure 6-9 for a single grain. As the profile demonstrates, distribution of stored energy agrees with typical experimental observations [3]; i.e. the concentration of stored energy at the grain boundary area and almost same level of stored energy in the rest of the grain. The extra stored energy around the large particle is added according to the technique described in [12] and the stored energy calculated from Equation (6-7) in Table 6-1.

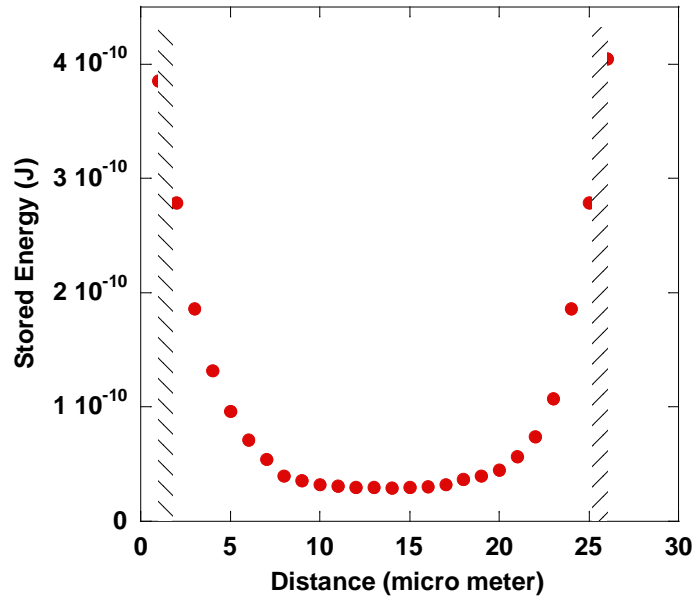


**Figure 6-9. Stored energy distribution across a deformed grain; the hatched rectangles show areas having the highest 10% of stored energy.**

#### 6.2.4.2 Simulating microstructural evolution

The next step is modeling microstructural evolution of the deformed structure. For this purpose, it is assumed that nucleation of recrystallization occurs entirely at the onset of annealing based on the site-saturated nucleation mechanism [3]. In the current work, the number of recrystallization nuclei per unit volume,  $N_{rex}$ , is considered as a calibration parameter, which is obtained from the experimentally-acquired number of grains in the fully-recrystallized microstructure. The recrystallized nuclei are added to the structure by the selection of  $N_{rex}$  sites. Selection has been drawn from those sites that have the highest 10% of stored energy, giving a higher chance to the sites with larger levels of stored energy by considering a weight factor. The areas having the highest 10% of stored energy for a sample grain are shown by the hatched rectangles in Figure 6-9. It should be noted that based on early simulation trials, this level of energy (the highest 10%) has been found to be close to an

optimum level for leading to a realistic distribution of nuclei. The stored energy of the selected sites is subsequently reset to zero and the recrystallization process is simulated by the growth of the assigned recrystallized nuclei.

To integrate the effect of recovery and precipitate coarsening on recrystallization in the Monte Carlo algorithm, the simulation should be run as a function of real annealing time. Therefore, a viable method is required to relate Monte Carlo time to real time. To do so, a defined time duration (i.e.  $t_{cycle}$ ) is assigned to each Monte Carlo cycle and annealing time is considered as the summation of the assigned time durations of successive Monte Carlo cycles. Assuming that grain boundary displacements at a small scale (i.e. one lattice site) have a linear relationship with velocity,  $t_{cycle}$  for each Monte Carlo cycle may be found through the following equation:

$$L = v_{max}(t, T)t_{cycle}(t, T) \quad (6-18)$$

where  $L$  is the length swept by high angle boundaries during one lattice site growth and  $v_{max}(t, T)$  is the velocity of the fastest moving boundary in the microstructure. The parameter  $v_{max}(t, T)$  can be related to the highest pressure on a lattice site of the microstructure, i.e.  $P_{max}(t, T)$  and grain boundary mobility, i.e.  $M_b(T)$ , as defined by [3]:

$$v_{max}(t, T) = P_{max}(t, T)M_b(T) \quad (6-19)$$

The parameter  $P_{max}(t, T)$  in the above equation is calculated as  $P_{max}(t, T) = H_{max}(t, T) - Z(t, T)$ , where  $H_{max}(t, T)$  is the highest stored energy in the structure and  $Z(t, T)$  is the pinning effect of precipitates against grain boundary movement. The parameter  $Z(t, T)$  is related to the volume fraction of precipitates,  $f_{ppt}$ , and their average radius,  $r_p$ , given by  $Z(t, T) = 3f_{ppt}\gamma/2r_p(t, T)$ [115].

Employing  $t_{\text{cycle}}$ , the analytical equations of recovery, the pinning effect of precipitates, as well as precipitate coarsening are included in the Monte Carlo simulation. In each Monte Carlo cycle, the driving force for growth of recrystallized lattice sites is considered as the difference between the stored energy of the adjacent deformed and the recrystallized sites. To simulate microstructural evolution, one lattice site is selected in a random manner. If the selected site is recrystallized, it may grow by reorientation of its neighbour that has the highest amount of stored energy. The possibility of reorientation is, then, verified thermodynamically and kinetically. To check if reorientation is thermodynamically possible, total energy of the system before and after reorientation,  $E_1$  and  $E_2$  respectively, are calculated through the following equation [9]:

$$E_{\text{total}}(t, T) = \sum_{i=1}^N H_i(t, T) + \frac{1}{2} \sum_{i=1}^N \sum_{j=1}^{N_n} \gamma(1 - \delta_{i,j}) \quad (6-20)$$

In this equation,  $\delta_{ij}$  is the Kronecker delta function that is zero if  $S_i \neq S_j$  and unity if  $S_i = S_j$ . The sum on  $i$  is over all  $N$  sites in the system and the sum on  $j$  is over the  $N_n$  nearest neighbours of site  $i$ . Reorientation of the selected neighbour is thermodynamically accepted if it is energetically favourable and the pinning effect of precipitates can be overcome, as defined in Equation (6-21).

$$E_2(t, T) \leq E_1(t, T) - Z(t, T) \quad (6-21)$$

To verify if one lattice site movement is kinetically possible, initially, the distance that the selected recrystallized site can move, i.e.  $X_{\text{local}}(t, T)$ , is calculated. For such calculation, it is assumed that the local pressure on the boundary is the balance between the stored energy of the selected site and pinning pressure of precipitates, i.e.  $H_i(t, T) - Z(t, T)$ . Then,  $X_{\text{local}}$  is

related to the local pressure, grain boundary mobility, and the annealing time of the selected site, i.e.  $t_i(t,T)$ , as defined in Equation (6-22):

$$X_{local}(t,T) = M_b(T)[H_i(t,T) - Z(t,T)]t_i(t,T) \quad (6-22)$$

Annealing time of the selected site, i.e.  $t_i$ , is the summation of  $t_{cycle}$  of previous MC cycles during which the selected site has experienced unsuccessful reorientation attempts. If the calculated distance is larger than one lattice site, as defined in Equation (6-23), then reorientation is kinetically possible.

$$X_{local}(t,T) \geq L \quad (6-23)$$

If either of Equation (6-21) or Equation (6-23) is not satisfied or if the selected site is not recrystallized, reorientation is not allowed and the chosen site will undergo recovery, where its stored energy is decreased through Equation (6-7). Monte Carlo algorithm is repeated till the stored energy due to deformation (i.e. the rolling process) is completely released and the entire microstructure recrystallized.

### 6.2.5. Calibration and implementation of simulation

To verify the validity of the model, it is implemented for predicting microstructural evolution of an overaged and cold-rolled AA6111 aluminum alloy during annealing at 325°C, for which published experimental data is available [6]. The thermomechanical route consists of aging the alloy for seven days at 325°C and then cold rolling for a total 40% reduction in thickness. The calibration parameters for the model implementation are summarized in Table 6-2. Figure 6-10 demonstrates three successive images from the simulation results (i.e. Improved-MC). In Figure 6-10 (a), it is seen that recrystallization nuclei are formed at grain boundaries, particularly at triple junctions, and around large particles as a result of particle stimulated nucleation (PSN). However, it is noticed that not the entire set of particles act as PSN sites

and nucleation preferably initiates at those particles which are located close to grain boundaries. This kind of nucleation is linked to the compensation of the low PSN efficiency of particles by the extra stored energy at the grain boundaries. The low PSN efficiency is due to the relatively low level of deformation and/or small sizes of particles [3]. Preferential PSN close to grain boundaries is in agreement with experimental studies on particle containing microstructures [3, 151]. As shown in Figure 6-10, by continuing annealing, a directional growth of recrystallized nuclei along the rolling direction occurs, which produces a non-equiaxed grain structure. Such a growth mechanism in the simulated microstructure is due to preferential growth of recrystallized sites toward high energy sites of the mapped structure through selection of high energy neighbours of recrystallized sites during reorientation attempts. The results are consistent with the experimentally acquired image reported in Ref. [6].

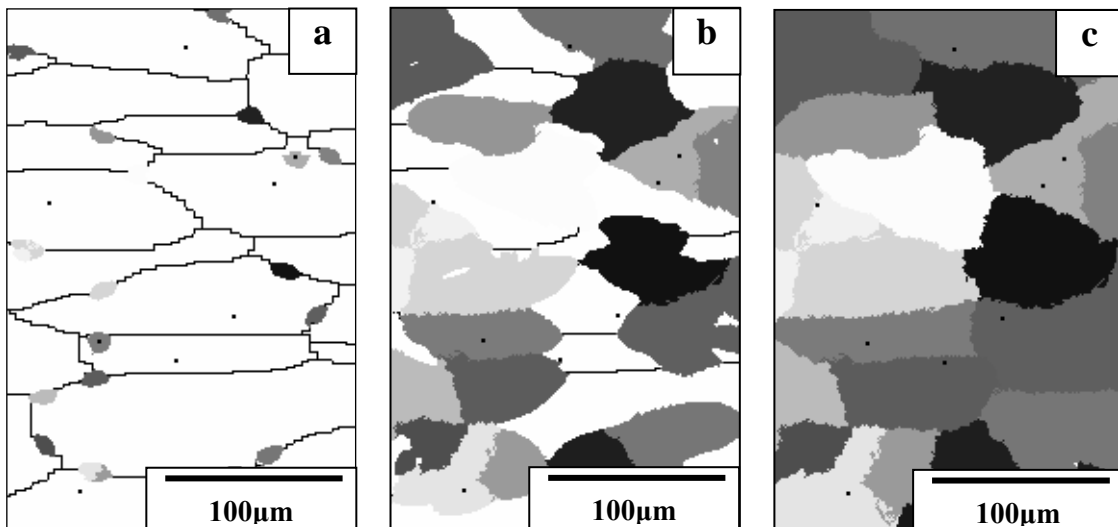


**Figure 6-10.** MC simulation of microstructural evolution during annealing at 325°C for a) 35 h, b) 165 h, and c) 600h.

**Table 6-2. Calibration parameters for model implementation**

<b>Parameter</b>	<b>Value</b>	<b>Derivation and Sources</b>
$A$	$8 \times 10^{-7} \text{ m}^3 \text{ s}^{-1} \text{ k}$	[31]
$d_l$	$2 \times 10^{-6} \text{ m}$	Experimentally measured [6]
$f_l$	0.2%	Experimentally measured [6]
$f_{ppt}$	1.9%	Experimentally measured [6]
$M_b(T)$	$2.6 \times 10^{-11} \text{ m}^4/\text{Js}$	$M_b(T) = M_{b0} \exp\left(-\frac{Q_M}{RT}\right)$ [3] $M_0=178 \text{ m}^4/\text{Js}$ , $Q_M=147 \text{ KJ/mol}$ [150]
$N_{rex}$	22	Calculated based on the average recrystallized grain diameter in [6]
$Q_A$	205 kJ/mol	[31]
$r_o$	$17.5 \times 10^{-9} \text{ m}$	Experimentally measured in [6]
$t_l$	55 s	Calculated based on the relationship introduced in [86]
$\gamma$	$0.324 \text{ J/m}^2$	[3]
$\gamma_\theta$	$0.185 \text{ J/m}^2$	$\gamma_\theta = \gamma \frac{\theta}{\theta^*} \left(1 - \ln \frac{\theta}{\theta^*}\right)$ $\theta^*=15^\circ$ , $\theta=3.5^\circ$ [3, 6]
$\sigma_{dis}$	165 MPa	$\sigma_y = \sigma_i + \sigma_{SS} + (\sigma_{ppt}^n + \sigma_{dis}^n)^{1/n}$ [61] $\sigma_y=194$ , $\sigma_i=10$ , $\sigma_{ss}=0$ , $\sigma_{ppt}=82 \text{ MPa}$ & $n=2$ [6]
$v$	$7.2 \times 10^{-29} \text{ m}^3$	$v=9b^3$ [5, 6]

A comparative analysis of recrystallization kinetics is conducted by plotting predicted recrystallized area fraction as a function of annealing time, as shown in Figure 6-11 (a). These results are compared with the results obtained from the experimental measurements. A similar trend for the simulation results and experimentally measured data are observed, and the two results are considered in good general agreement. The largest discrepancy is seen at 17% fraction recrystallized, where the experimental work has resulted in a large error bar. The good prediction capability of the simulation work is believed to be the result of including the effects

of concurrent recovery and precipitate coarsening as well as the effects of non-uniform distribution of stored energy and non-random nucleation in the simulation. To further verify the significance of all these considerations on the simulation results, a simple MC simulation (i.e. Simple-MC), where none of these effects are included, is run. The same approach is taken for calculating annealing time for the Simple-MC. The result of the Simple-MC simulation is plotted in Figure 6-11 (a), as well. Not surprisingly, the Simple-MC simulation result exhibits a different kinetic behaviour, with both a longer apparent incubation time and a different recrystallization rate, compared to the result of the Improved-MC simulation. As the apparent incubation time reflects the required time for the growth of nuclei to a noticeable fraction of recrystallized area, the different incubation times for the two curves in Figure 6-11 (a) are linked to different growth rates at the initial state of recrystallization. In contrast to the Simple-MC, the Improved-MC simulation considers the high energy locations as the potential nucleation sites in a microstructure with non-uniform distribution of stored energy. Therefore, in Improved-MC simulation, nuclei are surrounded by high energy neighbours providing a high driving force for growth and in turn resulting in a shorter incubation time compared to Simple-MC. In addition to the different incubation times, the rate of recrystallization progress varies in two curves. Such a variation is better observed when the simulation results are plotted in the way suggested by Johnson-Mehl-Avrami-Kolmogorov (JMAK) theory, as shown in Figure 6-11 (b). In this figure, Simple-MC shows a linear trend for  $\ln[-\ln(1 - f_r)]$  versus  $\ln(t)$ , as predicted by the JMAK relationship. On the other hand, Improved-MC shows deviation from this linear behaviour at the later stage of recrystallization. The observed deviation, which is also frequently reported when experimental data is used [3], is due to the dissatisfaction of the actual physical phenomena by the simple JMAK assumptions of random

nucleation, and constant growth rate of recrystallized grains [152, 153]. It is worth emphasizing that the Improved-MC simulation allows various recrystallized sites of the structure to grow at different rates due to the initial distribution of stored energy. Local amounts of stored energy in turn are functions of time and are reduced through recovery. This reduction of energy is affected by the precipitate coarsening. Coarsening of precipitates also results in a reduction of pinning pressure against grain boundary movement and enhances recrystallization growth.

The presented approach has significantly improved the prediction of microstructural evolution during annealing of a precipitation-hardenable aluminum alloy, where pre-existing large particles act as PSN sites and precipitate coarsening interacts with the annealing phenomena. The results confirm the viability of the developed approach and warrant further advancement of the methodology for microstructural modeling in AA6xxx alloys with complex interactions between precipitation and annealing phenomena.

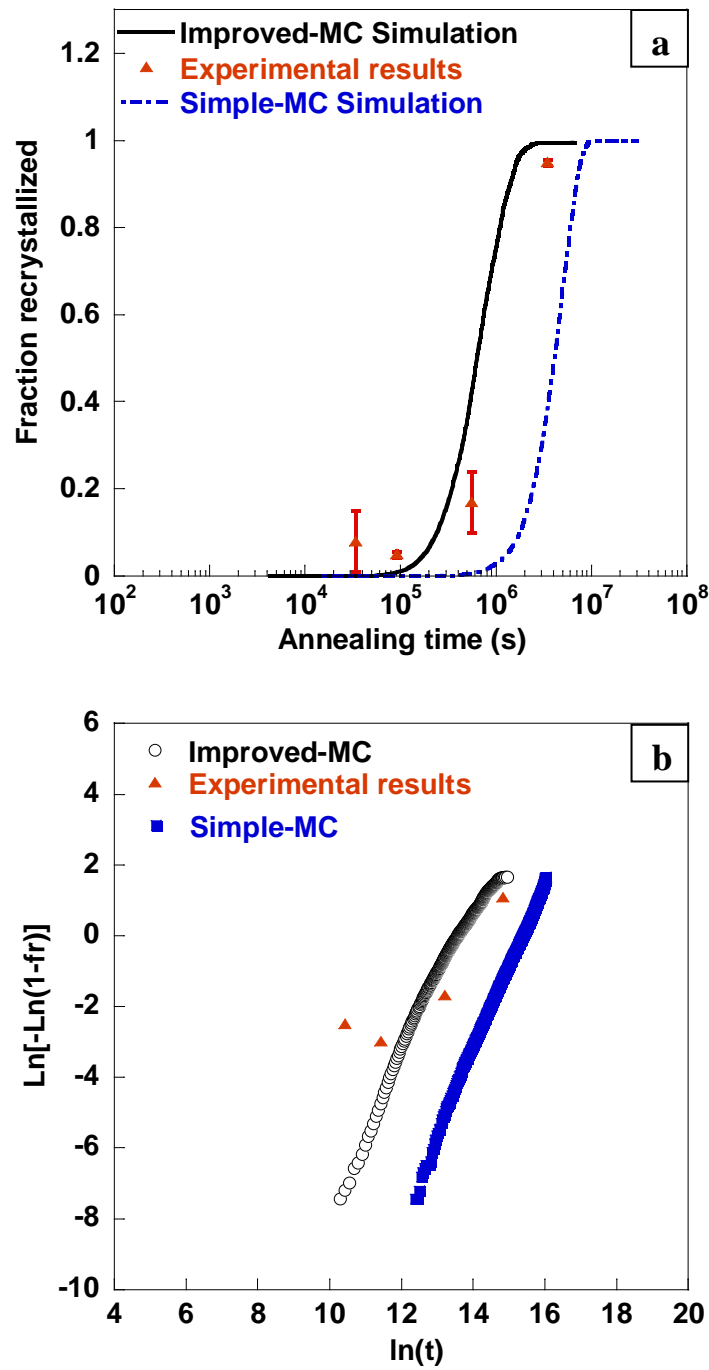


Figure 6-11. a) Recrystallized area fraction calculated from Improved-MC simulation, Simple-MC simulation and experimental results b) JMAK analysis of Improved-MC simulation, Simple-MC simulation, and experimental results. Experimental results are from Ref. [6].

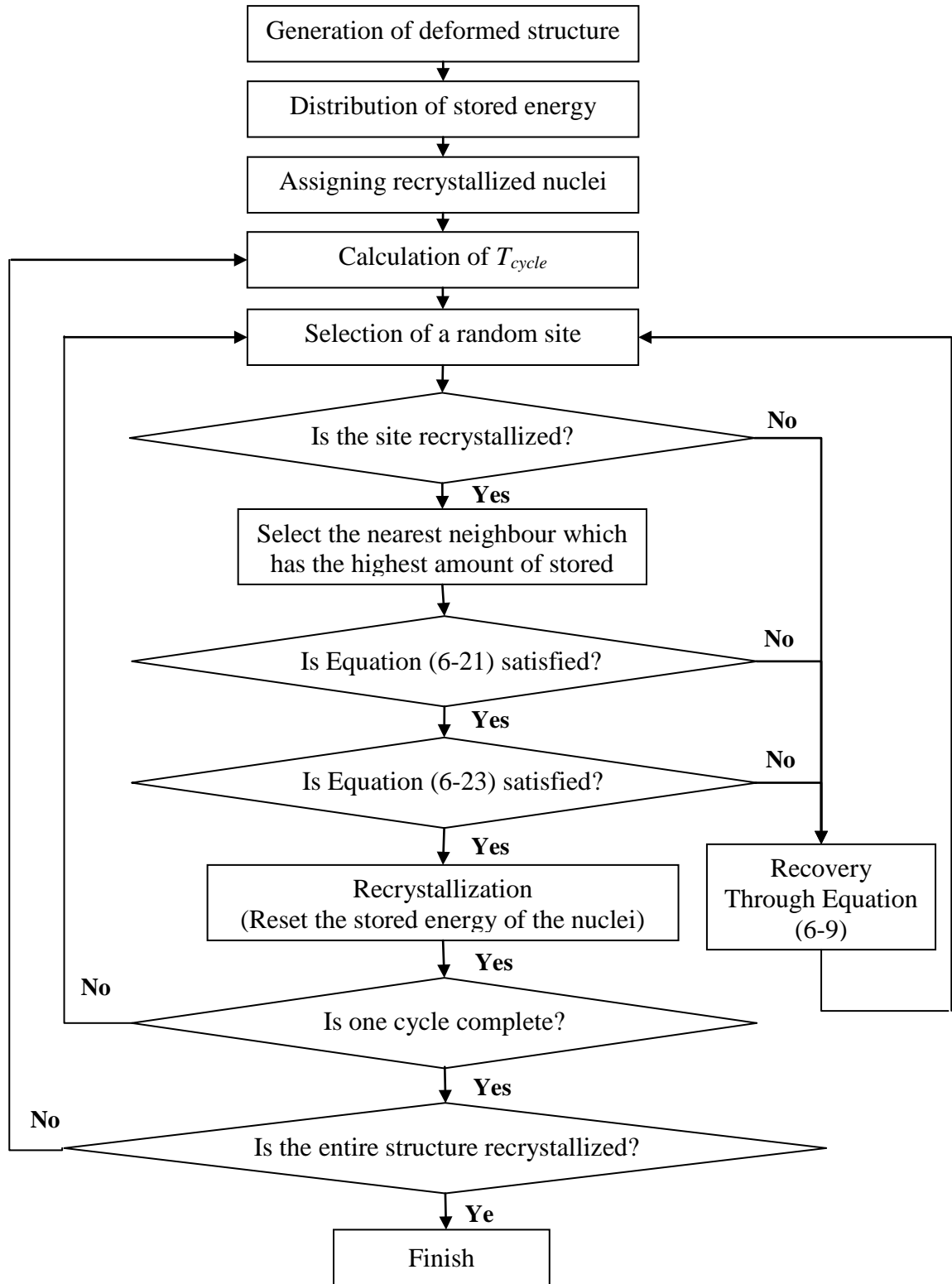


Figure 6-12. Flow chart describing the sequence of steps in simulation for isothermal condition.

### **6.3. Simulating non-isothermal annealing**

In this section, the simulation technique which has been developed in Section 6.2, has been extended for predicting microstructural evolution during non-isothermal annealing. This extension is realized by modifying the simulation algorithm for including the temperature-time relationship during non-isothermal annealing and considering the effect of this relationship on the temperature-dependent elements of the model. This simulation technique is, then, implemented for predicting microstructural evolution during the non-isothermal annealing stage of the TMPM (previously discussed in Section 5.3). The results of the simulation are compared with the results of computer assisted EBSD analysis (Section 6.1).

#### **6.3.1. Analytical formulation and assumptions**

To simulate microstructural evolution during non-isothermal annealing, it is assumed that non-isothermal annealing can be divided into successive infinitesimal steps of isothermal annealing. This assumption is valid for isokinetic conditions where throughout the temperature/time range, the transformation mechanisms remain the same, and the governing equation of transformation can be expressed by spreadable differential equations [154, 155]. The algorithm of the simulation technique for isothermal annealing (Section 6.3) includes three main metallurgical phenomena: precipitate coarsening, recovery, and recrystallization. Each of these phenomena is formulated separately. Subsequently, their interactions are integrated through the MC algorithm. It is assumed that the additivity approach is valid, provided that each of these phenomena is an isokinetic reaction. The criteria for applying the rule of additivity for each of these phenomena are introduced and discussed below:

Precipitate coarsening: The effect of precipitation on microstructural evolution is considered through the effect of precipitation pinning on recovery and grain boundary movement and, thus, is governed by the evolution of precipitate size due to coarsening. Precipitate coarsening is formulated through the LSW equation (Equation (6-11)). The detailed analysis performed by Grong et. al. [156] has proven that precipitate coarsening formulated through the LSW equation may be safely considered as an isokinetic reaction provided that the peak temperature of the thermal treatment is kept below the dissolution temperature of the precipitates. Following Grong et. al. [156], it is assumed that precipitate coarsening can be treated as an isokinetic reaction for the temperature range that the criteria for the additivity rule are satisfied.

Recovery: Progress of recovery and reduction of stored energy in the system during annealing is predicted through Equation (6-9). As explained in Section 2.2.2.1, this equation has been developed assuming that recovery is controlled by thermally activated dislocation re-arrangement and annihilation. Assuming that mechanisms of dislocation movement remain unchanged during the temperature range of the non-isothermal annealing, recovery can be treated as an isokinetic reaction. Applicability of the rule of addition to a similar recovery equation, as part of a model which predicts yield strength evolution during non-isothermal annealing, has been confirmed by the good agreement between the experimental and predicted results in a recent study [157].

Recrystallization: Simulation is developed for discontinuous recrystallization, where recrystallization progresses through nucleation and growth. Considering that site saturated nucleation mechanism is assumed, recrystallization is controlled by the growth of recrystallized nuclei. The growth mechanism is simulated according to the balance of forces

on grain boundary arisen from precipitate retarding effect, stored energy (which is defined by the level of deformation and recovery) and grain boundary mobility. As discussed, recovery and precipitate coarsening are assumed as isokinetic reactions. Therefore, to apply the additivity rule to simulation of recrystallization, isokinetic criteria for evolution of grain boundary mobility during the temperature range of annealing should be examined. Grain boundary mobility is related to temperature according to Equation (2-20).

$$M_b = M_{b0} \exp\left(-\frac{Q_M}{RT}\right) \quad (2-20)$$

In this Equation,  $M_{b0}$  and  $Q_M$  are assumed as temperature independent constants. Assuming that the mechanism of grain boundary mobility is not changing during the annealing temperature range, the additivity rule may be applied to Equation (2-20). The validity of application of the additivity rule to the recrystallization process in case of site saturated nucleation has been widely reported in literature (e.g. [158-160]).

In light of the above, the rule of additivity is considered to be applicable for the three main components of the simulation and the incorporation of non-isothermal conditions into the simulation may be achieved by considering the temperature dependencies of the various increments of the simulation.

### **6.3.2. Simulation algorithm for non-isothermal annealing**

The algorithm for non-isothermal annealing is developed based on the Monte Carlo technique explained in the previous section. Application of the additive rule to the Monte Carlo algorithm is accomplished benefiting from the cyclic nature of the Monte Carlo technique. Each cycle of the simulation is considered as an infinitesimal step of isothermal annealing as schematically presented in Figure 6-13.

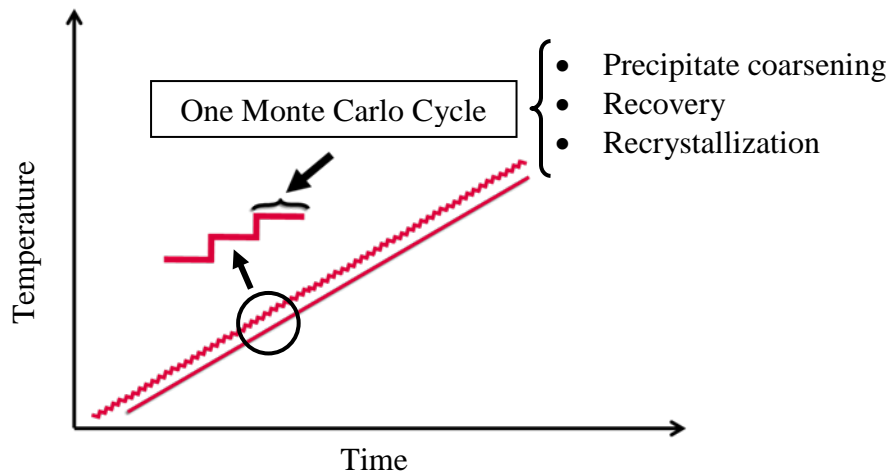


Figure 6-13. Schematic presentation of rule of addition for simulating non-isothermal annealing.

### 6.3.2.1 Generation of deformed structure

Similar to the isothermal algorithm, the first stage of the non-isothermal annealing simulation is the generation of an initial digital microstructure which is used as the input of the simulation. The digital microstructure is generated through the mapping technique described in Section 6.2.4.1. Similarly, following the approach taken in Section 6.2.4.1, a uniform distribution of precipitates is assumed, and subsequently, the influence of precipitates on the annealing mechanism is indirectly included in the simulation by considering their inhibiting effects against recovery and the growth of recrystallized grains. A modified approach is taken for distribution of stored energy within the deformed structure in order to accommodate the deformed microstructure that is achieved during cold rolling. In Section 6.2.4.1, stored energy is distributed in the microstructure to accommodate a non-uniform allocation of dislocations and stored energy within the deformed grains. This approach is not applicable for deformation conditions that lead to uniform distribution of dislocations inside the microstructure, such as

the as-deformed condition observed in Section 5.2.1. In the current simulation, it is assumed that stored energy of deformation consists of three main elements:

1. the stored energy component due to uniformly distributed dislocations within the deformed grains, i.e.  $H_{0g}$ ,
2. the stored energy component attributed to the additional dislocations which are accumulated around large particles, i.e.  $H_{0l}$ , and
3. the energy of grain boundaries, i.e.  $H_{0gb}$ .

The total energy of the system is assumed to be the linear summation of the above three components:

$$H_0 = H_{0g} + H_{0l} + H_{0gb} \quad (6-24)$$

The magnitudes of parameters  $H_{0g}$  and  $H_{0l}$ , are calculated from Equation (6-6) and Equation (6-7), respectively as described in Section 6.2.3. To calculate  $H_{0gb}$ , area fraction of lattice sites that corresponds to grain boundaries (their orientation  $S_i$  is different than their neighbours') are calculated and the associated amount of energy is computed according to high angle grain boundary energy,  $\gamma$ :

$$H_{0gb} = \frac{1}{2} \sum_{i=1}^N \sum_{j=1}^{N_n} \gamma (1 - \delta_{i,j}) \quad (6-25)$$

For spatial distribution of stored energy, initially,  $H_{0g}$  is uniformly distributed inside the microstructure. Subsequently,  $H_{0l}$  is added around the large particles through the same approach which has been taken in Section 6.2.4.1. Finally,  $H_{0gb}$  is added to grain boundary areas. To accommodate uniformity and continuity of stored energy distribution in the system, it is assumed that stored energy of the grain boundary is sharply reduced to stored energy of the lattice sites located inside the grains; in contrast to the approach taken in Section 6.2.4.1

which results in a gradual decrease of stored energy from the grain boundary toward the center of the grain. The sharp degradation of stored energy is realized by considering an exponential decrease of stored energy from the grain boundary to the adjacent sites. The stored energy distribution across a horizontal scan of a generated microstructure after 80% cold-rolled reduction is presented in Figure 6-14. In this figure, the sharp increases in the stored energy values correspond to grain boundary areas.

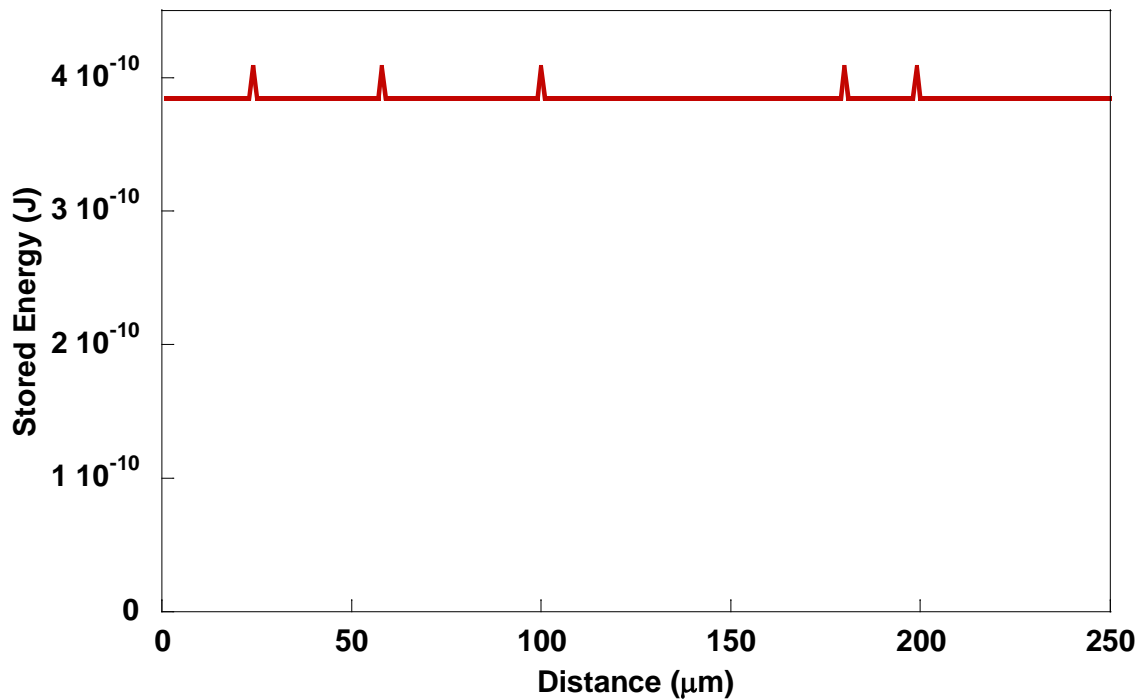


Figure 6-14. Stored energy distribution across deformed structure.

### 6.3.2.2 Simulation microstructural evolution

Recrystallization nucleation is assumed to occur entirely at the onset of annealing through site saturated nucleation. For spatial distribution of the nuclei, it is assumed that all lattice sites of the microstructure may potentially act as nucleation sites. However, higher chance is given to the sites which have a higher level of stored energy (i.e. grain boundaries

and around large particles) by considering a weight factor. Considering the nucleation chance,  $N_{\text{rex}}$  number of sites has been selected as recrystallized nuclei and their stored energy is reset to zero. Microstructural evolution during annealing is simulated by growth of these recrystallized nuclei.

Growth of nuclei and their transformation to recrystallized grains are treated through a Monte Carlo algorithm. To simulate microstructural evolution during non-isothermal annealing, a time interval (i.e.  $\Delta t$ ) is assigned to each Monte Carlo cycle. At the beginning of each cycle, the annealing temperature of the cycle is calculated through the following equation:

$$T(t) = T_o + \omega \Delta t \quad (6-26)$$

where  $T_o$  is the temperature of the previous step and  $\omega$  is the heating rate of the non-isothermal annealing process. At the start of each Monte Carlo cycle, based on the cycle temperature and the results of previous cycles, the magnitude of the temperature-dependent parameters are calculated. These parameters are subsequently employed to simulate recrystallization progress, precipitate coarsening, and the reduction of stored energy due to recovery for the  $\Delta t$  duration at  $T(t)$ . The sequence of the simulation within each Monte Carlo cycle is listed as follows:

- 1- A lattice site is selected in a random manner.
- 2- If the selected site is recrystallized (i.e. the stored energy of the site is nil), the possibility of the growth of the recrystallized site toward the non-recrystallized neighbouring sites is examined.
- 3- If the selected site is non-recrystallized, the stored energy of the site is reduced through recovery.

- 4- One Monte Carlo cycle is completed when all lattice sites of the microstructure are examined.

Once a recrystallized site is selected, it may grow. The possibility of the growth of the selected recrystallized nuclei is verified by examining whether reorientation of the non-recrystallized neighbours to recrystallized site (resetting the stored energy to zero) is kinetically and thermodynamically possible. The approach defined in Section 6.2.4.2 is used to check whether the reorientation is thermodynamically accepted, i.e. Equation (6-21) is satisfied. To check whether transformation is kinetically possible, the distance that the grain boundary of the selected nuclei can move in  $\Delta t$  time period is calculated:

$$X_{cycle}^i = M_b(T)[H_i(t, T) - Z(t, T)]\Delta t + X_0^i \quad (6-27)$$

where  $X_{cycle}^i$  is the distance that the grain boundary can move in one cycle, and  $X_0^i$  is the summation of  $X_{cycle}^i$  from previous unsuccessful transformation attempts. As defined in Equation (6-27),  $X_{cycle}^i$  depends on the mobility of the boundary which, in turn, depends on the annealing temperature, stored energy of the selected site, pinning force inserted by precipitates, and the magnitude of previous unsuccessful transformations,  $X_0^i$ . Transformation is kinetically accepted if  $X_{cycle}^i$  is larger than one lattice site:

$$X_{cycle}^i \geq L \quad (6-28)$$

Transformation of the selected site to a recrystallized site, and in turn, growth of recrystallized grain, is only accepted when Equation (6-21) and (6-28) are both satisfied. Otherwise, the stored energy of the selected site (i.e.  $H_i$ ) is reduced through recovery (Equation (6-9)) and the magnitude of  $X_0^i$  for the succeeding Monte Carlo cycle is replaced by  $X_{cycle}^i + X_0^i$ . The Monte Carlo algorithm is continued till all of the microstructure is recrystallized.

### 6.3.3. Calibration and implementation of the simulation

In this section, the calibration parameters and physical properties which are required for implementing the simulation technique in order to predict microstructural evolution in AA6451 during the non-isothermal annealing phase of the TMPM are identified. The required parameters are categorized into the following main categories:

- parameters associated with material properties;
- parameters associated with the annealing condition;
- parameters associated with Microstructural properties of the initial condition;
- parameters associated with the deformation condition;
- parameters required for predicting precipitate coarsening;
- parameters required for predicting recovery;
- parameters required for predicting recrystallization;

Parameters related to each of the above categories will be discussed below.

#### Parameters associated with material properties

Although the simulation has been developed for predicting microstructural evolution in AA6xxx aluminum alloys, it can be applied to other precipitate-containing alloys, provided that the assumptions of the simulation remain valid. The magnitude of material property parameters which are required for the simulation of AA6451 aluminum alloy are listed in Table 6-3.

#### Parameters associated with annealing conditions

The simulation technique is designed for conditions where annealing phenomena are concurrent with precipitate coarsening. Therefore, to implement the simulation technique for the prediction of microstructural evolution during TMPM, the temperature range for

simulation of the non-isothermal annealing should associate with precipitate coarsening. As discussed in Chapter 5, evidences for precipitate coarsening as the dominant mechanism for precipitate evolution, after annealing to and above 180°C have been observed. Coarsening can, however, be concurrent with precipitate nucleation and growth. Considering the long time of non-isothermal annealing at low temperatures (prior to reaching 180°C), nucleation of precipitation should already have been completed at this stage of annealing. Some levels of precipitation growth, on the other hand, might be concurrent with precipitate coarsening during non-isothermal annealing above 180°C. For simplicity, as a first order approximation, it is assumed that the role of precipitate growth is negligible and precipitate coarsening is assumed as the solo mechanism for precipitate evolution during non-isothermal annealing above 180°C. Therefore, the initial temperature for simulation is considered as 180°C. The heating rate of annealing is the same heating rate as the actual non-isothermal annealing stage of the TMPM, i.e. 0.4°C/min.

#### Parameters associated with microstructural properties of initial condition

For implementing the non-isothermal annealing simulation, microstructural properties including  $f_i$ ,  $d_l$ ,  $f_{ppt}$  and  $r_o$  should be defined. The magnitude of the volume fraction,  $f_i$ , and average diameter of the large particles,  $d_l$ , which are measured experimentally (Section 5.2.2) are listed in Table 6-3. Parameters  $f_{ppt}$  and  $r_o$  are assigned according to available information in the literature [18]. The initial temperature of simulation, i.e. 180°C, corresponds to the highest level of hardness which is achieved during non-isothermal annealing. TEM results on the NA-CR-180 sample (Chapter 5) cannot be used for estimation of  $f_{ppt}$  and  $r_o$ , due to the very small size of the precipitates. Therefore, as a first order approximation, it is assumed that

volume fraction and size of precipitates may be estimated as being equal to the values reported in literature for AA6111 (with a similar composition to AA6451) which has been aged to the peak of aging after natural aging [18]. These values are reported in Table 6-3.

#### Parameters associated with deformation conditions

The level of cold rolling dictates the amount of elongation of the deformed grain in the initial microstructure which is used as the input of the simulation, as well as the level of the energy that is stored in the system. The amount of elongation along the rolling direction is defined based on the true strain of deformation, i.e.  $\epsilon$ . To calculate the stored energy of the system through Equation (6-24), the three components of stored energy,  $H_{0l}$ ,  $H_{0g}$  and  $H_{0gb}$  should be calculated.

$H_{0gb}$  is defined through Equation (6-25), using values of grain boundary energy which are reported in Table 6-3. For calculating  $H_{0l}$  and  $H_{0g}$ , the densities of dislocation around large particles i.e.  $\rho_l$ , and inside the deformed grains, i.e.  $\rho_g$ , at the initial temperature of non-isothermal annealing should be computed. The parameter  $\rho_l$  is calculated through Equation (6-4) using the values reported for  $f_l$ ,  $d_l$  and  $\epsilon$  in Table 6-3. To calculate  $\rho_g$ ,  $\sigma_{dis}$  should be identified. As explained in Section 2.2.1.1, the contribution of dislocations, i.e.  $\sigma_{dis}$ , to the overall yield strength of the deformed and aged alloy may be computed through Equation (2-9):

$$\sigma = \sigma_i + \sigma_{ss} + (\sigma_{ppt}^n + \sigma_{dis}^n)^{1/n} \quad (6-29)$$

where for the overaged condition,  $n=2$  [61]. The intrinsic strength of aluminum, i.e.  $\sigma_i$ , is estimated as 10Mpa. For the peak aged and overaged conditions, the contribution from solid solution may be assumed to be negligible. Therefore, for the NA-CR sample, Equation (6-29) is reduced to:

$$\sigma = 10 + (\sigma_{ppt}^2 + \sigma_{dis}^2)^{1/2} \quad (6-30)$$

Therefore,  $\sigma_{dis}$  may be calculated from Equation (6-30) provided that the magnitude of  $\sigma_{ppt}$  and  $\sigma$  are known.  $\sigma$  is estimated from the measured microhardness value of the sample annealed to 180°C, i.e. 155 HVN, using Equation (6-31) [161].

$$\sigma = \frac{HVN}{0.33} - 16 \quad (6-31)$$

To identify  $\sigma_{ppt}$ , it is assumed that at the peak aged condition, the contribution of precipitate to the yield strength of the samples that has been deformed prior to aging (i.e. NA-CR) is the same as the contribution of precipitate to the yield strength of the sample which has not been deformed prior to aging (i.e. NA). The yield strength of the non-deformed material, i.e. NA, has been calculated from the corresponding microhardness value, i.e. 131 HVN at 230°C. Since, the material is not deformed, for the NA condition Equation (6-29) is reduced to:

$$\sigma_{NA} = 10 + \sigma_{ppt} \quad (6-32)$$

Substituting  $\sigma_{ppt}$  in Equation (6-30),  $\sigma_{dis}$  is calculated and reported in Table 6-3.

#### Parameters required for predicting precipitate coarsening

To predict the evolution of precipitate size during non-isothermal annealing through Equation (6-11), the rate constant  $k_c$ , which is related to  $A$  and  $Q_A$  through Equation (2-4) should be calculated.

$$k_c = \frac{A}{T} \exp\left(\frac{-Q_A}{RT}\right) \quad (6-33)$$

For this purpose,  $A$  and  $Q_A$  are considered to be temperature independent and equivalent to the values calculated by Esmaili et. al.[31], for a similar alloy. These values are reported in Table 6-3.

### Parameters required for predicting recovery

The key parameters in predicting reduction of stored energy through recovery are the activation energy and activation volume of recovery,  $U_r$  and  $V_r$ , respectively. As explained in Section 2.2.2.1, depending on the level of solute element in the matrix, activation energy for recovery varies between activation energy for the diffusion of solvent atoms and the activation energy for diffusion of the solute atoms in the matrix [102]. For the temperature range of the simulation, as the amount of the solute in the matrix is small,  $U_r$  is considered to be equal to the energy for self diffusion of aluminum (i.e. 142 KJ/mol). Activation volume for recovery in AA6xxx aluminum alloys has been shown to vary in the range of  $6b^3$  to  $12b^3$  [6]. Preliminary simulation results have shown that the final results of simulation are not significantly affected when activation volume varies in this range. Therefore, the activation volume is set equal to an average value of  $9b^3$ .

### Parameters required for predicting recrystallization

The number of recrystallized nuclei,  $N_{\text{rex}}$ , is obtained from the number density of recrystallized grains that is calculated from the EBSD results of the NA-CR-380-20min sample. To analyse the kinetics of grain growth from Equation (6-27),  $M_b$  is calculated according to Equation (2-20), where  $M_{b0}$  and  $Q_M$  are assumed to be equal to the values that Huang et. al. [150] have calculated for commercially pure aluminum. This assumption is justified, considering the fact that in the overaged condition, the contribution of solutes against grain boundary mobility is negligible, and the effect of precipitates against grain boundary movement is included separately. The corresponding values for  $M_{b0}$  and  $Q_M$  are reported in Table 6-3.

The parameters identified in Table 6-3 have been used to implement the simulation technique for the prediction of microstructure evolution during non-isothermal annealing of an AA6451 alloy. Considering the results of experimental analysis on microstructural evolution of the alloy during annealing, the main assumptions of the model, including site saturated nucleation and uniform distribution of dislocations in the deformed structure, are valid. Simulation has been applied on a deformed structure which has been mapped into a 250x300 square lattice of 250x300  $\mu\text{m}^2$ . The results of simulation are provided in the following section.

**Table 6-3 Material and simulation parameters (non-isothermal simulation)**

Category	Parameter	Value	Source
	Precipitate radius at start of simulation, $r_o$	$3.4 \times 10^{-9} \mu\text{m}$	[18]
Microstructural parameter	Volume fraction of precipitates, $f_{ppt}$	$7.9 \times 10^{-9}$	[18]
	Diameter of large particles, $d_l$	$2 \times 10^{-6} \mu\text{m}$	Measured
	Volume fraction of large particles, $f_l$	0.32%	Measured
Stored energy	Dislocation strengthening, $\sigma_{dis}$	243 MPa	Calculated
Precipitate coarsening	Equation constant, A	$8 \times 10^{-7} \text{ m}^3 \text{ s}^{-1} \text{ k}$	[31]
	Apparent activation energy, $Q_A$	205 kJ/mol	[31]
Recovery	Activation volume, $V_r$	$9b^3$	[6]
	Activation energy for recovery, $U_r$	142 kJ/mol	Assumed
Recrystallization	Grain boundary constant, $M_{b0}$	$M_0 = 178 \text{ m}^4/\text{Js}$ ,	[150]
	Activation energy for boundary migration, $Q_M$	147 KJ/mol	[150]
Deformation and annealing conditions	True strain, $\epsilon$	1.6	Calculated
	Initial annealing temperature	180°C	Assigned
	High angle grain boundary energy, $\gamma$	$0.324 \text{ J/m}^2$	[163]
Material parameters	Young Modulus, E	70 GPa	[163]
	Shear Modulus, G	26 GPa	[163]
	Burgers vector, b	$2 \times 10^{-10} \text{ m}$	[163]

#### 6.3.4. Simulation results and discussion

Figure 6-15 shows six successive predicted microstructures during non-isothermal annealing. In these images, recrystallized nuclei/grains are presented by different shades of gray contrast and large particles and grain boundaries of deformed grains are presented by black contrast. Except for the fully recrystallized condition, simulation results are presented for the same annealing conditions as the EBSD results presented in Section 5.2.3 (i.e. end annealing temperature of 180°C, 235 °C, 300 °C, 320 °C and 340°C). No recrystallization progress is observed in Figure 6-15 (a) and (b) which corresponds to low annealing temperature (180°C and 235 °C). By continuing annealing to higher temperatures, initially, the nuclei which are located at areas adjacent to large particles (which are shown by black contrast) grow, and then gradually all other recrystallized nuclei grow and form a fully recrystallized microstructure after annealing to 356°C. Comparing simulation and EBSD results, a general qualitative agreement between experimental and simulation results are observed, except for the end annealing temperature of 320°C, where the EBSD map (Figure 6-6 (c)) shows preferential recrystallization in one of the deformed grains. The preferential recrystallization is due to the preferred orientation of the deformed grain which is not included in the simulation algorithm and as a result is not reflected in the simulation result. As explained in Section 5.3.4 a limited fraction of the microstructure is affected by the initial orientation of the deformed grains [138], and as a result simulation results are not remarkably affected by neglecting the orientation effect.

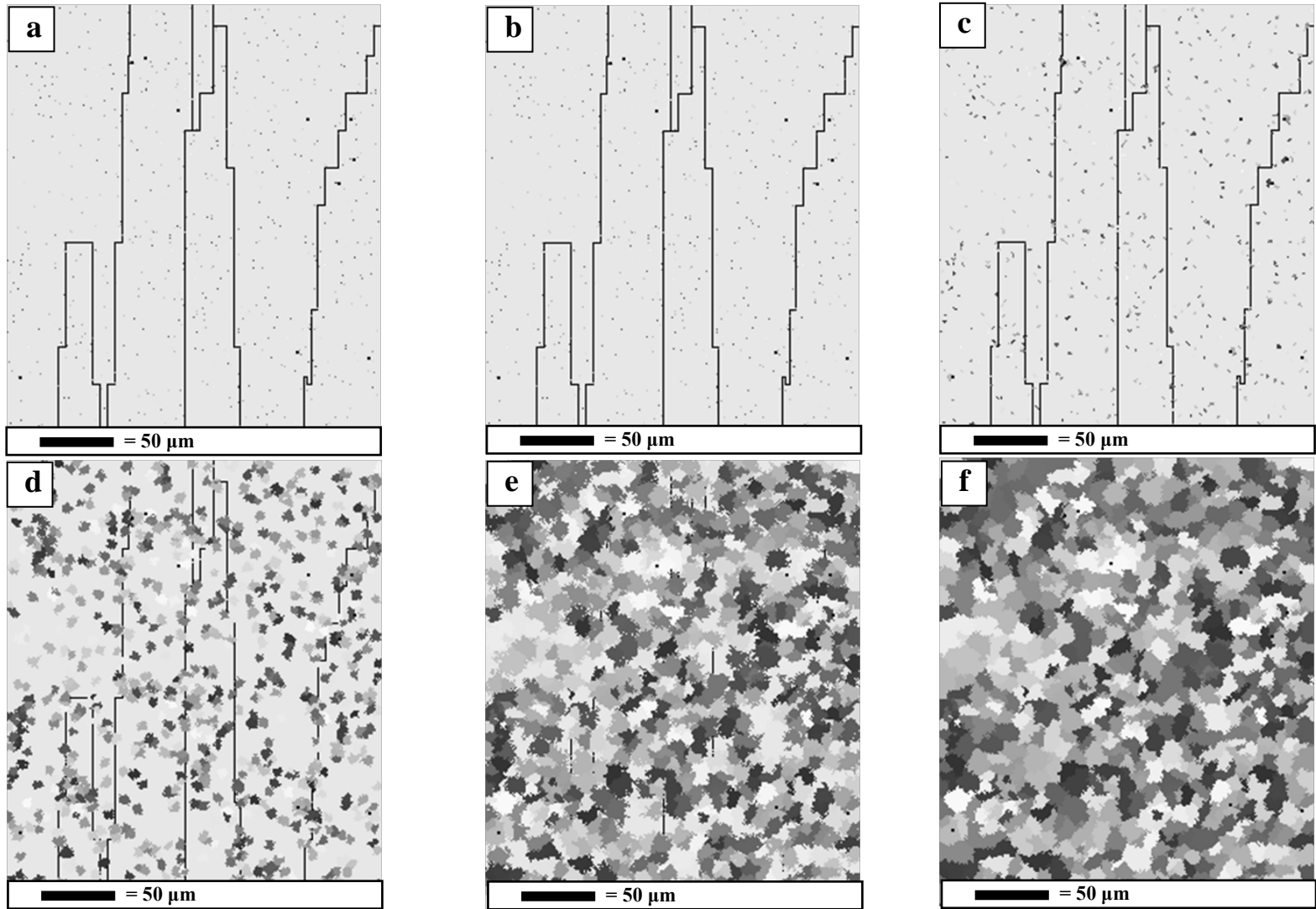


Figure 6-15. Non-isothermal simulation results after annealing to a) 180°C, b) 235°C, c) 300°C, d) 320°C, e) 340°C and f) 356°C.

For quantitative analysis of the simulation results, the recrystallized area fraction during simulation is calculated and presented in Figure 6-16. The quantified results of the computer assisted EBSD analysis are also plotted in the same figure for comparison. A good agreement between the simulation and quantified EBSD results is observed. It is seen that while an excellent match between the EBSD and simulation results exists at the early stages of annealing, simulation and EBSD results slightly deviate at the final stages of annealing. The agreement between the initial incubation period (180°C to 300°C) of EBSD and simulation results suggests that although a site saturated nucleation is assumed, proper simulation of the nuclei growth results in accurate prediction of recrystallization onset. The deviation at the later stage of annealing implies that simulation predicts the completion of recrystallization at slightly lower temperatures than experimental measurements. Progress of recrystallization during simulation is dictated by three main factors: i) remaining stored energy in the system which is affected by the initial level of stored energy and progress of recovery, ii) grain boundary mobility and iii) precipitate pinning. Completion of recrystallization at lower temperatures, therefore, may be attributed to the following reasons:

- 1- overestimation of the stored energy of the system;
- 2- underestimation of the effect of recovery and as a result preservation of higher stored energy in the system;
- 3- overestimation of grain boundary mobility;
- 4- underestimation of precipitate pinning.

Although the deviation may result from a combination of the above reasons, as deviation occurs at a higher annealing temperature, it may be suggested that those parameters which are more sensitive to temperature are the main origin of deviation. The initial level of

stored energy is temperature independent. Moreover, an excellent agreement between experimental and simulation results is observed at the initial stages of annealing. Therefore, the estimated stored energy cannot be responsible for the observed deviation. Similarly, the effect of recovery should be more pronounced at lower annealing temperatures, where recovery acts as the main restoration mechanism. Hence, the deviation at later stages of annealing is mainly attributed to overestimation of grain boundary mobility, which has an Arrhenius relationship with temperature and/or underestimation of precipitate pinning.

Grain boundary mobility during simulation is dictated by the values of  $M_{b0}$  and  $Q_M$  (Equation (2-20)). Unfortunately, there is significant lack of information in literature for these values, and such information has not been specifically measured or predicted for AA6xxx alloys. The employed values of  $M_{b0}$  and  $Q_M$  in the simulation correspond to single phase aluminum and might not be completely true for the simulated condition. The level of precipitate pinning depends on the input values of  $r_o$  and  $f_{ppt}$  which have been estimated from available information in the literature. The results of simulation may be improved by calculation of these values through either quantitative experimental analysis or development of a physically based modeling technique for prediction of precipitate evolution prior to coarsening.

In addition to the main reasons discussed above, part of the deviation may have arisen due to the underestimation of recrystallized fraction through computer assisted EBSD analysis as well as errors which are associated with other calibration parameters as well as neglecting the effect of deformed grain orientation on microstructural evolution during annealing.

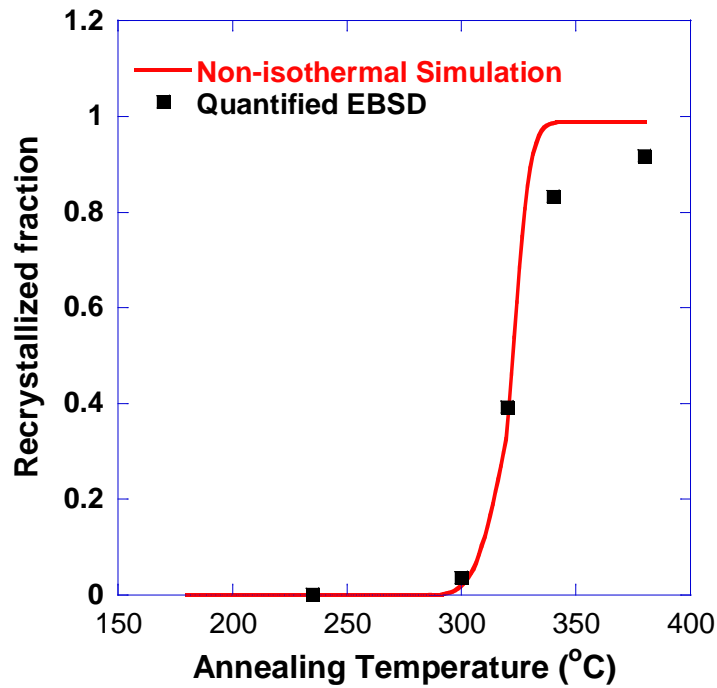


**Figure 6-16. Recrystallized area fraction calculated from Non-isothermal simulation and experimental results.**

In addition to recrystallized fraction, the equivalent average diameter of the recrystallized grains in the simulated microstructure is calculated and compared with the quantified EBSD results in Figure 6-17. A very good agreement between predicted and experimental results is observed. The largest deviation is seen at 235°C. At this annealing condition, EBSD results show the presence of few recrystallized grains which form a very small fraction of the microstructure. This small fraction of recrystallized grains has been formed due to localized variations of stored energy in the real microstructure, which has not been included in the simulation. Such in-detail microstructural inhomogeneities may be included in the simulation by using EBSD maps as the input of the model [162]. Although the present simulation technique is compatible with using EBSD maps as the input of the model, the main limitation is obtaining a reliable EBSD map for a highly deformed alloy, such as in

the case of this research. The EBSD map corresponding to NA-CR-180 (Figure 5-23 (a)) cannot be used as the input of the simulation either, due to the large number of un-indexed points in the map and the corresponding artifacts.

The fluctuation of average grain diameter in temperature range (270°C to 300°C) corresponds to the very initial stages of recrystallization. At this range of temperature, recrystallized fraction is very small (as shown in Figure 6-16 ) and the reported average grain diameter is calculated based on the size of a few recrystallized grains. Due to the small number of grains, the average value is strongly affected by changes in the size of each of these grains. Variation in their growth rate, which is dictated by their localized position and the stored energy of their surrounding neighbours, and growth of new nuclei results in the fluctuation of average grain size. By continuing annealing, the number of recrystallized grains is increased and the reported average becomes less sensitive to the size of individual grains. Therefore, a smoother curve is observed for annealing above 300°C which is associated with the initiation of accelerated recrystallization.

To further verify the results of simulation, the grain size distribution in the fully recrystallized microstructure achieved through simulation is plotted in Figure 6-18 and compared with the grain size distribution in the NA-CR-380-20m sample. Both plots show log-normal distributions, and a good agreement between simulation and experimental results is observed. The log-normal distribution is considered to be due to the inhomogeneities in the distribution of stored energy which have been reflected in simulation results by considering dislocation accumulation around large particles and at grain boundaries. Without these considerations a normal distribution of grain size would have been achieved through simulation [164, 165].

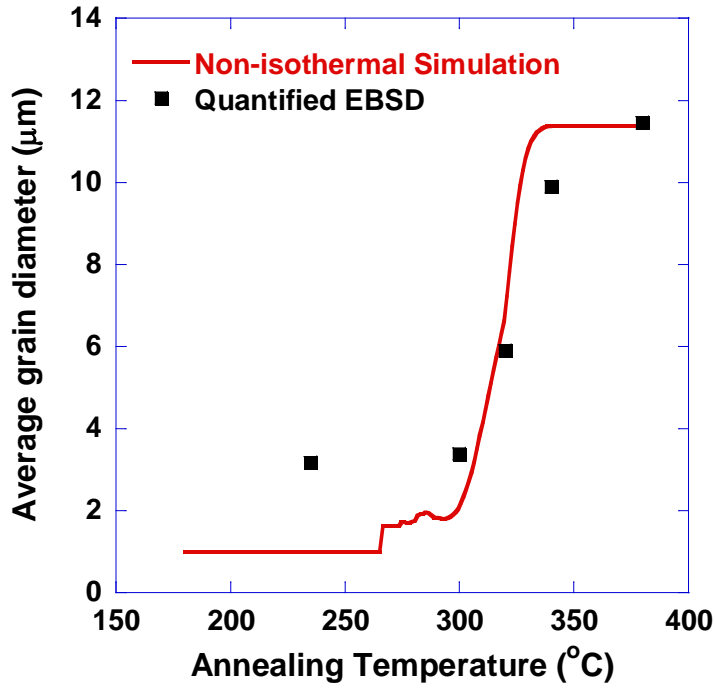


Figure 6-17. Average diameter of recrystallized grains calculated from Non-isothermal simulation and experimental results.

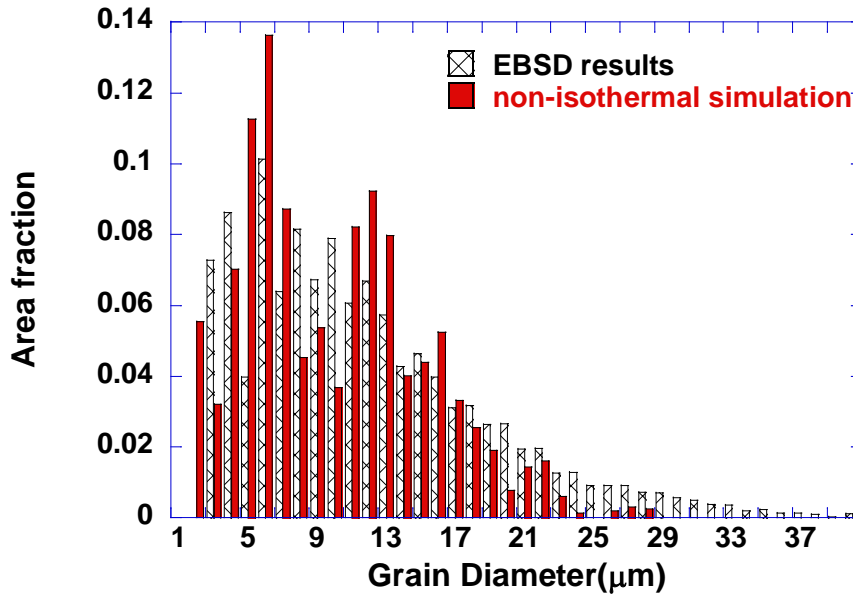


Figure 6-18. Grain size distribution calculated from non-isothermal simulation and experimental results for the fully recrystallized conditions.

#### **6.4. Range of applicability and limitation of the model**

A physically based computer simulation technique has been developed for the prediction of microstructural evolution during isothermal and non-isothermal annealing of precipitate hardenable AA6xxx aluminum alloys when annealing is concurrent with precipitate coarsening. The good agreement between various simulation and experimental results suggests that the method can be considered as a viable technique for the simulation of microstructural evolution during isothermal/non-isothermal annealing where precipitate coarsening, recovery and recrystallization interact. It further implies that the simplifying assumptions that were made in development of the simulation algorithm are reasonable for the current system. However, the range of applicability of the simulation technique is limited as follows:

- 1- The simulation technique is developed for conditions where precipitate coarsening is concurrent with recrystallization. In other words, the simulation technique is only applicable for annealing conditions where precipitate nucleation and growth are completed prior to recrystallization.

In addition, the effect of precipitate dissolution is not included in the simulation, and hence, annealing temperature should be lower than the precipitate dissolution temperature.

- 2- Generation of deformed microstructure and mechanism of recovery is designed for, and its application is restricted to non-cell forming deformation conditions.
- 3- The simulation technique is developed for discontinuous recrystallization, where recrystallization occurs through nucleation and growth. Therefore the simulation

cannot be used for prediction of microstructural evolution during continuous recrystallization.

- 4- A site saturated nucleation mechanism is assumed for recrystallization; therefore the model is applicable for annealing conditions that this assumption is reasonable.
- 5- The effect of grain orientation is not included in the simulation. The simulation may be implemented for predicting microstructural evolution in annealing conditions that this effect is not dominant.

## **Chapter 7. SUMMARY, CONCLUSIONS AND FUTURE WORK**

### **7.1. Summary and conclusions**

Microstructural evolution in an AA6xxx aluminum alloy during a non-isothermal annealing stage of a thermomechanical processing route which leads to significant grain refinement has been characterized and simulated through development of a new computational modeling technique. It has been seen that microstructural evolution is dictated through the extensive interactions between precipitation, recovery and recrystallization processes. The important conclusions of the work are summarized in this Section in two main categories: Microstructural evolution and Computational modeling.

#### **Microstructural evolution**

- TEM studies on the as-deformed condition have revealed a relatively uniform dislocation distribution. DSC analysis and microhardness measurements provide evidence for the presence of natural aging clusters and solute elements in the matrix prior to deformation. Therefore, the uniform distribution of dislocations is linked to the inhibition of dynamic recovery by the solute elements and natural aging clusters. Inhibition of dynamic recovery results in the presence of a high density of dislocations, and in turn, a high level of stored energy in the as-deformed condition.
- The combination of TEM, DSC and EBSD analyses has revealed strong evidence for the interaction of precipitates with dislocations during the initial stages of non-isothermal annealing. The uniformly distributed precipitates inhibit dislocation re-

arrangement and recovery, leading to the preservation of the high level of stored energy in the system up to the onset of recrystallization.

- Recrystallization nucleation has been observed to mainly occur uniformly within the microstructure. The uniformly distributed recrystallized nuclei are suggested to evolve from pre-existing small, dislocation-free regions in the microstructure. Although evidence for nucleation at grain boundaries and large particles has been observed, the combination of EBSD and TEM analysis shows that the contribution of localized nucleation compared to uniform nucleation is small.
- Recrystallization is initiated by the nucleation of new grains in the well-preserved high energy sites which are uniformly-distributed within the entire structure. Growth of the recrystallized nuclei has been seen to be limited through the effective pinning of grain boundaries by precipitates.
- The mutual effects of precipitate coarsening and enhanced grain boundary mobility by continuing annealing to higher temperatures at the late stages of annealing result in the completion of the recrystallization process and the formation of a fine-grained microstructure.
- Recrystallization has been observed to be concurrent with precipitate coarsening and occurs discontinuously through a nucleation and growth mechanism.
- The combination of TEM and SEM microstructural analysis has revealed a uniform distribution of precipitates at entire stages of annealing. Such a uniform distribution of precipitates is linked to the homogeneous nucleation of precipitation at initial stages of annealing and uniform distribution of dislocations which can act as heterogeneous nucleation sites for precipitation and easy diffusion paths for their growth.

## Computational modeling

- To predict and simulate microstructural evolution in AA6xxx aluminum alloy as a result of the complex interaction between precipitation, recovery and recrystallization, a new physically based computational modeling technique is developed. Modeling is accomplished through integration of analytical formulation in a Monte Carlo algorithm.
- The computational modeling technique has been first developed for simulation of microstructural evolution in precipitate hardenable AA6xxx aluminum alloys during isothermal annealing and, then, extended for simulation of non-isothermal annealing.
- Microstructural evolution during annealing is simulated considering competition between recovery and recrystallization for reduction of stored energy in the system, when annealing is concurrent with precipitate coarsening.
- Evolution of precipitate size through coarsening and reduction of stored energy through recovery has been predicted by employing and/or modifying existing analytical equations. The size of the precipitates dictates the retardation effect of precipitates against recovery, as well as the level of grain boundary pinning by precipitate pinning.
- A Monte Carlo algorithm is generated to simulate recrystallization and integrate effects of recovery, precipitation and local microstructural inhomogeneities (grain boundaries and large particles). Simulation is developed for discontinuous recrystallization which progresses by nucleation and growth. Recrystallization nucleation is assumed to occur through a site saturated mechanism while growth of recrystallized nuclei is being controlled by the balance of a local level of stored energy and precipitate pinning effect.

- Simulation is applied on a digital microstructure that is generated based on the level of deformation, dislocation distribution and microstructural properties including average size and volume fraction of precipitate and large particles (dispersoids and constituents) at the start of annealing.
- A new approach has been introduced to relate simulation time to real annealing time, which provides the unique ability of considering concurrent time-dependent phenomena, including recovery and precipitate coarsening, in the simulation.
- The computational modeling technique is implemented on AA6xxx aluminum alloys for isothermal and non-isothermal annealing conditions. The simulation results are compared with the results of experimental analysis. The good agreement between simulation and experimental results show that the effects of concurrent precipitation, recovery and recrystallization, in addition to the effect of microstructural inhomogeneities, have been correctly included in the modeling algorithm.
- The computational modeling technique predicts that when a heating rate of 0.4°C/min is used the overall recrystallization process initiates at 300°C and completes at 356°C. These temperatures are in very good agreement with the experimentally obtained data for the initiation and termination of recrystallization.

## **7.2. Future work**

- In-situ SEM/EBSD analysis on grain boundary mobility during non-isothermal annealing is proposed. The results will address lack of information in literature about grain boundary mobility in precipitate containing AA6xxx aluminum alloys. The

combination of this results and quantitative TEM analysis on precipitate size and distribution will assist in improving prediction capabilities of the computational modeling technique.

- The computational model can further be improved by including the effect of grain orientation on microstructural evolution. The generated algorithm has the potential for such addition; however, the main limitation would be the significant increase in the size of the digital microstructure, and in turn, the simulation time for capturing a statistically correct distribution of grain orientation in the system. To overcome this limitation, the development of a multi-scale simulation technique is recommended.
- To simulate the entire thermomechanical processing route, it is suggested to couple the developed model with a deformation model/simulation technique which can predict the as-deformed microstructure. The result of the deformation model then can be used as the input of the computational modeling technique for prediction of microstructural evolution during annealing.
- The range of applicability of the computational modeling technique may be improved by including the entire sequence of precipitation (nucleation, growth and coarsening) in the algorithm of the simulation.

## REFERENCES

- [1] Esmaeili, S., Lloyd, D.J., and Jin, H., *PCT application filed by the University of Waterloo*, (2009).
- [2] Lillywhite, S.J., Prangnell, P.B., and Humphreys, F.J. *Materials Science and Technology*, 16 (2000), 1112.
- [3] Humphreys, F.J., Hatherly, M., "Recrystallization and related annealing phenomena," Elsevier, UK, (2004).
- [4] Engler, O., and Hirsch, J., *Materials Science and Engineering A*, 336 (2002), 249.
- [5] Zurob, H.S., Hutchinson, C.R., Brechet, Y., and Purdy, G., *Acta Materialia*, 50 (2002), 3077.
- [6] Go, J., PhD Thesis, University of British Columbia, Vancouver, Canada, (2006).
- [7] Anderson, M.P., Srolovitz, D.J., Grest, G.S., and Sahni P.S., *Acta Metallurgica*, 32 (1984) 783.
- [8] Srolovitz, D.J., Grest, G.S., and Anderson, M.P., *Acta Metallurgica*, 34 (1986) 1833.
- [9] Srolovitz, D.J., Grest, G.S., Anderson, M.P., and Rollett, A.D, *Acta Metallurgica*, 36 (1988) 2115.
- [10] Radhakrishnan, B., Sarma, G.B., and Zacharia, T., *Acta Materialia*, 46 (1998) 4415.
- [11] Chun, Y.B., Semiatin, S.L., and Hwang, S.K., *Acta Materialia*, 54 (2006) 3673.
- [12] Song, X., and Rettenmayr, M., *Material Science and Engineering A*, 332 (2002) 153.
- [13] Chakrabarti, D.J. and Laughlin, D.E., *Progress in Materials Science*, 49 (2004) 389.
- [14] Gupta, A.K., Lloyd, D.J., Court, S.A., *Material Science Engineering A*, 301 (2001) 140.
- [15] Morley, A.I., Zandbergen, M.W., and Cerezo, A., *Materials Science Forum*, 519-521 (2006) 543.

- [16] Esmaeili, S., and Lloyd, D.J., *Materials Science Forum*, 519-521 (2006) 169.
- [17] Edwards, G.A., Stiller, K., and Dunlop, G.L., *Acta Materialia*, 46 (1998) 3893.
- [18] Esmaeili, S., Wang, X., and Lloyd, D.J., *Metallurgical and Materials Transactions A*, 34 (2003) 751.
- [19] Wang, X., Esmaeili, S., and Lloyd, D.J., *Metallurgical and Materials Transactions A*, 37 (2006) 2691.
- [20] Van Huis, M.A., Chen, J.H., and Sluiter, M.H.F., *Acta Materialia*, 55 (2007) 2183.
- [21] Marioara, C.D., Andersen, S.J., and Jansen, J., *Acta Materialia*, 49 (2001) 321.
- [22] Andersen, S.J., Zandbergen, H.W., and Jansen, J., *Acta Materialia*, 46, (1998) 3283.
- [23] Matsuda, K., Naoi, T., and Uetani, Y., *Scripta Materialia*, 41, (1999) 379.
- [24] Murayama, M., and Hono, K., *Acta Materialia*, 47, (1999) 1537.
- [25] Miao, W.F., and Laughlin, D.E., *Journal of Materials Science Letters*, 19, (2000) 201.
- [26] Miao, W.F., and Laughlin, D.E., *Scripta Materialia*, 40 (1999) 873.
- [27] Taniguchi, S., Matsuda, K., and Sato, T., *Materials Forum*, 28 (2004) 742.
- [28] Laughlin, D.E., Miao, W.F., and Karabin, L.M., *TMS Annual Meeting*, (1998) 63.
- [29] Porter, D.A., and Easterling, K.E., "Phase transformations in metals and alloys," CRC Press, UK, 1992.
- [30] Reed-Hill, R.E., and Abbaschian, R., "Physical metallurgy," PWS-Kent Pub., USA, 1992.
- [31] Esmaeili, S., Lloyd, D.J., and Poole, W.J., *Acta Materialia*, 51 (2003) 2243.
- [32] Lifshitz, M., and Slyozov, V.V., *Journal of the Physics and Chemistry of Solids*, 19 (1961) pp. 35.
- [33] Brown, L.M., and Ham, R.K., Dislocation Particle Interaction. in: Kelly, A., and Nicholson, R.B., (Eds) *Strengthening Methods in Crystals*, Applied Science, (1971) 9.
- [34] Gerold, V., Precipitation hardening in: Nabarro F.R.N., (Eds) *Dislocations in Solids*, North-Holland Publishing Company (1979) 221.
- [35] Ardell, A.J., *Metallurgical Transaction A*, 16 (1985) 2131.

- [36] Poole, W.J., Wang, W., Lloyd, D.J., and Embury, D., *Philosophical Magazine*, 85 (2005) 3113.
- [37] Morris, J.G., *Materials Science and Engineering*, 13 (1974) 101.
- [38] Zhu, Z., and Starink, M.J., *Material Science Engineering A*, 489 (2008) 138.
- [39] Wang, S.J. and Starink, M.J., *Acta Materialia*, 55 (2007) 933.
- [40] Roven, H.J., Liu, M., and Werenskiold, J.C., *Material Science Engineering A*, 483-484 (2008) 54.
- [41] Ardell, A.J., *Acta Metallurgica*, 20 (1972) 601.
- [42] Hoyt, J.J., "On the coarsening of precipitates located on grain boundaries and dislocations," *Acta Metallurgica et Materialia*, Vol. 39, 1991, pp. 2091-2098.
- [43] Cottrell, A.H. and Bilby, B.A., *Proceeding of the Physical Society*, 62 (1949) 49.
- [44] Deschamps, A., Livet, F., and Brechet, Y., *Acta Metallurgica*, 47 (1999) 281.
- [45] Quainoo, G.K., and Yannacopoulos, S., *Journal of Materials Science*, 39 (2004) 6495.
- [46] Gutierrez-Urrutia, I., Munoz-Morris, M.A., and Morris, D.G., *Journal of Materials Research*, 21 (2006) 329.
- [47] Zhen, L., Fei, W.D., and Kang, S.B., *Journal of Materials Science*, 32, (1997) 1895.
- [48] Marioara, C.D, Nordmark, H, Andersen, S.J, and Holmestad, R., *Journal of Materials Science*, 41 (2006) 471.
- [49] Birol, Y., *Scripta Materialia*, 52 (2005) 169.
- [50] Yassar, R.S., Field, D.P., and Weiland, H., *Scripta Materialia*, 53 (2005) 299.
- [51] Yassar, R.S., PhD thesis, *Washington State University*, Pullman, United States of America (2005).
- [52] Birol, Y., and Karlik, M., *Scripta Materialia*, 55 (2006) 626.
- [53] Long, D.C., Ohmori, Y., and Nakai K., *Materials Transactions*, 41 (2000) 690.
- [54] Shen, C.H., and Ou, B.L., *Canadian Metallurgical Quarterly*, 46 (2007) 65.
- [55] Girifalco, L.A., and Herman, H., *Acta Metallurgica*, 13 (1965) 583.
- [56] Esmaeili, S., Vaumousse, D., Zandbergen, M.W., Poole, W.J., Cerezo, A., and Lloyd, D.J., *Philosophical Magazine*, 87 (2007) 3797.

- [57] Cai, M., Field, D.P., and Lorimer, G.W., *Materials Science and Engineering A*, 373, (2004) 65.
- [58] Shen, C.H., Ou, B.L., *Journal of the Chinese Institute of Engineers*, 31 (2008) 181.
- [59] Verdier, M., Saeter, J.A., Janecek, M., Brechet, Y., Guyot, P., Duly, D., Nes, E., and Orsund, R., *Materials Science Forum*, 217-222 (1996) 435.
- [60] Taylor, G., *Proceeding of the Royal Society of London*, 145 (1934) 362.
- [61] Cheng, L.M., Poole, W.J., Embury, J.D., and Lloyd, D.J., *Metallurgical and Materials Transactions A*, 34 (2003) 2473.
- [62] Ashby, M.F., *Philosophical Magazine*, 14 (1966) 1157.
- [63] Ashby, M.F., *Philosophical Magazine*, 21 (1970) 399.
- [64] Bay, B., Hansen, N., Hughes, D.A., and Kuhlmann-Wilsdorf, D., *Acta Metallurgica et Materialia*, 40 (1992) 205.
- [65] Bay, B., Hansen, N., Hughes, D.A., and Kuhlmann-Wilsdorf, D., *Materials Science and Engineering A*, 158 (1992) 139.
- [66] Young, C.T., Headley, T.J., and Lytton, J.L., *Materials Science and Engineering A*, 81 (1986) 391.
- [67] Liu, Q., Juul Jensen, D., and Hansen, N., *Acta Materialia*, 46 (1998) 5819.
- [68] Nes, E., and Marthinsen, K., *Materials Science and Engineering A*, 322 (2002) 176.
- [69] Gay, P., and Kelly, A., *Acta Crystallographica*, 6 (1953) 172.
- [70] Gay, P., Hirsch, P.B., and Kelly, A., *Acta Crystallographica*, 7 (1954) 41.
- [71] Labusch, R., *Physica Status Solidi*, 41 (1970) 659.
- [72] J. Friedel, "Electron microscopy and strength of materials," Interscience, New York, (1963).
- [73] Lebyodkin, M., Dunin-Barkowskii, L., Brechet, Y., Estrin, Y., and Kubin, L.P., *Acta Materialia*, 48 (2000) 2529.
- [74] Blavette, D., Cadel, E., Fraczkiewicz, A., and Menand, A., *Science*, 286 (1999) 2317.
- [75] Cottrell, A.H., "Dislocations and plastic flow in crystals," Oxford University Press, New York, (1953).

- [76] Cottrell, A.H., and Jaswon, M.A., *Proceeding of the Royal Society of London*, 199 (1949) 104.
- [77] Hughes, D.A., *Acta Metallurgica et Materialia*, 41 (1993) 1421.
- [78] Waldron, G.W.J., *Acta metallurgica*, 13 (1965) 897.
- [79] Driver, J.H., and Papazian, J.M., *Materials Science and Engineering A*, 76 (1985) 51.
- [80] Korbøl, A., Embury, J.D., Hatherly, M., Martin, P.L., and Erbsloh, H.W., *Acta Metallurgica*, 34 (1986) 1999.
- [81] Drury, M.D., and Humphreys, F.J., *Acta Metallurgica*, 34 (1986) 2259.
- [82] Zolotarevsky, N.Y., Solonin, A.N., Churymov, A.Y. and Zolotarevsky, V.S., *Materials Science and Engineering A*, 502 (2009) 111.
- [83] Huang, Y., Robson, J.D., and Prangnell, P.B., *Acta Materialia*, 58 (2010) 1643.
- [84] Nourbakhsh, S., and Nutting, J., *Acta Metallurgica*, 28 (1980) 357.
- [85] Deschamps, A., Brechet, Y., Necker, C.J., Saimoto, S. and Embury, J.D., *Material Science and Engineering A*, 207 (1996) 143.
- [86] Verdier, M., Brechet, Y., and Guyot, P., *Acta Materialia*, 47 (1999) 127.
- [87] Verdier, M., Janecek, M., Brechet, Y., and Guyot, P., *Material Science and Engineering A*, 248 (1998) 187.
- [88] Nes, E., *Acta Metallurgica Materialia*, 43 (1995) 2189.
- [89] Singhal, L.K., and Vaidya, M.L., *Metallurgical and Materials Transactions B*, 1 (1970) 1044.
- [90] Schmidt, C.G., and Miller, A.K., *Acta Metallurgica*, 30 (1982) 615.
- [91] Gutierrez-Urrutia, I., Munoz-Morris, M.A., Morris, D.G., *Materials Science & Engineering A*, 394 (2005) 399.
- [92] Wang, X., Poole, W.J., Embury, J.D., and Lloyd, D.J., *Materials Science Forum*, 519-521 (2006) 1913.
- [93] Saeter, J.A., PhD Thesis, The Norwegian University of Science and Technology, Trondheim, Norway (1997).
- [94] Cottrell, A.H., and Aytikin, V., *Journal of the Institute of Metals*, 77, (1950) 389.
- [95] Friedel, J., "Dislocations," Pergamon Press, Oxford, (1964).

- [96] Starke, E.A.J., and Troeger, L.P., *Materials Science and Engineering A*, 293, (2000) 19.
- [97] Jeniski, R.A., Jr, Thanaboonsombut, B., and Sanders, T.H., Jr, *Metallurgical and Materials Transactions A*, 27 (1996) 19.
- [98] Thanaboonsombut, B., Sanders, T.H., Jr, *Metallurgical and Materials Transactions A*, 28 (1997) 2137.
- [99] Burger, G.B., Gupta, A.K., Jeffrey, P.W., and Lloyd, D.J., *Materials Characterization*, 35 (1995) 23.
- [100] Arzt, E., *Acta Materialia*, 46 (1998) 5611.
- [101] Furu, T., Orsund, R., and Nes, E., *Acta Metallurgica et Materialia*, 43 (1995) 2209.
- [102] Zurob, H.S., PhD Thesis, McMaster University, Hamilton, Canada (2003).
- [103] Doherty, R.D., Hughes, D.A., Humphreys, F.J., *Materials Science and Engineering A*, 238 (1997) 219.
- [104] Troeger, L.P., Starke, E.A.Jr., and Crooks, R., "Method of producing superplastic alloys and superplastic alloys produced by the method," No. US 6350329 (2002).
- [105] Wang, Z.C., and Prangnell, P.B., *Materials Science and Engineering A*, 328 (2002) 87.
- [106] Paton, N.E., and Hamilton, C.H., "Method of imparting a fine grain structure to aluminum alloys having precipitating constituents," No. US 4092181, (1978).
- [107] Waldman, J., Sulinski, H.J., and Markus, H., "Processes for the fabrication of 7000 series aluminum alloys," No. US 3847681, (1973).
- [108] Jazaeri, H., and Humphreys, F.J., *Acta Materialia*, 52 (2004) 3239.
- [109] Jazaeri, H., and Humphreys, F.J., *Acta Materialia*, 52 (2004) 3251.
- [110] Humphreys, F.J., and Chan, H.M., *Materials Science and Technology*, 12 (1996) 143.
- [111] Prangnell, P.B., Hayes, J.S., and Bowen, J.R., *Acta Materialia*, 52 (2004) 3193.
- [112] Humphreys, F.J., *Materials Science Forum*, 467-470 (2004) 107.
- [113] Doherty, R.D., *Progress in Materials Science*, 42 (1997) 39.
- [114] Huang, Y., and Humphreys, F.J., *Acta Materialia*, 47 (1999) 2259.
- [115] Nes, E., Ryum, N., and Hunderi, O., *Acta Metallurgica*, 33 (1985) 11.

- [116] Cahn, J.W., *Acta Metallurgica*, 10 (1962) 789.
- [117] Johnson, W.A., and Mehl, R.F., *American Institute of Mining and Metallurgical Engineers-Transactions*, 135 (1939) 416.
- [118] Avrami, M., *Journal of Chemical Physics*, 7 (1939) 1103.
- [119] Avrami, M., *Journal of Chemical Physics*, 8 (1941) 177.
- [120] Avrami, M., *Journal of Chemical Physics*, 7 (1939) 1103.
- [121] Kolmogorov, A.N., *Bulletin of the Academy of Sciences of the USSR, Mathematical Series*, 1 (1937) 355.
- [122] Juul Jensen, D., *Materials Science and Technology*, 21 (2005) 1365.
- [123] Furu, T., Marthinsen, K., and Nes, E., *Materials Science and Technology*, 6 (1990) 1093.
- [124] Y.S. Seo, Y.B. Chun, and S.K. Hwang, *Computational Materials Science*, 43 (2008) 512.
- [125] X. Song, and M. Rettenmayr, *Computational Materials Science*, 40 (2007) 234.
- [126] Go, J., Poole, W.J., and Militzer, M., *Thermec 2003*, 426-432 (2003) 291.
- [127] Daniel, D., Guiglionda, G., Litalien, P., and Shahani, R., *Materials Science Forum*, 519-521 (2006) 795.
- [128] Hirsch, J., *Materials Forum*, 28 (2004) 15.
- [129] Chung, Y.H., Troeger, L.P., and Starke, E.A.J., *The 4<sup>th</sup> International Conference on Aluminum Alloys*, (1994), 434.
- [130] Ferrasse, S., Segal, V.M., and Hartwig, K.T., *Journal of Materials Research*, 12 (1997) 1253.
- [131] Esmaeili, S., Lloyd, D.J., and Jin, H., Submitted for Publication.
- [132] S.M. van Boxel, M. Seefeldt, B. Verlinden, and P. van Houtte, *Journal of Microscopy*, 218 (2005) 104.
- [133] H. Jin: Private communications, Novelis Global Technology Centre, Kingston, Ontario, Canada, 2010.
- [134] Gupta, A.K., and Lloyd, D.J., *Metallurgical and Materials Transactions A*, 30 (1999) 879.
- [135] Lloyd, D.J., Evans, D.R. and Gupta, A.K. *Canadian metallurgical Quarterly*, **39**, (2000), 475.

- [136] Gaber, A., Mossad Ali, A., Matsuda, K., Kawabata, Yamazaki, T., and Ikeno, S., *Journal of Alloys and Compounds*, 432 (2007) 149.
- [137] Humphreys, F.J., *Journal of Materials Science*, 36 (2001) 3833.
- [138] Poorganji, B., Sepehrband, P., Jin, H. and Esmaeili, S., *Scripta Materialia*, 63 (2010) 1157.
- [139] Wang, X. Unpublished results (2008).
- [140] Sepehrband, P. H. Jin and Esmaeili, S. Unpublished results (2009)
- [141] McCabe, R.J., and Teter D.F., *Journal of Microscopy*, 223 (2006) 33.
- [142] Raveendra, S., Mishra, S., Mani Krishna, K.V., Weiland, H., 39 (2008) 2760
- [143] Tarasuik et. al., *Acta Materialia*, vol. 50, 2002, 1467-1477
- [144] Caleyó, F., Baudin, T., and Penelle, R., *The European physical journal of Applied physics* 20 (2002) 77.
- [145] Bocos, J.L., Novillo, E., Petite, M.M., Iza-Mendia, A. and Gutierrez, I., *Metallurgical and Materials Transactions A*, 34 (2002) 827.
- [146] Cho, j.H., Ha, h.P., Oh. K.H., *Metallurgical and Materials Transactions A*, 36 (2005) 3415.
- [147] Alvi, M.H., Cheong, S., Weiland, H. and Rollett, A.D., *Materials Solutions Conference*, (2003) 191.
- [148] Sepehrband, P. and Esmaeili, S., *Scripta Materialia*, 63 (2010) 4.
- [149] L.P. Troeger, and E.A. Starke Jr, *Material Science and Engineering A*, 277 (2000) 102.
- [150] Y. Huang and F. Humphreys, *Acta Materialia*, 48 (2000) 2017.
- [151] N. Hansen and B. Bay, *Acta Materialia*, 29 (1981) 65.
- [152] A.D. Rollett, D.J. Srolovitz, R.D. Doherty and M.P. Anderson, *Acta Metallurgica*. 37 (1989) 627.
- [153] E.M. Lauridsen, D. Juul Jensen, H.F. Poulsen, U. Lienert, *Scripta Materialia*, 43 (2000) 561.
- [154] Christian, J.W., "The Theory of Phase Transformations in Metals and Alloys" Pergamon Press, Oxford, (1975)
- [155] Vandermeer, R.A., Hansen, N., *Acta Materialia*, 56, (2008), 5719.
- [156] Grong, O. and Shercliff, H.R., *Progress in Materials Science*, 47 (2002) 163.

- [157] Dunlop, J.W.C., Brechet, Y.J.M., Legras, L. and Zurob, H.S., *Journal of Nuclear Material*, 366 (2007) 178.
- [158] Vandermeer, R.A., and Juul Jensen, D., *Acta Materialia*, 49, (2001) 2083.
- [159] Cahn, J.N., *Acta Metallurgica*, 4, (1956) 572.
- [160] Lad, K.N., Savalia, R.T., Pratap, A., Dey, G.K., and Banerjee, S., *Thermochimica Acta*, 473 (2008) 74.
- [161] Lloyd, D.J., and Gupta, A.K., *Thermec*, (1997) 99.
- [162] Chun, Y.B., Semiatin, S.L., and Hwang, *Materials Science Forum*, 654-656 (2010) 1486.
- [163] ASM International Handbook Committee, *Metals Handbook*, 10th ed. (ASM, Materials Park, OH, 1990), Vol. 2.
- [164] Saetre, T.O., Hunderi, O., and Nes, E., *Acta Metallurgica*, 34 (1986) 981.
- [165] Marthinsen, K., Lohne, O., and Nes, E., *Acta Metallurgica*, 37, (1989) 135.

## APPENDIX (A1): MICROGRAPHS

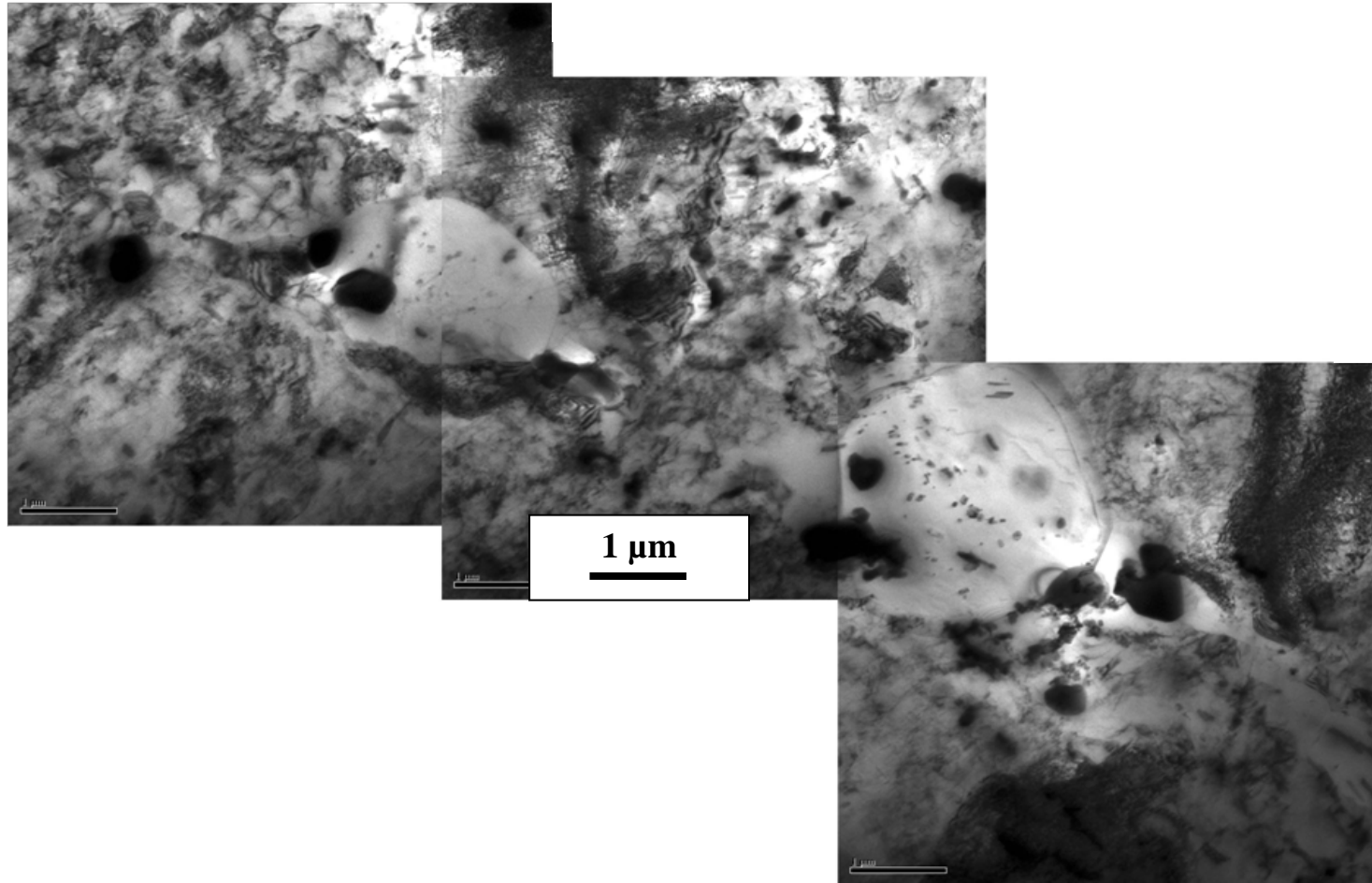


Figure A1- 1. TEM bright field micrographs of the NA-CR-300 sample showing recrystallized grains on a pre-existing grain boundary.

## APPENDIX (A2): MISORIENTATION CALCULATION

In this section, the method which has been used to calculate misorientation between two lattice sites of the EBSD maps is presented.

Orientation of each lattice site of the EBSD map is defined relative to the orientation of the sample by three Euler angles:  $\varphi_1$ ,  $\Phi$ ,  $\varphi_2$  (phi1, Phi, phi2). Corresponding values of Euler angle for each lattice site of the EBSD map have been calculated by Channel 5 software. As schematically presented in [1], to transform the lattice site coordinate system into the sample coordinate system, the following rotations must be performed [1, 2]:

1. a rotation of  $\varphi_1$  about the z-axis,
2. a rotation of  $\Phi$  about the rotated x-axis followed by,
3. a rotation of  $\varphi_2$  about the rotated z-axis.

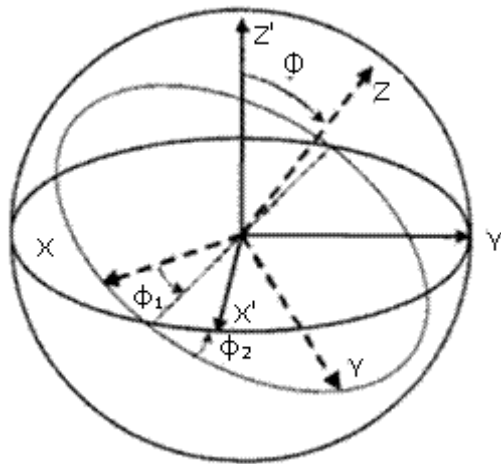


Figure A2- 1. Euler angles that define an orientation of a crystal axes ( $x'$ ,  $y'$ ,  $z'$ ) with respect to the sample axes ( $x$ ,  $y$ ,  $z$ ) [3].

Orientation of a lattice site in respect to the sample coordinate can be represented in form of an orientation matrix. The orientation matrix is a square matrix of nine elements which is defined as:

$$g = \begin{bmatrix} g_{11} & g_{11} & g_{11} \\ g_{11} & g_{11} & g_{11} \\ g_{11} & g_{11} & g_{11} \end{bmatrix}$$

$$g_{11} = \cos \varphi_1 \cos \varphi_2 - \sin \varphi_1 \sin \varphi_2 \cos \Phi$$

$$g_{12} = \sin \varphi_1 \cos \varphi_2 + \cos \varphi_1 \sin \varphi_2 \cos \Phi$$

$$g_{13} = \sin \varphi_2 \sin \Phi$$

$$g_{21} = -\cos \varphi_1 \sin \varphi_2 - \sin \varphi_1 \cos \varphi_2 \cos \Phi$$

(A2- 1)

$$g_{22} = -\sin \varphi_1 \sin \varphi_2 + \cos \varphi_1 \cos \varphi_2 \cos \Phi$$

$$g_{23} = \cos \varphi_2 \sin \Phi$$

$$g_{31} = \sin \varphi_1 \sin \Phi$$

$$g_{32} = -\cos \varphi_1 \sin \Phi$$

$$g_{33} = \cos \Phi$$

The misorientation between two lattice sites can be calculated once their orientation matrices are defined from Equation (A2- 1). The misorientation between two crystals is given by:

$$\Delta g = g_1 g_2^{-1} \tag{A2- 2}$$

where  $g_1$  and  $g_2$  are the orientation matrices of the two lattice sites, and  $\Delta g$  is the matrix which represents the misorientation between  $g_1$  and  $g_2$ . In Equation (A2- 2),  $g_2$  is arbitrarily chosen to be the reference orientation. The orientation matrix can be used to find the angle/axis of misorientation which describes the misorientation between two lattice sites. The

pair of misorientation angle/axis defines a rotation angle about a certain axis to transform the coordinate system of one lattice site into the coordinate system of the other one [1, 2]. Due to crystal symmetries, there are several pairs of misorientation angle/axis that describe equal misorientation between two crystals. For cubic crystals, there are 24 different ways to describe the crystal orientation. These symmetrical orientations can be described by symmetry matrices which are the symmetry operations of the crystal structure [1]. The 24 symmetric matrices for cubic crystals are given in Figure A2- 2.

$$\begin{array}{cccccc}
 \begin{pmatrix} 1 & 0 & 0 \\ 0 & 1 & 0 \\ 0 & 0 & 1 \end{pmatrix} & \begin{pmatrix} 0 & 0 & \bar{1} \\ 0 & \bar{1} & 0 \\ \bar{1} & 0 & 0 \end{pmatrix} & \begin{pmatrix} 0 & 0 & \bar{1} \\ 0 & 1 & 0 \\ 1 & 0 & 0 \end{pmatrix} & \begin{pmatrix} \bar{1} & 0 & 0 \\ 0 & 1 & 0 \\ 0 & 0 & \bar{1} \end{pmatrix} & \begin{pmatrix} 0 & 0 & 1 \\ 0 & 1 & 0 \\ \bar{1} & 0 & 0 \end{pmatrix} & \begin{pmatrix} 1 & 0 & 0 \\ 0 & 0 & \bar{1} \\ 0 & 1 & 0 \end{pmatrix} \\
 \begin{pmatrix} 1 & 0 & 0 \\ 0 & \bar{1} & 0 \\ 0 & 0 & \bar{1} \end{pmatrix} & \begin{pmatrix} 1 & 0 & 0 \\ 0 & 0 & 1 \\ 0 & \bar{1} & 0 \end{pmatrix} & \begin{pmatrix} 0 & \bar{1} & 0 \\ 1 & 0 & 0 \\ 0 & 0 & 1 \end{pmatrix} & \begin{pmatrix} \bar{1} & 0 & 0 \\ 0 & \bar{1} & 0 \\ 0 & 0 & 1 \end{pmatrix} & \begin{pmatrix} 0 & 1 & 0 \\ \bar{1} & 0 & 0 \\ 0 & 0 & 1 \end{pmatrix} & \begin{pmatrix} 0 & 0 & 1 \\ 1 & 0 & 0 \\ 0 & 1 & 0 \end{pmatrix} \\
 \begin{pmatrix} 0 & 1 & 0 \\ 0 & 0 & 1 \\ 1 & 0 & 0 \end{pmatrix} & \begin{pmatrix} 0 & 0 & \bar{1} \\ \bar{1} & 0 & 0 \\ 0 & 1 & 0 \end{pmatrix} & \begin{pmatrix} 0 & \bar{1} & 0 \\ 0 & 0 & 1 \\ \bar{1} & 0 & 0 \end{pmatrix} & \begin{pmatrix} 0 & 1 & 0 \\ 0 & 0 & \bar{1} \\ \bar{1} & 0 & 0 \end{pmatrix} & \begin{pmatrix} 0 & 0 & \bar{1} \\ 1 & 0 & 0 \\ 0 & \bar{1} & 0 \end{pmatrix} & \begin{pmatrix} 0 & 0 & 1 \\ \bar{1} & 0 & 0 \\ 0 & \bar{1} & 0 \end{pmatrix} \\
 \begin{pmatrix} 0 & \bar{1} & 0 \\ 0 & 0 & \bar{1} \\ 1 & 0 & 0 \end{pmatrix} & \begin{pmatrix} 0 & 1 & 0 \\ 1 & 0 & 0 \\ 0 & 0 & \bar{1} \end{pmatrix} & \begin{pmatrix} \bar{1} & 0 & 0 \\ 0 & 0 & 1 \\ 0 & 1 & 0 \end{pmatrix} & \begin{pmatrix} 0 & 0 & 1 \\ 0 & \bar{1} & 0 \\ 1 & 0 & 0 \end{pmatrix} & \begin{pmatrix} 0 & \bar{1} & 0 \\ \bar{1} & 0 & 0 \\ 0 & 0 & \bar{1} \end{pmatrix} & \begin{pmatrix} \bar{1} & 0 & 0 \\ 0 & 0 & \bar{1} \\ 0 & \bar{1} & 0 \end{pmatrix}
 \end{array}$$

**Figure A2- 2. The 24 symmetric matrix operators for a cubic system [1].**

To find the smallest misorientation angle between the two lattice sites, the symmetry operators are applied to the misorientation matrix  $\Delta g$  and the misorientation angle for each

condition is calculated through Equation (A2- 3) [1, 2]. The smallest misorientation angle is considered as the misorientation angle between  $g_1$  and  $g_2$ .

$$\cos \theta = \frac{(O\Delta g_{11} + O\Delta g_{22} + O\Delta g_{33} - 1)}{2} \quad (\text{A2- 3})$$

The above calculation has been performed by generating a Matlab code which calculates misorientation between all neighbouring sites of the EBSD map.

### References:

- [1] Randle, V., Engler, O., Introduction to Texture Analysis, CRC Press, 2000.
- [2] Randle, V., Theoretical framework for electron backscatter diffraction, in: A.J. Schwartz, M. Kumar, and B.L. Adams (Eds), Electron Backscatter Diffraction in Material Science, Kluwer Academic/Plenum Publishers, 2000, pp. 19-31.
- [3] Rajan, R., Presentation of texture in orientation space, in: A.J. Schwartz, M. Kumar, and B.L. Adams (Eds), Electron Backscatter Diffraction in Material Science, Kluwer Academic/Plenum Publishers, 2000, pp. 31-39.